EXTREME FAST CHARGING FOR LITHIUM ION BATTERIES: STRUCTURAL ANALYSIS OF ELECTRODES AND SOLVENT FORMULATION OF ELECTROLYTES

by

Xianyang Wu

A Dissertation

Submitted to the Faculty of Purdue University

In Partial Fulfillment of the Requirements for the degree of

Doctor of Philosophy

School of Mechanical Engineering

West Lafayette, Indiana

May 2022

THE PURDUE UNIVERSITY GRADUATE SCHOOL
STATEMENT OF COMMITTEE APPROVAL

Dr. Kejie Zhao, Chair
School of Mechanical Engineering

Dr. Zhijia Du
Oak Ridge National Laboratory

Dr. Jong Hyun Choi
School of Mechanical Engineering

Dr. Adrian Buganza Tepole
School of Mechanical Engineering

Approved by:
Dr. Nicole L. Key

Dedicated to my family,
for their encouragement and support

ACKNOWLEDGMENTS

First, I would like to express my sincere gratitude to my advisor, Dr. Kejie Zhao, for his patience and guidance at Purdue. Time flies, and I still remember my first visit to Dr. Zhao's office in the summer of 2017 vividly. As a graduate student with no background in lithium ion batteries (LIBs), Dr. Zhao suggested that I start with experiments first. I began my research on the solid-state electrolyte of LIBs. During my 1st year, I made not too much progress on the search, as the course load was relatively heavy for me. Fortunately, Dr. Zhao exhibits excellent understanding and tolerance, although he faces his own pressures. For international students whose native language is not English, besides the research, giving a comprehensive presentation is another challenge. At the same time, it plays a vital role for researchers to survive in academia. Then Dr. Zhao offered us more practice on this, from one-to-one discussion every week to group discussion.

Furthermore, my skills in giving presentations have significantly improved during these years. For the research, I learned the key of doing research from my weekly discussion with Dr. Zhao, from initial experimental design to the logical rigour of final conclusion and the skills on preparing the manuscript. I really appreciate Dr. Zhao's patience, tolerance, and encouragement on my way to becoming an independent researcher.

Besides, I want to express my great appreciation to Dr. Zhao, Dr. Zhijia Du and Dr. Jue Liu for providing me with the excellent opportunity to visit Oak Ridge National Laboratory (ORNL) and do my thesis there. I am grateful for the knowledge, experimental skills, and encouragement from Dr. Zhijia Du, my host at of Electrification and Energy Infrastructures Division of ORNL. As a visiting student at ORNL, I learned many experimental skills from him, and my understanding of the whole LIB system solidified during our daily discussions. During my period at the Spallation Neutron Source of ORNL, I mastered the skills of probing the crystal structure of electrodes: from the short-range order obtained from pair distribution function to the long-range order extracted from diffraction data.

At the same time, I want to express my appreciation to my thesis committees, Dr. Zhijia Du, Dr. Jong Hyun Choi, and Dr. Adrian Buganza Tepole, for their insightful suggestions and comments. Besides, I really appreciate the efforts/time of all the committee members in arranging my thesis defense.

During my years at Purdue, I am fortunate to meet everyone in Zhao's group: Dr. Rong Xu, Dr. Luize Scalco de Vasconcelos, Dr. Hong Sun, Xiaokang Wang, Nikhil Sharma, Ram Kishore Venkatesan, Jiaxiu Han, Sameep Shah, Xixian Yang, Dongliang Wu, Dr. Shan Hu, and Madison Perrin. When I began my first nano-indentation experiment on LIBs, I had no experience with all those things as my research experience was mainly on simulation. With the help of Rong and Luize, I successfully finished my first experiment and started my research on the solid-state electrolyte of LIBs. Whenever I had some unknown things on experiments or LIBs, I could have a fruitful discussion with members of the group. And I really enjoy the days with everyone in the group: from discussions on courses that we should choose every semester to the unknown experimental skills/knowledge on LIBs and the chit-chat on courses we chose and arrangements during holidays.

I want to express my deepest gratitude to my collaborators and friends at ORNL: Dr. Jianlin Li, Dr. Bohang Song, Dr. Linxiao Geng, Dr. Yaocai Bai, Dr. Bo Jiang, Dr. Yuxuan Zhang, Dr. Mengya Li and Dr. Erxi Feng. For LIBs, it involves too many things, from crystallography of electrode materials, liquid/solid electrolyte to the dynamic behavior of Li migration/diffusion, and it is really challenging for newcomers to have a good understanding of it and starts his/her research. Every time I have some unknown things, from the detailed steps for rinsing cycled electrodes, the preparation of pouch cells for further testing, and the technical details of Rietveld refinement of powder diffraction data, I can find suggestions even solutions to my problems after enjoyable discussion with them.

Last, I want to express my thanks to my family: my great parents, Mr. Chunzhou Wu, Mrs. Guifang Ding; my sisters, Mrs. Caixia Wu, Mrs. Lipin Wu, Miss Lixin Wu and my brother Mr. Xianfei Wu. I am quite proud to have this big family. Without their constant encouragement and never-ending support, I will not obtain this degree.

TABLE OF CONTENTS

LIST OF TABLES

LIST OF FIGURES

ABSTRACT

Fossil fuel has dominated the global energy market for centuries, and the world is undergoing a great energy revolution from fossil fuel energy to renewable energies, given the concerns on global warming and extreme weather caused by the emission of carbon dioxide. Lithium ion batteries (LIBs) play an irreplaceable role in this incredible energy transition from fossil energy to renewable energy, given their importance in energy storage for electricity grids and promoting the mass adoption of battery electric vehicles (BEVs). Extreme fast charging (XFC) of LIBs, aiming to shorten the charging time to 15 minutes, will significantly improve their adoption in both the EV market and grid energy storage. However, XFC has been significantly hindered by the relatively sluggish Li^+ transport within LIBs.

Herein, effects caused by increasing charging rates (from 1C, 4C to 6C) on $LiNi_{0.6}Mn_{0.2}Co_{0.2}O_2$ (NMC622) || graphite cell were systematically probed via various characterization methods. From electrochemical test on their rate/long term cycling performance, the significant decrease in available capacity under high charging rates was verified. Structural evolutions of cycled NMC622 cathode and graphite anode were further probed via ex-situ powder diffraction, and it was found that lattice parameters *a* and *c* of NMC622 experience irreversible evolution due to loss of active Li^+ within NMC622; no structural evolution was found for the graphite anode, even after 200 cycles under 6C (10 minutes) high charging rates. The aging behavior of liquid electrolyte was further analyzed via inductively coupled plasma-optical emission spectrometry (ICP-OES) and gas chromatography-mass spectrometry (GC-MS), increased Li^+ concentration under higher charging rates and show-up of diethyl carbonate (DEC) and dimethyl carbonate (DMC) caused by transesterification both suggest faster aging/degradation of liquid electrolyte under higher charging rates.

Given the structural evolution of NMC622 caused by irreversible Li^+ loss after long term cycling, the structural evolution of both NMC622 cathode and lithiated graphite anode were further studied via operando neutron diffraction on customized $LiNi_{0.6}Mn_{0.2}Co_{0.2}O_2$ (NMC622) || graphite cell. Via a quantitative analysis of collected Bragg peaks for NMC622 and lithiated graphite anode, we found the rate independent structural evolution of NMC622: its lattice parameters *a* and *c* are mainly determined by Li^+ contents within it (*x* within $Li_xNi_{0.6}Mn_{0.2}Co_{0.2}O_2$) and follow the same evolution during the deintercalation process, from slowest 0.27 C charging to the fastest 4.4 C

charging. For graphite intercalated compounds (GICs) formed during Li^+ intercalating into graphite, the sequential phase transition from pure graphite → stage III (LiC_{30}) → stage II (LiC_{12}) → stage I (LiC_6) phase under 0.27 C charging is consistent with previous studies. This sequential phase transition is generally maintained under increasing charging rates, and the co-existence of LiC_{12} phase and LiC_6 was found for lithiated graphite under 4.4 C charging, mainly due to the large inhomogeneity under these high charging rates. Meanwhile, for the stage II (LiC_{12}) → stage I (LiC_6) transition, which contributes half the specific capacity for the graphite anode, quantitative analysis via Johnson-Mehl-Avrami-Kolmogorov (JMAK) model suggests it to be a diffusion-controlled, one-dimensional transition, with decreasing nucleation kinetics under increasing charging rates.

Based on the LiC_{12} → LiC_6 transition process, strategies to improve the Li^+ transport properties were further utilized. Various cosolvents with smaller viscosity, from dimethyl carbonate (DMC), ethyl acetate (EA), methyl acetate (MA) to ethyl formate (EF), were further tested by replacing 20% (weight percent) ethyl methyl carbonate (EMC) of typical 1.2 M $LiPF_6$ salt solvated in ethylene carbonate (EC)/EMC solvents (with a weight ratio of 30:70). From the measurement of their ion conductivity, the introduction of these cosolvents indeed enhanced the Li^+ transport properties. This was further verified by improved rate performance from 2C, 3C to 4C charging for liquid electrolytes using these cosolvents. Both X-ray absorption spectroscopy (XAS) and X-ray powder diffraction (XRD) indicated the increase of Ni valence state and structural evolution of NMC622, all resulting from the irreversible loss of active Li^+ within the NMC622 cathode. From long term cycling performance and further analysis of interfaces formed between electrode and anode, the best performance of electrolyte using DMC cosolvent was attributed to the most stable solid electrolyte interphase (SEI) and cathode electrolyte interphase (CEI) formed during the cycling.

1. FUNDAMENTALS OF LITHIUM ION BATTERIES

During the past centuries, fossil fuels, especially crude oil, have greatly improved humanity's life and dominated the global energy market, as more than 80% of global energies are fossil fuel energies [1]. At the same time, it causes serious climate challenges from global warming caused by the emission of carbon dioxide to extreme weather [2,3]. Thus, as shown in **Figure 1.1**, most countries promise to realize carbon neutrality by 2060 via replacing fossil fuels with "green energy" like wind energy and solar energy [4–6]. Furthermore, the world is experiencing this great energy revolution from fossil fuels to renewable energies. For these renewable wind/solar energies, due to their intrinsic instability, grid energy storage devices are of great necessity to stabilize their transport over grids [7–9].

Given its good balance between cost, performance, and maturity, lithium ion battery (LIB) plays a central role in this energy revolution. LIBs with improved rate performance will respond better to the dynamic needs of grids thus serve better to the energy storage needs from these renewable energies; meanwhile, shortening charging time will mitigate greatly people's concern on the time consumed for the charging of LIBs and thus stimulate the mass application of both renewable energies and battery electrical vehicles (BEVs) [10,11]. Thus, the enhanced rate performance of LIBs will significantly accelerate this revolution.

In line with this incredible energy evolution, the Department of Energy of US (DOE) sets detailed technical goals to realize extreme fast charging (XFC) for LIBs: while shortening charging time to be less than 15 minutes, BEVs should have the range of over 300 miles, and 80% capacity needs to be retained after 500 cycles, with initial energy density $\geq$ 180 Wh/Kg [12]. These years, extensive studies have been implemented on the realization of extreme fast charging, and the latest progress is well summarized in these publications [10,13–19].

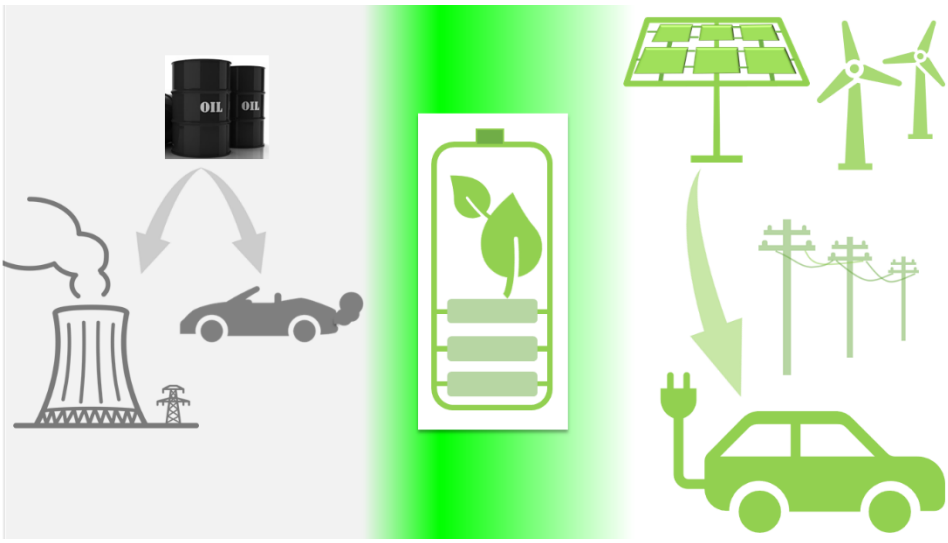

Figure 1.1. Energy revolution from fossil energy to renewable energy to realize carbon neutrality by 2060

1.1 Fundamentals of Lithium ion batteries

Typically, LIBs possess a sandwich structure and consist of three major components: the cathode material providing active Li^+ during the charging process, electrolyte (nonaqueous liquid or solid-state) bridging Li^+ transport between cathode and anode, with the anode playing as the host for intercalated Li^+. For the charging process, the Li^+ deintercalates from the cathode and diffuses/migrates within the electrolyte, and gets intercalated into the anode within the internal circuit. For the external circuit, electrons are pumped from the cathode with a relatively lower Fermi energy level into an anode with a relatively higher Fermi energy level by the power source. Thus, electroneutrality is well maintained, and the electrical energy is then successfully converted into chemical energies stored within LIBs. When it comes to the discharging process, movements of electrons in the external circuit and Li^+ in the internal circuit experience the reverse process.

For the open-circuit voltage (V_{oc}) of LIBs, higher V_{oc} has the potential to provide a higher average working voltage and higher energy density. However, the V_{oc} is intrinsically determined by the difference between the electrochemical potential of the cathode (μ_C) and the anode (μ_A), as shown in equation (1.1), where e presents the magnitude of an electron charge. As shown in **Figure 1.2a**, dominating cathode materials used in LIBs were all developed by John B. Goodenough and his collaborators and further improved by the whole community, from polyanion $Li_xFe_2(XO_4)_3$,

spinel $LiMn_2O_4$ to layered oxide $LiTMO_2$ with 3d transitional metal (TM) cations Ni, Mn and Co, typically [20,21].

$$V_{oc} = (\mu_A - \mu_C)/e \qquad (1.1)$$

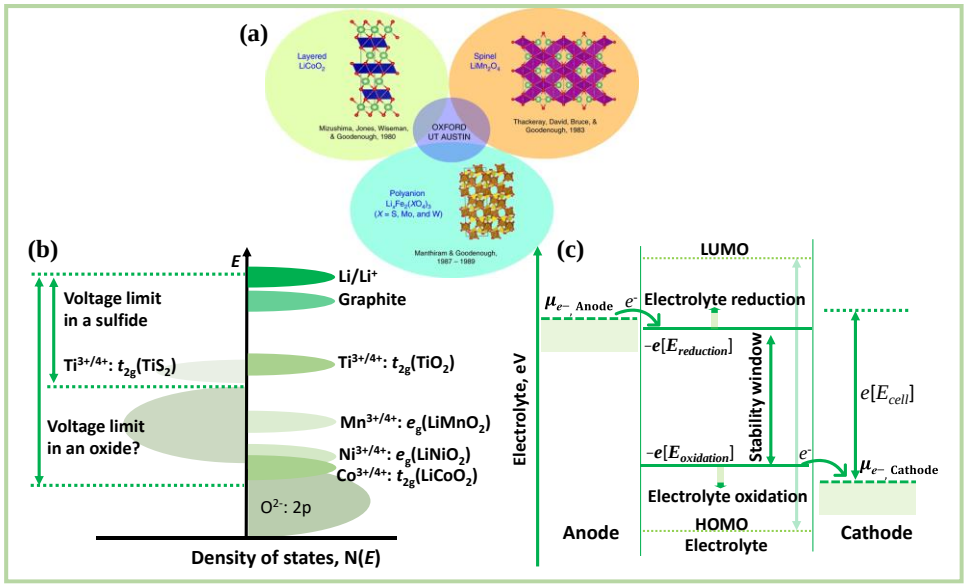

Figure 1.2. Constrains on voltage range of LIBs: (a) the 3 major types of cathode materials utilized by the LIBs industry [20], (b) the relative energy scheme for various elements within cathode materials [20], adapted with permission from Manthiram, (c) the stability window of liquid electrolyte within LIBs [22], adapted with permission from Peljo et al..

As shown in **Figure 1.2b,** the workable voltage range for cathodes is intrinsically constrained by the relative energy difference between TM cations and anions (typically, oxygen and sulfide) within the cathode frame. During the charging process, TM cations are the redox center to maintain electroneutrality via its reduction (TM cations get electrons during discharging) and oxidation (TM cations lose electrons during charging). Moreover, cathode materials involving anionic redox (mainly the participation of oxygen) are not considered as those cathode materials are still immature, and there is no actual application in the industry [23,24]. Meanwhile, during the charging process, electrons are deprived of these TM cations and transferred to the anode within the external circuit. Thus, the valence state of TM cations increases and their energy levels drop down after this oxidation, and the higher voltage the cathode is charged to, the lower will the energy level TM cations will drop into. When charged to a critical value (the amount of deintercalated Li^+ from the cathode is greater than a specific value), the energy level of TM cations

will even drop to levels lower than that of O_{2p} orbitals. Thus, the further charging process (the further deintercalation of Li^+ from cathode materials) will involve electrons transferring not from the TM cations but from the O_{2p} orbital. As oxygen anions form the basic frames for the whole crystal structure of cathode material, their participation in the following redox reaction will lead to their loss of electrons. Beyond a certain level, the charging of LIBs will lead to the formation of O_2 gas from O^{2-} anions and result in detrimental structural damage to the cathode material and final breakdown of cathode materials. Goodenough initially suggested this, and it was experimentally verified in recent studies. The redox behaviors of oxygen (the participation of oxygen in losing/getting electrons during the charging/discharging process) within $LiTMO_2$ are under intensive studies these days, given their possibility to improve the specific capacity of cathode materials [23–25]. In this study, we focus only on the redox behavior of TM elements and choose the typical value of 4.2 V vs. Li/Li^+ for $LiNi_{0.6}Mn_{0.2}Co_{0.2}O_2$ (NMC622) cathode; thus no redox behavior of oxygen is involved in the study.

Besides the constrain from cathode materials, the working voltage range for LIBs should also be within the electrochemical stability window of liquid electrolytes, as shown in **Figure 1.2**c. It is known that during the charging/discharging process, the liquid electrolyte tends to be reduced at the anode side (during the discharging process) and oxidated at the cathode side (during the charging process). If μC and μA are out of this stability window, oxidation/reduction of liquid electrolyte will occur during each cycle, leading to various side reactions, irreversible loss of active Li+ from cathode material, lower Coulomb efficiency, and accelerated degradation of the full cell [22]. This stability window of liquid electrolyte is theoretically determined by its thermodynamic properties and could be verified by various electrochemical characterization methods like the cyclic voltammetry (CV) method. Within a given voltage range, a larger charging/discharging current for different electrolyte systems suggests higher instability within this voltage range. This stability window is also empirically determined by the energy difference between the lowest-unoccupied molecular orbital (LUMO) and the highest-occupied molecular orbital (HOMO) of given electrolyte systems. Meanwhile, ideal passivation interphases between electrode and electrolyte, like the solid electrolyte interphase (SEI) and cathode electrolyte interphase (CEI) formed during formation processes or initial cycles, could enlarge this stability window, given their capabilities to transport Li^+ and hinder the transport of electrons between electrolyte and

electrodes, thus prevents damaging side reactions and stabilize the liquid electrolyte at the electrolyte/electrode interphase [26,27].

To realize the energy density of 180 Wh/Kg, thick electrodes are needed to compensate for the masses from inactive components (including alumina/copper current collectors, polymer separators, and external alumina pouch) thus cathode materials with high specific capacities are preferred as relatively thinner cathode coating will be utilized for given energy density. As shown in **Figure 1.3**, for the specific capacity of various cathode materials, they are well summarized by Wenhua Zuo et al. [28]. And layered oxide NMCs (NMC622, NMC811 here, with NMC111/NMC532 not included) dominate all these cathode materials due to their balance between various metrics (mass/volume specific capacity, safety, structural stability, cost, and technical maturity). For the leading $LiNi_{1-x-y}Mn_xCo_yO_2$ ($0<x, y<1$) cathode materials, although $Li_1Ni_{0.8}Mn_{0.1}Co_{0.1}O_2$ (NMC811) possesses a higher specific capacity and has been successfully commercialized, $Li_1Ni_{0.6}Mn_{0.2}Co_{0.2}O_2$ (NMC622) is utilized in the whole study as NMC811 commonly accompanies with Li^+/Ni^{2+} mixing and the quality of NMC811 relies heavily on the providers. Graphite is chosen in this study for the anode materials due to its dominant role in the LIB industry.

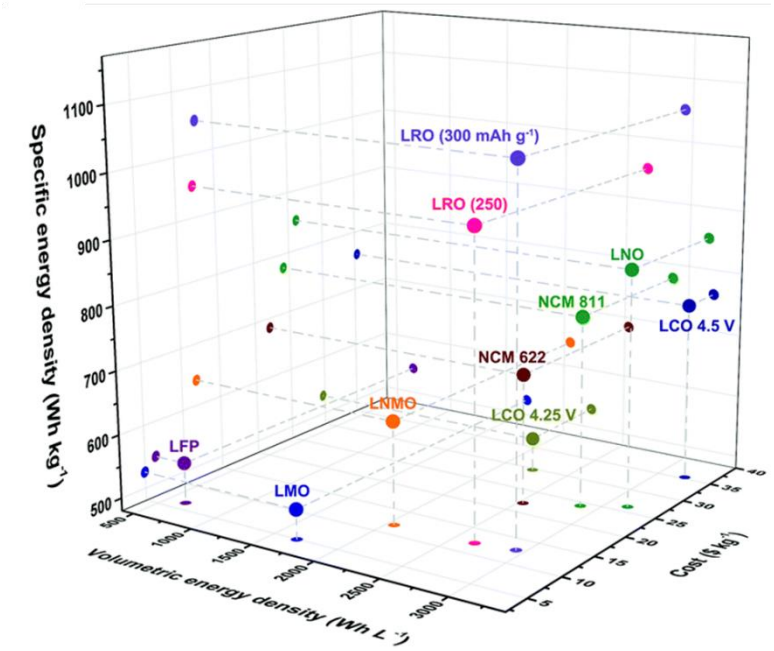

Figure 1.3. Specific/volumetric energy densities, costs for various cathode materials used for LIBs [28].

1.2 Li^+ transport within LIBs

For Li^+ transport behaviors within LIBs, at the cell scale (with the characteristic length of ~ 10 cm in this study), as seen in **Figure 1.4a**, there is a Li^+ concentration gradient from the cathode side to the anode to support the diffusion/migration from cathode to anode during the charging process. At the microscale (with the characterization length of ~10 μm, as shown in **Figure 1.4b**), from the core region to the outer shell of secondary cathode particles, Li^+ concentration possesses a significant decreasing trend to support the Li^+ diffusion/migration within cathode particles; at the anode side, Li^+ concentration shows an increasing trend from the outer shell to core regions during their intercalation into the graphite anode; for the nonaqueous liquid electrolyte, the Li^+ also exhibits this concentration gradient, from the cathode side to the anode side. Under larger currents of higher charging rates, higher concentration gradients within LIBs will form. These concentration gradients lead to larger overpotentials within electrodes and electrolytes. This will lead to a shorter charging time to reach the cutoff voltage and a more extended voltage holding time under the cutoff voltage [29]. During the voltage holding process, as the current is mainly from diffusion caused by the Li^+ concentration gradient, it vanishes quickly. Thus, further voltage holding contributes no more capacity as no Li^+ intercalation continues. Then, less capacity is obtained during this voltage holding stage than the constant current charging.

For the Li^+ diffusion within electrodes (NMC622 cathode and graphite anode) at the atomic scale (with the characteristic length of ~ 1nm), it generally diffuses via hopping through neighboring vacancy sites, and the diffusion rate is well described by the transition state theory shown in equation (1.2), where Γ represents the diffusion rate, v^* represents the effective vibrational frequency and ΔE_B is the activation barrier needed to overcome during the diffusion process [30].

$$\Gamma = v^* \exp\left(-\Delta E_B / kT\right) \quad (1.2)$$

Given the layer structure of the NMC622 cathode, it consists of repeating layers of Li-O-TM slabs, and each Li^+ forms a LiO_6 octahedron with neighboring oxygen anions, with the Li^+ forming a rhombus within the Li layer. Considering the arrangement of neighboring Li vacancies around the hopping Li^+, its diffusion consists of two hopping mechanisms: the diffusion via oxygen dumbbell hop (ODH) path and the tetrahedral site hop (TSH) path, as proposed by A. Van der Ven et.al [31]. As shown in **Figure 1.4c**, for the Li^+ diffusion via ODH path, it occurs with infinite

dilution of the Li^+ vacancy site (in the initial deintercalation process for $LiTMO_2$), and the Li^+ hops directly into the closest Li vacancies positions; for the TSH path, the Li^+ diffuses into available divacancy site only when enough divacancies exist [32]. As the TSH path possesses a lower energy barrier ΔE_B than the ODH path, the Li^+ within layered cathode is mainly diffusing via the TSH path for most of the Li deintercalation from cathode. Depending on the extent and detailed spatial distribution of Li^+ within the Li layer, the Li^+ diffusion is thus mainly determined by the following factors: the Li^+ concentration within Li_xTMO_2, the extent of Li/TM mixing, the distance between Li slabs and neighboring oxygen slabs, the TM species, and their valence states. Generally, the Li^+ diffuses faster with less Li^+ content within the layered cathode due to higher Li^+ vacancies available for diffusion. Also, the Li^+ diffuses relatively slower with more Li/TM mixing, as TM ions mixing into the Li layer shrink the TMO_6 octahedra, given its small radius than Li^+ and stronger attraction with neighboring oxygen ligands. This will also shorten the layer space. Besides, TM ions with a higher valence state than Li+ in the Li slab exert larger electrostatic repulsion than Li+. All these will lead to a higher energy barrier for Li+ hopping, hindering the Li^+ diffusion within Li layers. Other factors affecting the Li^+ diffusivity are mainly due to their effects on enhancing the energy barrier ΔE_B needed to overcome for the diffusion of Li^+, for example, Co^{4+} has small radius than Co^{3+} and stronger attraction with oxygen ligands thus higher energy barrier for Li^+ diffusion, thus leading to decreased Li^+ diffusivity at a higher state of charge. Moreover, systematic studies on these factors can be found in Ceder's publications [33]. Meanwhile, these characteristics of Li^+ diffusion also result in the kinetic hindrance widely observed in layer oxide cathode materials [30].

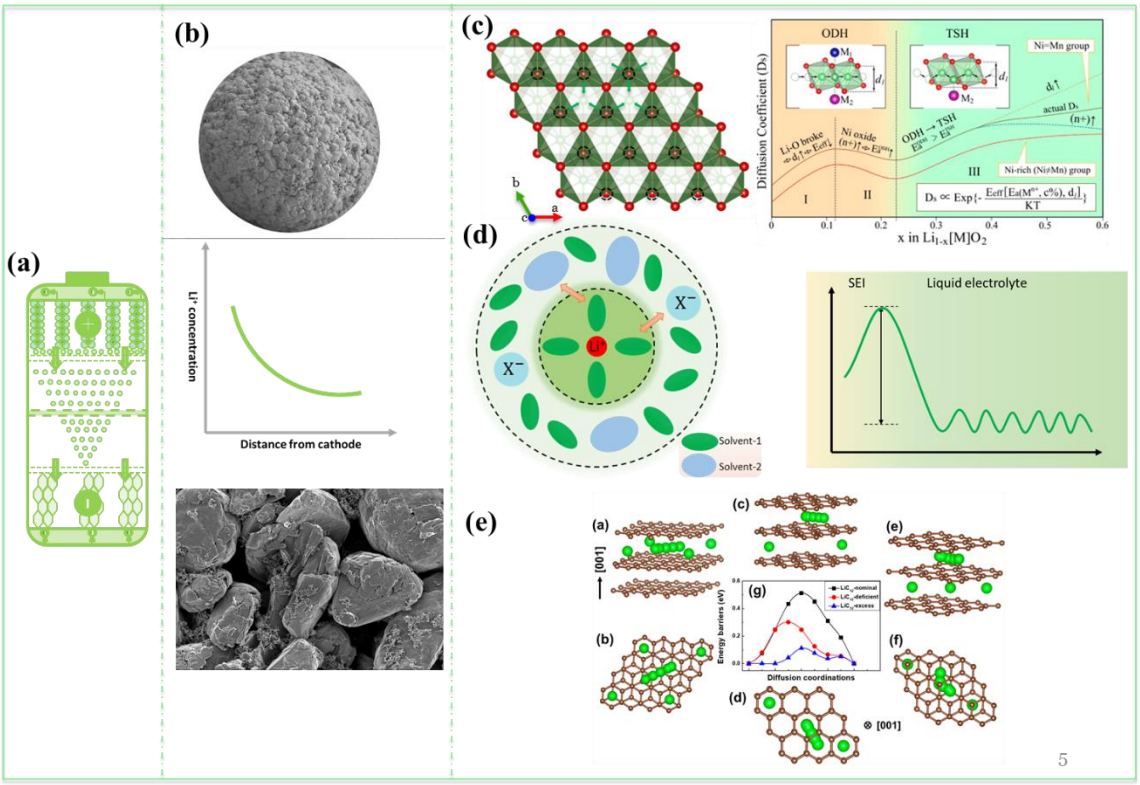

Figure 1.4. Li^+ diffusion within LIBs, (a) schematic image of LIBs; (b) polarization during the charging process; (c) Li^+ diffusion within layered oxide $LiTMO_2$ [32], adapted with permission from Y.Wei et al.; (d) the solvation structure for Li^+ within liquid electrolyte and accompanying energy barrier for the desolvation process [34], adapted with permission from S.S.Zhang, (e) Li^+ diffusion within LiC_6 phases [35], adapted with permission from Q. Liu et al..

For liquid electrolytes transporting the Li^+ from cathode to anode, it typically consists of Li salts and organic solvents to dissociate Li salts into Li^+ cation and anions. Organic solvents commonly used in LIBs are linear carbonates mixed with ethylene carbonate (EC), which functions irreplaceably in the formation of stable SEI layers on graphite anode and enhances Li^+ transport properties [36,37]. The solvation structure formed is schematically shown in **Figure 1.4d**. The Li^+ first forms an inner shell of prime solvation structure (with a strong attraction between Li^+ and coordinated solvent molecules) and an outer shell of second solvation structure (loose interaction with neighboring solvent molecules) and experiences bulk migration/diffusion. At the electrolyte/SEI interphase, the Li^+ overcomes a much higher energy barrier to get desolvated from the solvation shell. And then, the Li^+ is transported through the SEI layer. For its transport through the SEI layers, the detailed diffusion mechanism is still unclear as it is pretty challenging to

implement experiments on the transport of Li^+ through the very thin SEI layers of ~ 10 to 20 nm thick.

When it comes to the Li^+ diffusion within graphite anode, it generally diffuses within two adjacent graphene layers. As various graphite intercalated compound (GIC) phases (stage III, dilute stage II, stage II to the final stage I) form during the Li intercalation process, the Li^+ diffusivity within GICs relies heavily on the exact phases formed and the extent of graphite intercalated. Generally, the diffusivity of Li^+ follows a decreasing trend with higher Li^+ concentration within each phase formed. Taking the detailed Li^+ diffusion from LiC_{12}-deficient to nominal LiC_{12} and LiC_{12}-excess shown in **Figure 1.4e**, possible Li diffusion paths are well illustrated [35]. Various experiments also indicated that the Li^+ diffusivity relies heavily on the microstructure and compositions of the graphite flakes.

1.3 Aging of LIBs during cycling

LIB is a complex system involving various physical/chemical side reactions during the charging/discharging process. It experiences aging with significant degradation of reversible capacity and rate/power performance. Typically, the degradation of LIBs can be divided into the capacity fade and the power fade: for the capacity fade, the capacity obtained from LIBs shows a significant decreasing trend during the long term cycling; for the power fade, the ratio available capacity of the total capacity that could be extracted under given charging/discharging rates also shows a decreasing trend. For the capacity fade, the irreversible loss of active Li^+ within the cathode and loss of contact of electrode materials during the long term cycling leads to decreasing usable capacity. For the power fade, the increase of internal resistance, mainly due to SEI/CEI thickening and cracks formed within electrode particles, results in the degradation of rate/performance.

Furthermore, comprehensive cell aging mechanisms are summarized in **Figure 1.4**, and more comprehensive reviews on cell aging mechanisms can be found in recent publications [38,39]. For these aging mechanisms, they include the inevitable loss of reversible Li^+ from the cathode via Li plating or consumption of active Li^+ at the SEI/CEI interphase, the loss of active electrode material via losing contact with the current collector, the formation of fresh surfaces caused by cracking of electrodes under repeated cycling, the increase of internal resistance due to thickness/composition evolution of SEI/CEI, and the aging of liquid electrolyte. These effects are

tightly coupled with each other: for example, the loss of reversible Li^+ lead to thicker SEI/CEI layers, and thicker SEI/CEI layers suggest increased internal resistance, and this will contribute to more consumption of active Li^+ from the cathode for the following cycling, thus accelerated aging of LIBs.

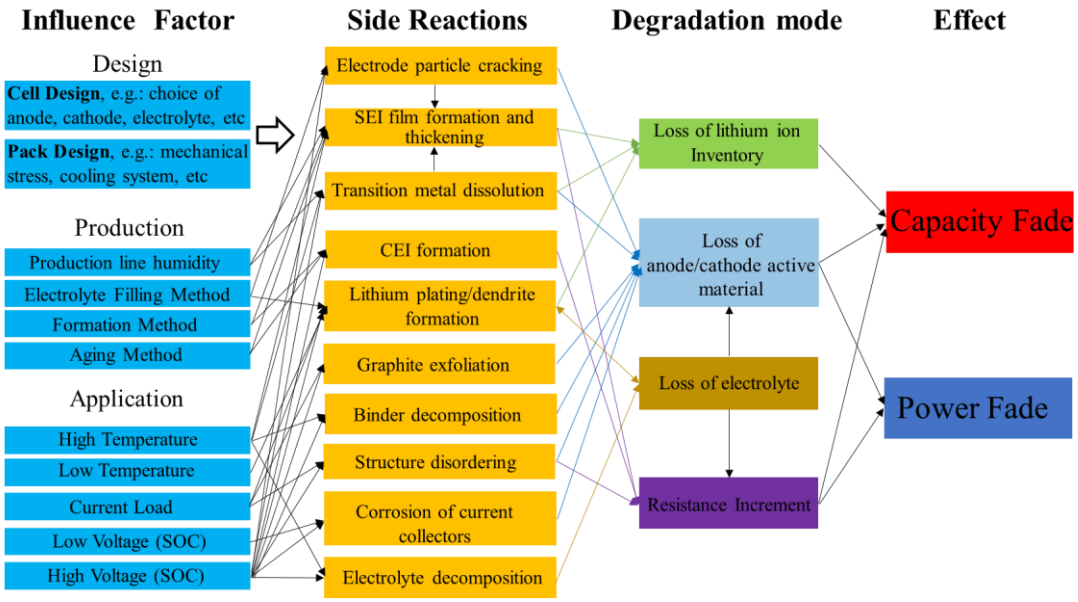

Figure 1.5. Causes and their effects on the aging of LIBs [38], adapted with permission from X. Han et al..

The loss of active Li^+ within cathode materials will permanently decrease the useable cell capacity. These active Li-ions are consumed in the formation of SEI/CEI interphases, leading to increased internal resistance and reduced power performance. Meanwhile, as electrode particles are typically enclosed by binder materials to form a network capable of both Li^+ and electron conduction, due to mechanical failure caused by cracking during the long term cycling, some electrode particles lose contact with surrounding binders during repeated cycling and will not participate the redox reaction, thus forming "dead" materials [40].

For liquid electrolytes within LIBs, as the electrochemical potential of graphite anode (0.05 V vs. Li^+/Li) lies out of the electrochemical stability window of liquid electrolyte (typically between 1.0-4.6 V vs. Li^+/Li), liquid electrolyte then experiences reduction at the electrolyte/graphite interphase, and SEI layers will be formed on the surface of graphite flakes. Ideally, a well-formed SEI layer consisting of inorganic Li_2CO_3 and LiF will hinder electrolyte

reduction as it is supposed to transport Li^+ only and will hinder the transport of electrons after initial formation cycles. Given the volume expansion/shrinkage of graphite anodes during cycling, the formed SEI layers get broken, and fresh SEI layers will form, with consumption of Li^+ from the cathode and decreased capacity. Besides issues with the SEI layer, liquid electrolyte also suffers from various side reactions, including all of these lead to the aging of liquid electrolyte with significantly reduced transport properties (Li^+ conductivity and transference number), which will trigger other failure mechanisms and accelerate the aging of LIBs [41]. Meanwhile, various additives contained in the electrolyte are also consumed, and benefits (improvement of stability) from these additives are also lost during long term cycling [42–44].

For CEI layers formed at the cathode side, it is well recognized as a more critical player in cell aging (especially for cathodes with high Nickel content within $LiTMO_2$), mainly due to the surface reconstruction on the cathode and continuous oxidation of EC. Various studies have indicated that this faster resistance growth at the cathode side via electrochemical impedance spectroscopy (EIS). As irreversible loss of Li^+ from $LiTMO_2$ cathode occurs during the initial cycles for LIBs, the rocksalt NiO layer is thus reconstructed on the surface of $LiTMO_2$ particles [45]. Although this NiO layer has been widely verified by TEM imaging of cycled cathode, debates still exist on how this NiO layer (with thickness ranging from ~ 10 to ~40 nm in various studies) leads to a significant increase of internal resistance, and systematic studies are still needed to solve this debate [46]. Meanwhile, as the CEI layer formed at the cathode surface is not capable of insulating the transport of electrons (NiO is a semiconductor, and it can also catalyze chemical reactions), continuous oxidation of EC via dehydrogenation also contributes to the growth of internal resistance. Recent studies verified this oxidation via various experiments and simulations: via systematic EIS measurements and voltage/time evolution of charge transfer resistance for a $LiCoO_2$ cell, Ryoichi Tatara et al. proposed the growth of resistance to the dehydrogenation of EC [47]; this dehydrogenation was further supported by Livia Giordano via systematic density functional theory (DFT) simulation for EC with different layered oxide cathodes [48]; combining in situ Fourier transform infrared spectroscopy (FTIR) on the evolution of compositions of liquid electrolyte with EIS for a cell, Yirui Zhang et al. concluded that the growth of impedance was caused by EC dehydrogenated into oligomers [49].

Also, complex electrochemechanics effects contribute a lot to cell aging. Due to the intrinsic layered structure of the $LiTMO_2$ cathode, it experiences cyclic first-increase-then-decrease

evolution along its *c* axis. Thus, the cathode itself experiences cyclic volume expansion/shrinkage. This will indefinitely trigger the electrochemechanics and cell aging: for example, under the considerable volume shrinkage of prime NMC particles during the Li deintercalation (charging) process, some NMC particles lose contact with current collect/other NMC particles, new interphases will form, and the side reaction of EC oxidation is thus greatly enhanced, leading to faster impedance growth. Recent publications have well summarized studies on the interplay between electrochemechanics and cell aging of LIBs [50–53].

1.4 Challenges/solutions for fast charging of LIBs

Major aspects of LIBs have been introduced, and systematic models for LIBs with dominating composite electrodes have been widely accepted, especially the Newman battery model. For the commonly utilized constant current constant voltage (CCCV) charging protocol, a larger charging current forms during the constant current (CC) stage compared to the current under the constant voltage (CV) stage. Thus, the CC stage is more efficient than the CV stage for the charging process. When the charging starts, overpotentials within electrodes and electrolytes are created, and the charged LIBs will first reach the cutoff voltage with the following voltage holding stage (CV stage). And this voltage holding stage ends once the total charging time (the CC stage plus the CV stage) reaches the set C rates. Under this CCCV charging protocol, the more significant polarization from higher C rates leads to a relatively shorter CC stage for LIBs before reaching the cutoff voltage. Thus fewer Li^+ gets intercalated into the graphite anode, and less capacity is obtained during the charging process.

Li plating, indicating the deposition of metal Li on graphite anode, not the intercalation of Li into graphite anode, is widely seen as the main issue with XFC. What is more, its occurrence could be well seen from the following equations.

$$V(i) = V_{oc} - V_{activation} - V_{ohm} - V_{concentration} \qquad (1.3)$$

$$i = kc_1^{0.5} c_s^{0.5} (c_{s,max} - c_s) \times 2\sinh\left[\frac{0.5F}{RT}(\Phi_s - \Phi_l - U)\right] \quad (1.4)$$

$$i_l = -k_{l,eff}\frac{\partial \Phi_l}{\partial x} + \frac{2k_{l,eff}\cdot RT}{F}\left(1 + \frac{\partial \ln f}{\partial \ln c_l}\right)(1 - t_+)\frac{\partial \ln c_l}{\partial x} \qquad (1.5)$$

For equation (1.3), V_{oc} represents the voltage for the open circuit; it is intrinsically determined by the voltage difference between cathode and anode materials, as we have mentioned

before. For a given LIB system, it is replaced by the fixed cutoff voltage to obtain reliable performance during its long term cycling. The $V_{activation}$ represents the overpotential needed for Li^+ to diffuse between the electrode/electrolyte interphase, and it is typically described by the Butler-Volmer equation shown in equation (1.4). The V_{ohm} is the voltage drop caused by Ohm resistance within LIBs, including effects from electron conductivity and Li^+ conductivity. For $V_{concentration}$, it includes the voltage drop within cathode/anode particles and liquid electrolyte: the voltage drop within cathode/graphite electrode could be simply described by Fick's law (in fact, the diffusion of Li^+ within graphite particles is more complex than its diffusion within cathode), and the voltage drop within liquid electrolyte is described by the concentrated solution theory, as shown in equation (1.5).

So it is seen that, under higher charging rates, the corresponding large charging current leads to significant terms of $V_{activation}$, V_{ohm}, and $V_{concentration}$. Meanwhile, the V_{oc} term is fixed, thus, the electrochemical potential at the graphite anode side gets closer to 0 under higher charging rates, leading to Li plating at the graphite anode.

Once Li plating occurs, significant challenges are confronted: (1) Given the high reactivity of plated Li metal, various side reactions, including the reduction of organic solvents and thickening of SEI layers on graphite anode, will be triggered (as shown in **Figure 1.5c**), leading to the increase of internal resistance; (2) The plated Li forms so-called "dead lithium" as they seldom participate the electrochemical reaction and this leads to the irreversible loss of active Li^+ from the cathode then permanent capacity degradation; (3) The possibility of plated Li penetrating through the polymer separator will cause the internal short to LIBs and cause serious safety issues. Thus, it is straightforward to conclude that the improvement of Li^+ transport and prevention of Li plating are the key issues to realizing fast charging of LIBs.

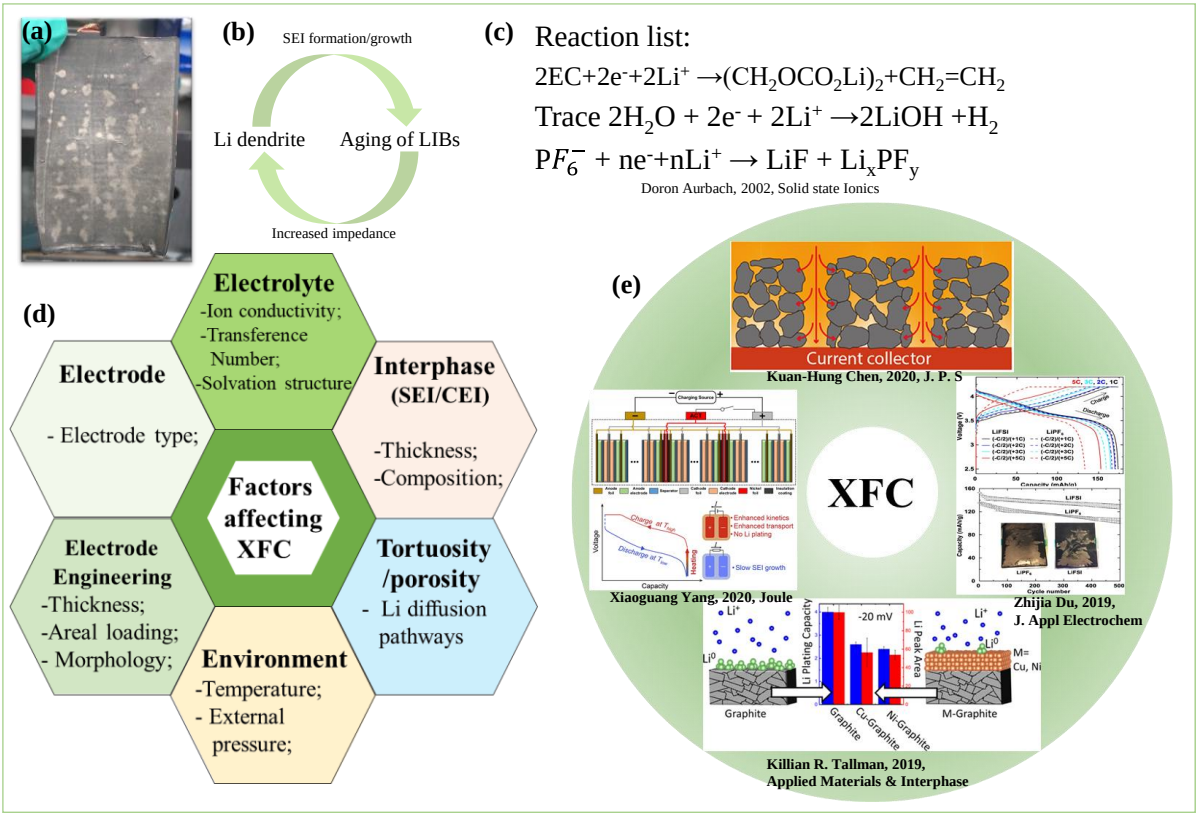

Figure 1.6. (a) Li plating on graphite anode under XFC; (b) accelerated aging of LIBs after Li plating, (c) the possible reaction of Li metal with liquid electrolyte [41]; (d) factors affecting XFC for LIBs; (e) strategies probed by the community in improving XFC performance [54–57].

To prevent/mitigate Li plating triggered by the polarization within LIBs under higher charging rates, intensive studies have been implemented by the community. As shown in **Figure 1.5d**, factors affecting the cycling performance of LIBs under XFC are well summarized, and intensive studies have been investigated for all areas of LIBs involving Li^+ transport:

(1) The improvement of tortuosity of LIBs: the macroscopic diffusivity of Li^+ within LIBs is highly related to its microstructural tortuosity. As a descriptor for the ratio of the total diffusion lengths of Li^+ diffused to the Euclidean distance between two points, tortuosity is well recognized for its effect on the macro diffusivity and resistance, thus rate/power performance of LIBs, and it is straightforward to have low tortuosity to obtain good rate/power performance. Recent studies investigated the utilization of magnetic field, freeze casting, and laser drilling to achieve this goal: by applying an external magnetic field via Fe_3O_4 particles attached to graphite flakes in the coating process, Juliette Billaud et al. successfully reduced the tortuosity within a cell and greatly improved its rate

performance [58]; through directionally freeze coating graphite anode, Dingying Dang et al. reduced the tortuosity within graphite anode and achieved 60% higher capacity at 1C than anodes manufactured from conventional tape-casting method [59]; what is more, via laser drilling of 3D patterned holes on graphite anode, Kuan-Hung Chen et al. realized a capacity retention of ~91% after 600 cycles under 4C (15 minutes) charging [54]. All these studies verify the effects of lowering tortuosity to the realization of fast charging.

(2) The enhancement of Li^+ transport properties from ion conductivity to Li^+ transference number: as polarization from liquid electrolyte contributes a lot to the total overpotential, and it is straightforward to improve the transport properties of liquid electrolyte to mitigate its polarization under large currents. Various strategies have been taken to enhance these transport properties: Xiaoguang Yang et al. heated the cell to 60 °C during the ~ 10-minutes charging, and good capacity retention of ~91.7% was achieved even after 2500 cycles, due to the enhanced Li^+ transport under this high temperature [55]; E.R. Logan et al. summarized other design strategies ranging from utilization of cosolvents with low viscosity, concentrated electrolyte, and Li salts with large polyanions [12].

(3) The improvement of SEI: besides improvement in the transport of Li^+ within bulk electrodes and liquid electrolytes, Li plating caused by fast charging could also be mitigated via enhancement of the stability of SEI layers. Killian R. Tallman et al. mitigated Li plating by ~ 50% under 6C charging via magnetron sputtering of nanoscale layers of Cu and Ni on graphite anode [56]; Sewon Park et al. improved the capacity retention for a $Li_1Ni_{0.8}Mn_{0.1}Co_{0.1}O_2$||Si cell under 3C charging by replacing conventional electrolyte additives with their newly developed electrolyte additives [60].

(4) The utilization of electrodes with higher Li^+ transport properties: besides the NMC622 and graphite electrodes utilized in this study, electrodes with higher Li^+ diffusivity will mitigate the overpotential within bulk electrodes and thus improve the rate performance of LIBs. For example, a recent study by Haodong Liu et al. on disordered rock salt $Li_{3+x}V_2O_5$ anode exhibited its capability to deliver 40% capacity within 20 seconds [61].

All these techniques indeed increase the performance of LIBs under fast charging, but they are still far away from mass application in the industry due to their intrinsic drawbacks (cost,

maturity of techniques, energy density), thus systematic investigation of both the fundamental mechanism of Li plating and more techniques to improve the rate/power performance of LIBs are urgently needed.

1.5 Experimental methods utilized in the study

In this study, pouch cells tested in this study were prepared, following the typical cell preparation procedures shown in **Figure 1.6**. Besides, various characterization methods were utilized for the study of fast charging for LIBs. Besides commonly used electrochemistry characterization methods (rate performance, long term cycling performance, EIS and so on), the following characterization techniques range from valence state of various elements (Ni, Co, Mn), evolution of interphases (SEI and CEI) to crystal structure of electrodes to have been taken:

(1) X-Ray absorbance spectroscopy (XAS): As a powerful tool in studying the valence state of elements, its working principle is relatively mature, and samples prepared in the study follow typical procedures. For LIBs experiencing fast charging, as irreversible loss of Li^+ within cathode material occurs, it is of great necessity to investigate how the valance of TM elements would evolve during this process, given their central role in the redox actions.

(2) X-ray photoemission spectroscopy (XPS): XPS is a mature tool for probing both the valence state and detailed compositions for chemicals, and the fundamental principles of XPS are well summarized in these studies [62,63]. For LIBs, XPS is commonly utilized in probing elements within the SEI/CEI layers [64]. As the interfacial stability of cosolvents utilized in this study is unknown, it is necessary to utilize this method to verify their chemical stability with NMC622 and a graphite anode.

(3) X-Ray/Neutron powder diffraction and Rietveld refinement: for LIBs, powder diffraction is the standard method for the characterization of the crystal structure of electrodes. In this study, the structural evolution of both NMC622 cathode and graphite anode was studied via this technique. Furthermore, to better understand the phase transition for LiC_{12} to LiC_6 during the Li intercalation process, sequential Rietveld refinement was implemented for a customized NMC622||graphite cylindrical cell. From the time evolution of collected diffraction data, each phase's phase fraction (weight ratio) could be well obtained quantitatively.

(4) Inductively coupled plasma-optical emission spectrometry (ICP-OES): Due to the moisture within liquid electrolytes, Li salts suffer from continuous consumption within LIBs. To quantitively probe how Li salts evolve under various charging rates, extracted electrolytes were analyzed via ICP-OES. Procedures for the experiment and following data analysis all follow the general steps implemented in a typical ICP-OES experiment.

(5) Gas chromatography-mass spectrometry (GC-MS): Compared to charging under relatively small charging rates, XFC utilizes a larger charging current, thus large current from electron moving occurs at the electrode/electrolyte interphase, leading to more severe side reactions (thus faster aging) for solvents within liquid electrolytes. As a mature technique commonly utilized by the community, in this study, GC-MS was utilized for the investigation of how Li salts and organic solvents evolve under long term cycling. And cycled electrolytes were extracted from pouch cells, and its compositions were then analyzed using GC-MS, following the procedures from Jeff Dahn's group [65,66].

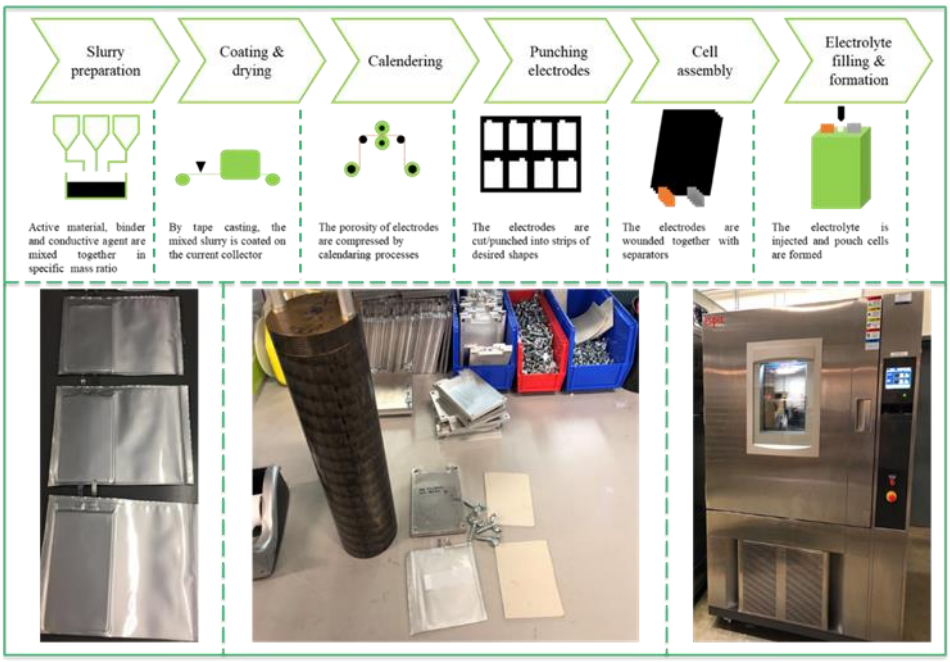

Figure 1.7. The procedures for the preparation of pouch cells tested in the study

1.6 Thesis outline

For our study, the main goal is to realize XFC for LIBs with areal loading ≥ 3 mA/cm^2 while maintaining capacity ≥ 80% after 500 cycles. Thus, chapter 2 systematically probes the effects of increasing charging rates (from 1C, 4C to 6C charging) on the whole LIB system, from the crystal structure of both NMC622 cathode, and graphite anode to cycled liquid electrolyte. Then, in chapter 3, via operando neutron powder diffraction (NPD) experiment on a home-made NMC622||graphite cylindrical cell, the structural evolution of NMC622 cathode (lattice parameters *a* and *c* with Li contents within NMC622) and phase transition of lithiated graphite under increasing charging rates were studied systematically. In chapter 4, various cosolvents, ranging from dimethyl carbonate (DMC), ethyl acetate (EA), and methyl acetate (MA) to ethyl formate (EF), were systematically tested for their effects on the whole LIBs system under extreme fast charging: from rate/long term cycling performance.

2. EFFECTS OF CHARGING RATES ON $LINI_{0.6}MN_{0.2}CO_{0.2}O_2$ (NMC622)/GRAPHITE LI-ION CELLS

This chapter is from the following publication: **Wu, Xianyang**, et al. "Effects of charging rates on $LiNi_{0.6}Mn_{0.2}Co_{0.2}O_2$ (NMC622)/graphite Li-ion cells." *Journal of Energy Chemistry* 56 (**2021**): 121-126.

Contributions

Xianyang Wu: Design and implementation of experiment, data post-processing, writing, reviewing, and editing of original draft.

Yaocai Bai: Implementation of ICP-OES experiment, editing of original draft.

Zhenglong Li: Data analysis and editing of original draft.

Jue Liu: Implementation of NPD experiment, data analysis, editing of original draft.

Kejie Zhao: Conception and design of experiment, reviewing, and editing of original draft.

Zhijia Du: Conception and design of experiment, reviewing, and editing of original draft.

2.1 Introduction

The development of Li-ion cells with fast-charging capability is critical to further progress the widespread of electric vehicles [67]. The charging of an electric vehicle should ideally cost a similar amount of time compared to refueling a gasoline engine vehicle, which is 15 minutes or less. High-power Li-ion cells with thin electrodes are capable of recharging in short time (10~15 minutes). However, these cells have lower energy density and would lead to higher cell cost compared to state-of-the-art high energy density cells. A calculation by Ahmed et al. found a 10 minutes fast charging cell design with 19 μm thick anode increase the cell cost sharply to $ 196/kWh, compared to $107/kWh with 87 μm thick anode capable of 47 minute charging [68]. In the high energy density Li-ion cells, fast charging can adversely lead to degradation in battery safety, energy density and cycle life.

Li plating has been identified as one of the most critical issues affecting battery performance [68–73]. It occurs on the surface of the graphite electrode when large overpotentials in a cell decrease the local potential to below 0 V (vs. Li^+/Li) [74–76]. Gallagher et al. have systematically studied the effect of electrode loading (thickness) and charging rate on Li plating [77]. It was found a relatively moderate charging rate of 1.5 C (40 minutes charging) can have significant impact on

Li-ion cells with 3.3 mAh/cm^2 loading, leading to capacity decrease and metallic Li deposition. Li plating can result in irreversible capacity loss due to the removal of active Li inventory in the cell [78]. Fully discharging of the cells with Li plating even at a low rate did not strip the deposited Li back to the positive electrode [77]. Another issue with Li plating is its high tendency to form dendrites with high surface area, which increase the parasitic reactions with electrolyte, forming isolated (dead) lithium, and thus reducing the Coulombic efficiency [79–81]. Li dendrite would also short the cell, cause catastrophic failure of the battery, and even inducing fatal safety hazards [82–85].

Fast charging can also lead to rapid temperature rise from the high heat generation rate due to the large current applied to the cell. With embedded thermal couple in a 2-Ah pouch cell, Huang et al. observed the temperature of the cell rose from room temperature (23 °C) to 38 °C under 5C charging rate and 45 °C under 7C within 5 minutes [86]. This increased temperature can result in a decrease of the cell resistance to improve kinetics. Yang et al. have shown the cell performance during fast charging can be improved by intentionally heat the cell by internal heaters [87]. However, performance degradation can be aggravated by exposing the cell to elevated operation temperature. This is because parasitic reactions, like SEI growth, are intensified with increased temperatures [78]. Increase in the temperature can also worsen other unwanted reactions such as transition metal dissolution and binder decomposition [88,89].

In the present study, we study the effects of fast charging (+1C, +4C and +6C) on the capacity fading, electrode microstructural changes and electrolyte changes in $LiNi_{0.6}Mn_{0.2}Co_{0.2}O_2$ (NMC622) /graphite pouch cells. A detailed post-mortem analysis is performed to study the aging under different fast charging rates via electrochemical testing, neutron powder diffraction, inductively coupled plasma atomic emission spectroscopy (ICP-OES), gas chromatography–mass spectrometry (GC-MS), etc.

2.2 Experiments

Electrodes and pouch cells with capacity of 400 mAh were prepared in a dry room (dew point < -50 °C) at the DOE Battery Manufacturing R&D Facility (BMF) at Oak Ridge National Laboratory (ORNL). The cathode was NMC622 (Targray) electrodes with 2.3 mAh/cm^2 areal capacity loading and calendered to 30% porosity. The anode was graphite (Superior Graphite 1520T) electrodes with 2.6 mAh/cm^2 areal loading and calendered to 30% porosity. The electrolyte

filled into the pouch cell was 1.2 M $LiPF_6$ in ethylene carbonate (EC): ethyl methyl carbonate (EMC) 3:7 by weight (*soul*brain MI).

The cell cycling was carried out on a battery cycler, Maccor Series 4000, in an environmental chamber at 30 °C. The cells were cycled between 2.8 and 4.2 V with a constant voltage holding at 4.2 V (trickle charging). A total time limit was imposed to guarantee that the duration of the charging step did not exceed the intended time for each C rate (10 minutes for 6C charging, 15 minutes for 4C, and 1 hour for 1C charging). Half coin cells were built to test the Li inventory loss in cathodes. Both NMC622 cathode and graphite anode electrodes were punched from aged NMC622 pouch cells after disassembling in the Ar-filled glove box. The electrodes were then assembled into Li coin cells with Li metal as the counter electrodes. The electrolyte was fresh electrolyte, and the half coin cells were charged and discharged at a constant rate of C/10 between 2.5 V and 4.2 V.

NMC and graphite powder samples were collected from the electrodes after discharging the cell to 2.0 V and disassembled in Ar-filled glove box. Room temperature neutron total scattering data were collected at the NOMAD beamline at the Spallation Neutron Source (SNS) at ORNL [90]. About 3.0 g powder sample was loaded into a 3 mm quartz capillary. The detectors were calibrated using scattering from a diamond powder standard prior to the measurements. The average structure refinements using neutron diffraction data were carried out in TOPAS Academic, version 6 [91].

The gas generation during fast charging cycles was studied by using Archimedes principle, similar to previous report [92]. The cells were hung below an analytical balance and suspended in silicone mechanical pump oil at room temperature. The test was carried out after 50 cycles and 200 cycles.

The electrolyte after long-term cycling was analyzed by ICP-OES following a similar procedure reported by Thompson et al. [93]. The pouch cells after cycling were cut open in the dry room and sealed in centrifuge tube, then they were centrifuged under 2000 rpm for 20 minutes to extract cycled electrolyte. The extracted liquid electrolyte (~ 0.10 g) was first diluted with ~ 20 grams of 2 wt% HNO_3 with ~ 0.2 g CH_2Cl_2 added for organic separation. The 1st diluted solution was then centrifuged under 2000 rpm for 30 minutes for fully extraction of Li^+ into the aqueous HNO_3 and phase separation. Then ~ 1 g of 1st diluted solution from the top layer was added into ~

10 g 2% HNO_3 and shaken for 15 minutes. The 2nd diluted solution was then analyzed using Agilent Technologies 5110 ICP-OES to obtain the different elemental concentrations.

GC-MS was used to analyze the composition changes in the electrolyte solvents after long term fast charging cycles. One drop of the recovered electrolyte from cycled pouch cell was diluted in polytetrafluoroethylene vials with ~15 mL of CH_2Cl_2 and ~0.1 mL deionized water for the complete extraction of Li salts [65,93]. The vial was machine-shaken for 30 minutes in two directions and centrifuged for 30 minutes under 2000 rpm for complete separation. The organic layer (electrolyte solvents in CH_2Cl_2) was removed by diluting into CH_2Cl_2 again, followed by another machine-shaken of 15 minutes. The organic layer was then analyzed by an Agilent 6850 GC−MS system. The GC inlet temperature is 250 °C with a split ratio of 1:10. Carrier gas was helium at a linear velocity of 1.5 mL/min. The column temperature started at 40 °C and ramped up to 250 °C at a heating rate of 8 °C/minute. The interface and ion source temperature for MS were 250 and 200 °C, respectively. The morphology of the electrode was characterized by a scanning electron microscope (SEM, Carl Zeiss Merlin).

2.3 Results and Discussion

Figure 2.1a shows the cycling performance of the NMC622/graphite pouch cell under different charging rates of 1C, 4C and 6C. The capacity shown on the Y-axis is based on the mass of the cathode materials NMC622. The capacity retentions after 200 cycles (compared the 1st cycle) are 94.0%, 89.4% and 73.8% under 1C, 4C and 6C charging rate, respectively. **Figure 2.1b** shows the voltage curves of cells at the 1st, 50th and 200th cycles under different charging rates. During the 1st cycle, the capacities of the cell (corresponding to the mass of NMC622) are 164, 152 and 143 mAh/g under 1C, 4C and 6C charging rates, respectively. Huge polarization is observed with increasing the charge current from 1C to 6C. The capacity decreases under increasing charging current are due to the mass transport limitation in electrolyte and/or sluggish diffusion kinetics in graphite [77,94,95].

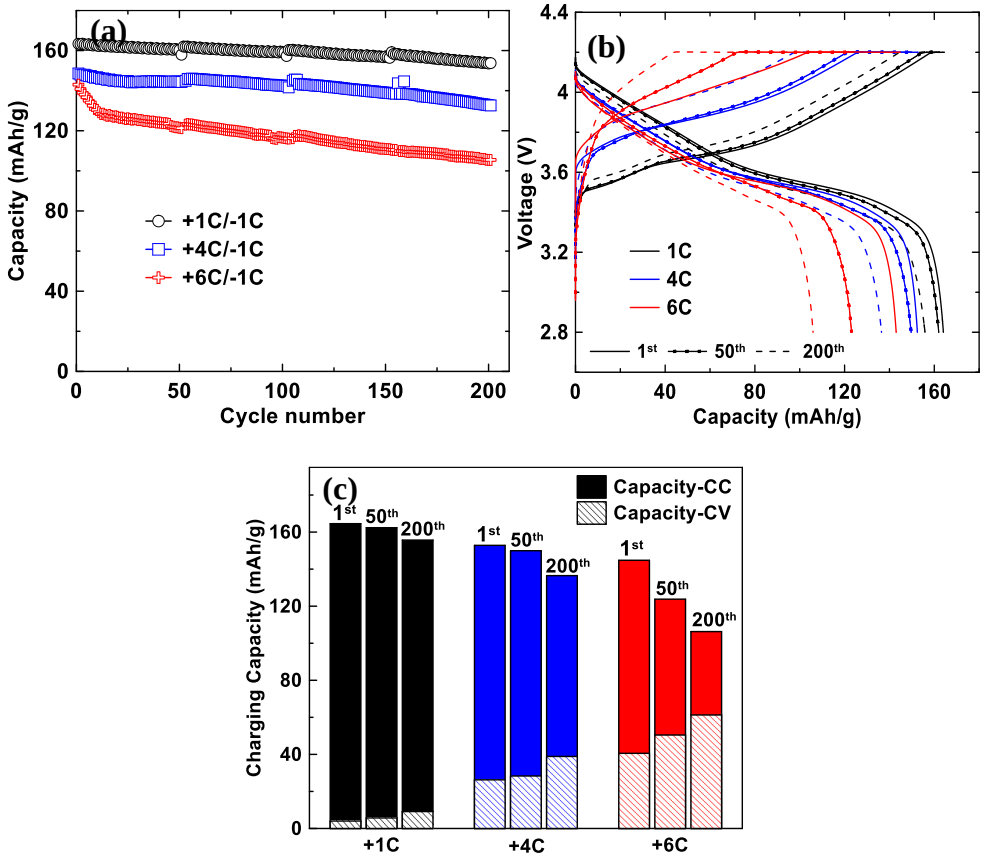

Figure 2.1. electrochemical performance of NMC622/graphite pouch cell under different charging rates. (a) cycling performance; (b) voltage curves at 1st, 50th and 200th cycle; (c) capacity from constant current charging and capacity from constant voltage charging at 1st, 50th and 200th cycle.

Figure 2.1c shows the capacities of the cells obtained within the specified time (60 minutes for 1C, 15 minutes for 4C and 10 minutes for 6C) from the 1st, 50th and 200th cycles. The capacities consist of capacity from the constant current (capacity-CC) charging and that from the constant voltage (capacity-CV) charging. The portion of capacity-CV in total capacity increases significantly with the increase of charging current. It also increases with the cycling number, indicating continuous aging and increasing polarization in the cell. Under 6C charging after 200 cycles, more than 50% of the total capacity is from capacity-CV. This high voltage operation has been reported to cause more degradation in Li-ion cells [96,97].

Figure 2.2a shows the bank 4 neutron diffraction patterns of the cathode at fully discharged states after 200 cycles under different charging rates. In general, the layered structure of the NMC materials is well maintained when fitted with the $R\bar{3}m$ [166] space group. However, peak shifting and intensity changes can still be noticed. For example, **Figure 2.2b** shows the local magnification

of (108) and (110) peaks which are directly related to the *a* and *c* value of the unit cell. The shifting of (108) to lower *d* spacing while (110) shifting to higher *d* spacing with increasing charging rates indicates the increase of *c* and decrease of *a*. This is also shown in **Figure 2.2c** of the unit cell parameters derived from the refinement of neutron diffraction data. The structural expansion along *c* direction indicates the loss of Li ions in the lithium slabs which increases the repulsive force between adjacent oxygen slabs. The increase of *c* with the increase of charging rates indicates less Li ion inventory available for faster charging after long-term cycles. Bond length information is shown in **Figure 2.2d**, and the absolute values of the bond lengths reveal only slight changes from pristine state to fully discharged states after repeated cycling. However, the trend in changes can be explained by the loss of Li inventory in the Li ion slab, and these changes demonstrate the fast charging at 6C rate leads to the most Li loss after cycling. Figure S1 shows the neutron powder diffraction of graphite after 200 cycles. The diffraction patterns are the same as pristine graphite and can be indexed to space group $P6_3/mmc$. This demonstrates electrode structural changes mainly occurs in the cathode materials during cell aging, which is consistent with previous reports [98,99].

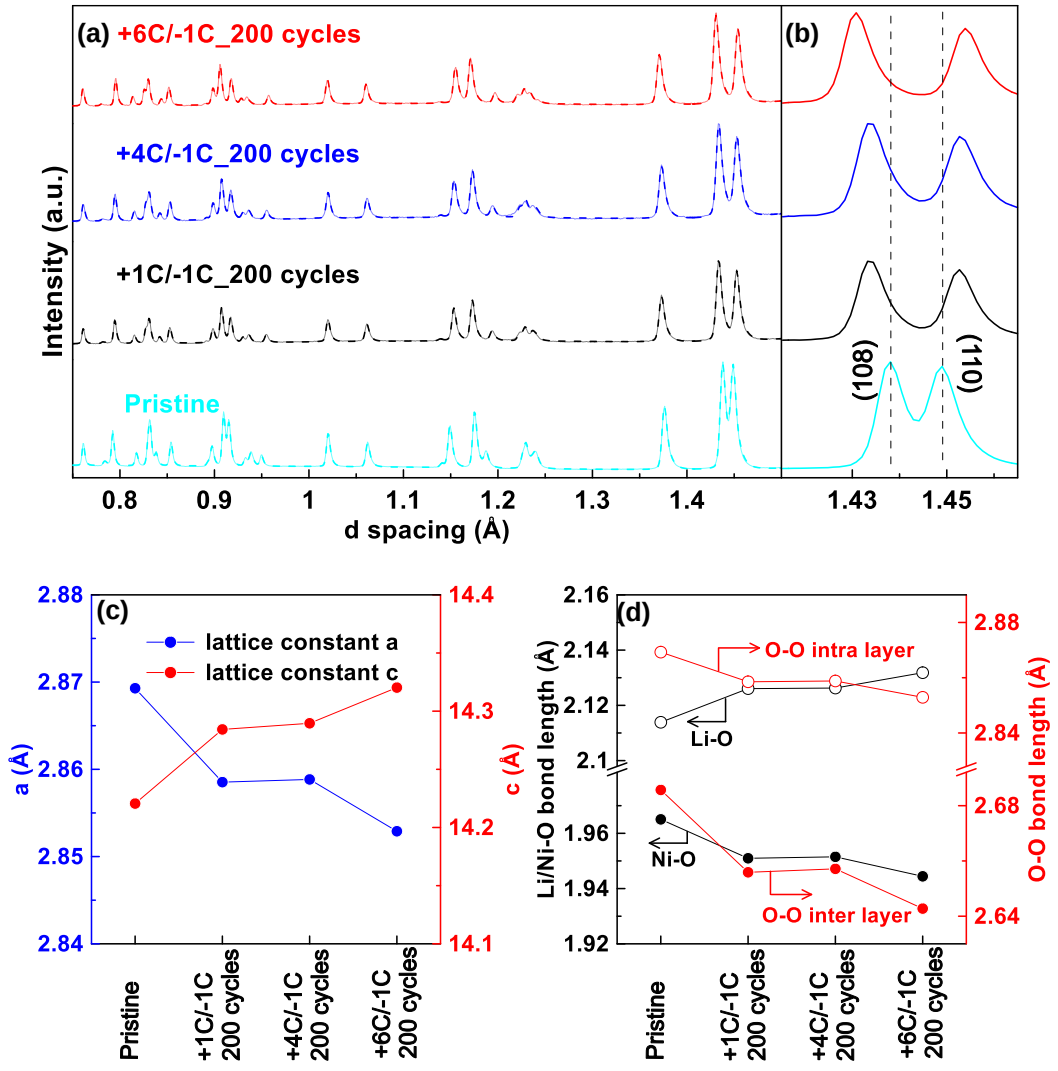

Figure 2.2. (a) Neutron power diffraction and the Rietveld refinement fitting to the curves. (b) Diffraction patterns showing the shifting of (108) and (110) peaks. (c) Lattice parameters of a and c from the Rietveld refinement. (d) Ni-O, Li-O, O-O intra layer, and O-O interlayer bond lengths.

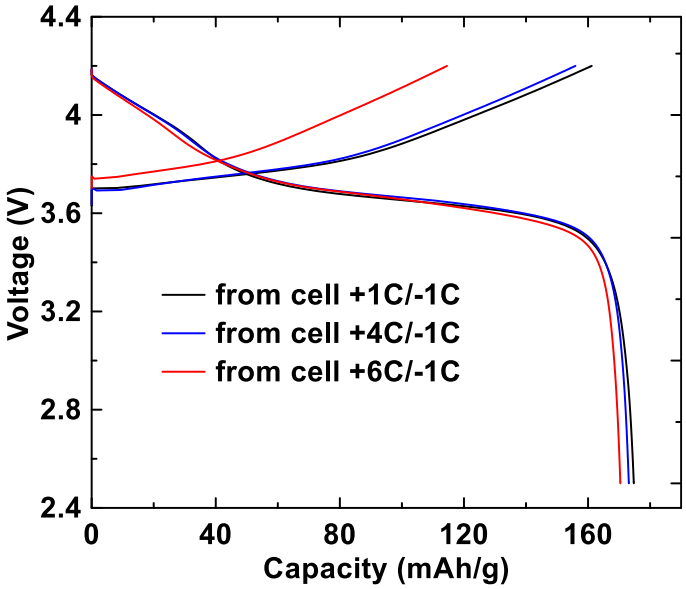

Figure 2.3. Voltage curves of Li coin cells assembled with NMC622 cathode after 200 cycles under +1C/-1C, +4C/-1C and +6C/-1C charge/discharge rates. The material was delithiated first and then lithiated at a constant rate of C/10 between 2.5 and 4.2 V.

To confirm the Li inventory loss after long-term cycling and evaluate the reversibility of the cathode structures, coin cells were made from the aged NMC622 cathodes with fresh Li counter electrodes and electrolyte as shown in **Figure 2.3**. The cells were charged and then discharged to assess the Li inventory left in the structure and Li ions that can be intercalated back. The 1st charge capacities of the cells are 161, 156, and 115 mAh/g for 1C, 4C and 6C, respectively. This is in accordance with the neutron diffraction result that higher charging rate leads to more Li inventory loss during cycling. However, all the three cells show similar discharge capacity of 171-175 mAh/g, indicating the reversibility of the cathode structure for Li intercalation/de-intercalation is not affected by fast charging. Figure S2 shows the voltage curves of the aged graphite electrodes in reassembled Li coin cells, which overlaps well with each other regardless of the charging rates during pouch cell aging. This indicates the graphite electrode has good structural integrity without exfoliation or disordering from rapid lithium intercalation during fast charging.

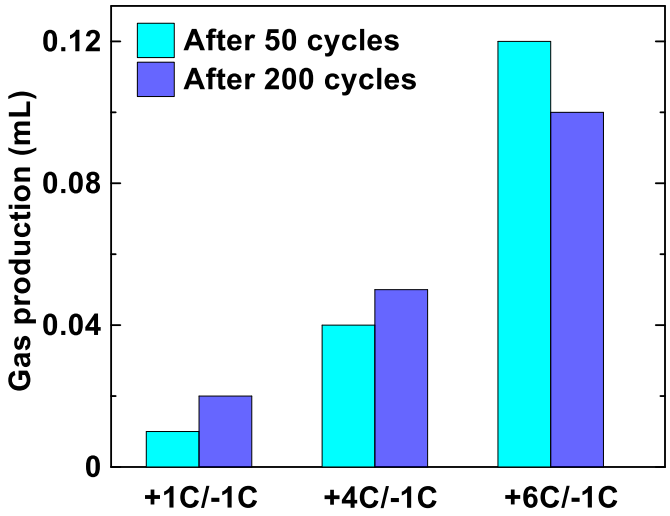

Figure 2.4. Comparison of the gas volume measured by Archimedes' principle under different charging rates. The pouch cells have an initial cell volume of ~4.0 mL.

Figure 2.4 shows the gas production of the cells after 50th and 200th cycles under different charging rates. Gas generation during cell aging is mainly from the decomposition of the electrolyte at the electrode/electrolyte interfaces [100–102]. A general trend in **Figure 2.4** is that the gas production increases with the increase of charging rate. The cell under +6C/-1C charge/discharge rate shows more gas production after 50 cycles than after 200 cycles. We believe this phenomenon can be explained by the cathode-anode cross-talk during cell aging. The gas generated from one electrode can migrate to the other electrode, and the gas generated in initial cycles can be gradually consumed in the following cycles, either electrochemically or chemically [103–105]. In this study, the scale of the gas production is relatively small (0.02-0.12 mL) compared to the total cell volume of ~4.0 mL. This is also the case in previous report when cells were cycled at a moderate rate (C/3) [93]. Therefore, gas production in the cells is not considered as an issue for fast charging of the cells within normal voltage range (2.8-4.2 V).

Figure 2.5 shows Li ion molarity in electrolytes from ICP-OES measurement after 200 cycles under different charging rates. The molarity is slightly increased in all three cases, which contrasts with the report by Thompson et al. which shows a slight decrease in molarity for cells cycled at a moderate rate of C/3 [93]. This suggests that the solvent has been consumed at a slightly higher rate compared to Li ions in the cells. Nonetheless, the relative change of the Li molarity is small (within 8%). Transition metal ion concentration was also measured in the ICP-OES test, all

the three elements (Ni, Co and Mn) were below 10 ppm or detection limits. Therefore, fast charging has no impact on the transition metal ion dissolution from the crystal structure.

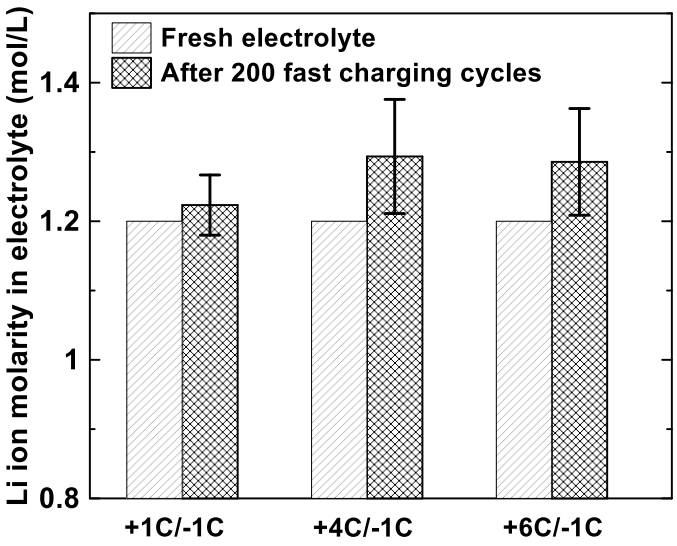

Figure 2.5. Changes in Li ion molarity in the electrolyte after 200 cycles under different charging rates.

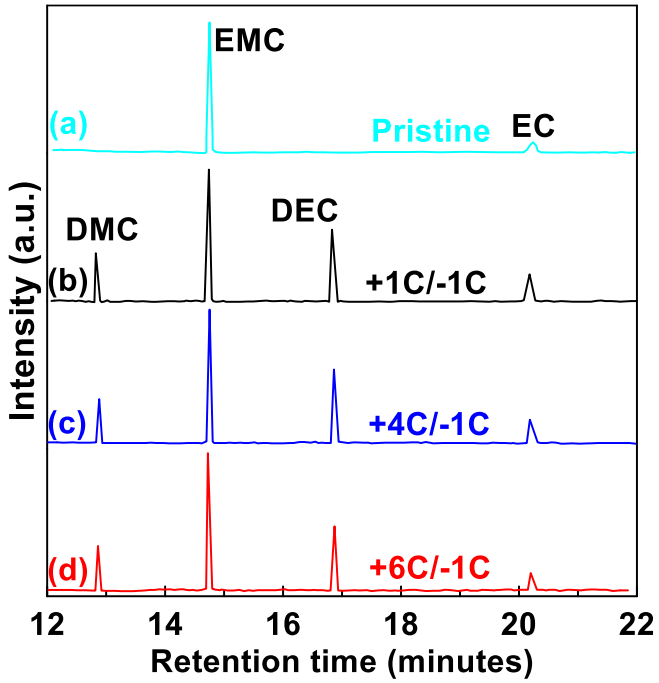

Figure 2.6. Chromatogram of (a) pristine electrolyte, (b) electrolyte after 200 +1C/-1C cycles, (c) electrolyte after 200 +4C/-1C cycles, (d) electrolyte after 200 +6C/-1C cycles.

Figure 2.6 shows the corresponding chromatograms of different electrolyte samples analyzed by GC-MS. The carrying solvent, dichloromethane, has a huge peak at a retention time of 10.65 minutes, and was not included in this figure for better clarity on the carbonate solvents in Li-ion electrolyte. In conjunction with MS analysis (Figure S3) on the retention peaks, the following peaks are assigned to dimethyl carbonate (DMC), EMC, diethyl carbonate (DEC) and EC at 12.80, 14.75, 16.80, and 20.20 minutes, respectively. In the pristine electrolyte sample, only EMC and EC are presented in **Figure 2.6a**, in consistent with its constituents. However, DMC and DEC are generated via the transesterification of EMC after repeated cycles in all cases under different charging rate. The presence of Li-alkoxides, one of the reduction products from EMC on anode/electrolyte interface, is speculated to facilitate the transesterification reaction as firstly reported by Yoshida et al. [106]. This transesterification has been extensively reported in cells with slow and/or moderate charging rates [65,93,107]. Although the GC-MS method used in this study is semiquantitative, the tentative conclusion is that transesterification decrease with the increase of charging rate. This agrees with previous report that electrolyte reduction (SEI growth) follows a parabolic growth law, which means time [78], not cycle count, dominates the parasitic reaction. With cycling counts the same, faster charging rate has less time in total, which, in turn, leads to less transesterification in the electrolyte.

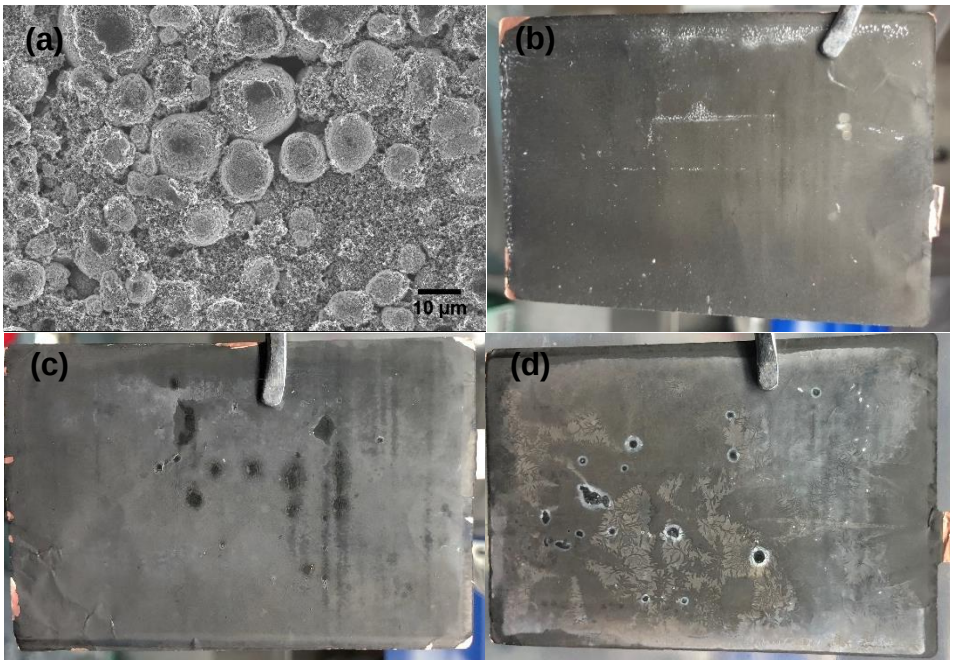

Figure 2.7. (a) SEM image of the NMC622 electrode after 200 +6C/-1C cycles. Digital photos of the graphite electrodes after 200 cycles under (b) +1C/-1C, (c) +4C/-1C, and (d) +6C/-1C, respectively.

Figure 2.7a shows the morphology of the NMC622 cathode after 200 +6C/-1C cycles. NMC622 secondary particles dispersed well in the carbon black matrix with good structural integrity. This SEM image has little difference from the electrodes after 200 cycles under +1C/-1C or +4C/-1C rates (Figure S4). As discussed above, the capacity loss is mainly from the Li inventory loss in the layered crystal structures, not from loss of active material. **Figure 2.7b, c** and **d** show the digital photos of the graphite electrodes after 200 cycles under +1C/-1C, +4C/-1C and +6C/-1C, respectively. The cells were disassembled at fully discharged state and was kept inside the Ar-filled glove box. The surface color changed from the grey of graphite for +1C/-1C to pale white for +6C/-1C, with the +4C/-1C in-between. This is in consistent with the cycling performance in **Figure 2.1**. With the increase of charging rate, more capacity fading is observed due to Li ion mass transport limitation [57,77,94]. Metallic Li plating leads to more parasitic reaction due to its high reactivity and "dead" lithium from electrical disconnection to graphite electrode. This also explains the Li inventory loss in the cathode in **Figure 2.2**, which converted into the Li plating in high charging rate cells.

2.4 Conclusions

Pouch cells with a moderate loading of 2.3 mAh/cm^2 were tested under different charging rates at 1C, 4C and 6C to evaluate its fast charging capabilities. Rapid capacity deterioration was observed for extreme fast charging (6C) cells with only 73.8% capacity retention after 200 cycles compared to 94.0% and 89.4% for 1C and 4C, respectively. An increasing portion of capacity for 6C was obtained from the high voltage (4.2V) trickle charging. Post-mortem analysis on the cathode materials indicated Li inventory loss from the Li slab in the layered structure with a shrinkage of *a* and expansion of *c*. Li coin cell test using the aged NMC622 electrodes confirmed the Li loss. However, the cathode structure was not compromised as Li can be reversibly intercalated/de-intercalated in the structure once the Li inventory was replenished. The electrolyte in the aged cells showed a slight increase of Li molarity, indicating a higher consuming rate of solvent compared to Li salt in the electrolyte. GC-MS analysis on the electrolyte solvents observed less transesterification when higher charging rate was applied, which was attributed to the less charge time for higher charging rate. Metallic Li plating was severer at higher charging rate, which accounted for the Li inventory loss in the cell. These findings deepen the understanding on cell aging mechanism when fast charging was applied and can be used as benchmarks for future improvement studies.

3. STRUCTURAL EVOLUTION AND TRANSITION DYNAMICS IN LITHIUM ION BATTERY UNDER FAST CHARGING: AN OPERANDO NEUTRON DIFFRACTION INVESTIGATION

This chapter is from the following publication: **Wu, Xianyang**, et al. "Structural Evolution and Transition Dynamics in Lithium Ion Battery under Fast Charging: An Operando Neutron Diffraction Investigation." *Advanced Science* 8.21 (**2021**): 2102318.

Contributions

Xianyang Wu: Design and implementation of experiment, data processing, writing, reviewing, and editing of original draft.

Bohang Song: Conception and design of experiment, reviewing, and editing of original draft.

Po-Hsiu Chien: Data analysis, editing of original draft.

S Michelle Everett: Reviewing, editing of original draft.

Kejie Zhao: Conception and design of experiment, reviewing, and editing of original draft.

Jue Liu: Conception and design of experiment, reviewing, and editing of original draft.

Zhijia Du: Conception and design of experiment, reviewing, and editing of original draft.

3.1 Introduction

Since its first commercialization by Sony in 1991, Li-ion batteries (LIBs) have dominated the portable electronic markets during the past 30 years [108]. These days, the huge demand from electrical vehicles (EVs) market challenges the state-of-the-art LIB technologies for higher energy density and shorter charging time to less than 15 minutes [10], to ease the range anxiety and promote the adoption of LIBs in EV markets. Utilization of realistic loading electrodes (3-4 mAh/cm^2) has been well proven as an effective way of increasing the cell energy density [77,94]. However, the caveat is that thicker electrodes prevent the cell from fast charging, which can lead to unwanted Li plating and eventual cell failure [109–111]. It is generally recognized that the limiting factor of fast charging is the limited transport property of Li^+ in electrolytes and/or graphite anode. Under fast charging (high C rate) conditions, Li^+ concentration gradient builds up in both the electrolyte and graphite, leading to insufficient lithiation of graphite and Li plating on graphite electrode. Several approaches have been reported to improve the fast charging performance of LIBs via improving Li^+ mass transport at the graphite electrode side, including

advanced electrolyte formulation, asymmetric temperature modulation, and laser-patterned electrode architectures [112–114]. Anode overpotential control via interfacial modification has also been reported to suppress Li plating during fast charging [56]. While these studies shed light on improvements of fast charging, the structural evolution of electrode materials (both the layered cathode and anode materials) during fast charging has not been systematically studied. Further investigation, especially under operando conditions, is highly needed.

For fast charging of LIBs, as the challenge comes mainly from the Li^+ diffusion/intercalation at the graphite anode side in a nonequilibrium fashion, the intercalation of Li^+ into graphite via staging has been intensively investigated [115]. From the domain model proposed by Daumas and Herald to the Cahn-Hilliard type phase-field model, they provide solid mechanistic understanding and explanation of the staging transition during lithium intercalation [116–118]. Valuable insights on the staging process have been elaborated from various characterization methods. Electrochemical methods (EIS, PITT, and GITT) were reported to obtain valuable information on the kinetic behaviors of the Li intercalation [119–124]. Semi-quantitative studies on the Li^+ transport within graphite were reported by observing the color changes for lithiated graphite at different state of charges via optical imaging [125–129]. The qualitative structural evolutions and stagings during intercalation were also widely probed via in-situ/ex-situ Raman spectra [130–138]; other experimental methods such as NMR, in situ X-ray/synchrotron and neutron powder diffraction (NPD) also provide insightful qualitative information on the Li^+ intercalation [139–142]. However, detailed quantitative information about the structural evolution of graphite staging phases, especially under fast charging conditions, is still lacking.

X-ray and neutron powder diffraction techniques have been well developed due to their unique capability on structural characterization [143–148]. For applications of in situ/operando X-ray powder diffraction on LIBs under fast charging, encouraging progresses have been made recently from two groups via high speed synchrotron diffraction with spatial resolution at micron scale on thick graphite anodes. Koffi P. C. Yao et al. quantified the Li^+ concentration gradient and staging kinetics within a 114 μm thick graphite anode under up to 1 C charging [149]. Donal P. Finegan et al. obtained temporal and spatial distribution of graphite intercalation compounds (GICs) and plated Li metal for a 101 μm thick graphite anode under up to 6 C charging [150]. Then they quantitatively analyzed the kinetics of phase transition and the heterogeneities of Li plating. For NPD techniques, in situ NPD has been applied to the study of LIBs ever since early 2000 [151–

154]. Compared to the widely used synchrotron X-ray diffraction techniques for the structural characterization of LIBs, NPD has the following unique advantages: (1) strong penetration and no heating effect; the heating effect from high energy photons often leads to inhomogeneous or delayed electrochemical reactions within LIBs, despite improved signal-to-noise ratio as a result of the very high flux photons; (2) neutron scattering lengths are constant as a function of momentum transfer (***Q***), which helps to better quantify the site occupancies and atomic displacements; (3) NPD can detect light elements in the electrode materials, especially carbon and oxygen, which play a pivotal role in the structural evolution for $LiNi_{1-x-y}Mn_xCo_yO_2$ (NMC) cathode materials and graphite anodes; (4) NPD can distinguish adjacent transition metal ions such as Ni, Co, and Mn, which is an otherwise challenging task to cope with when using conventional X-ray diffraction [155–158]. Despite these great advantages, the broad application of NPD has been hindered by the relatively lower neutron flux and the larger amount of materials needed. Also, it suffers from large incoherent scattering from hydrogen-rich organic electrolyte, and scarce neutron beam time [144].

Despite the above challenges, steady progress has been made in improving the capability of in situ/operando neutron diffraction in the past decade. For instance, Neeraj Sharma et al. investigated the phase transition of Li_xC_6 via operando NPD study by overcharging a commercial 18650 cell to ~ 4.6 V [159]. Lucien Boulet-Roblin et al. studied a $LiNi_{0.5}Mn_{1.5}O_4$ (LNMO) || graphite cylindrical cell filled with deuterated electrolyte, and they were able to reveal the evolution of lattice parameters of both the LNMO and graphite phases [147]. Laura Vitoux et al. designed a $LiNi_{0.6}Mn_{0.2}Co_{0.2}O_2$ (NMC622) || Li cylindrical cell with the capability of repeated cycling up to 60 cycles, and the signal-to-noise ratio was good enough to extract the structure information of NMC622 [160]. Jörn Wilhelm et al. probed the low temperature operation of a pouch cell under various discharging rates and following relaxation via in situ NPD, and by studying the co-existence of LiC_{12} and LiC_{18} phases, they elaborated the inhomogeneous lithiation within the graphite anode at low temperature [161]. Yet, collecting structural refinable operando neutron diffraction data under fast charging conditions is still extremely challenging, in large part due to the relatively long data acquisition time required at many neutron powder diffractometers [162,163]. Recently, we successfully commissioned the operando neutron diffraction study of batteries at the Spallation Neutron Source (SNS)'s NOMAD beamline. The high incident neutron flux together with very large detector coverage at NOMAD enables the very fast collection (< 1

min/pattern) of high quality operando neutron diffraction data from the newly designed cylindrical cell. This inspires us to carry out a systematic investigation of the structural evolution of NMC622 and graphite electrodes during fast charging.

All the information obtained (lattice structure, phase ratio and their time evolution) is vitally important for advancing the fast charging technologies of LIBs. Thus, the operando neutron diffraction capability developed by our group offers a unique opportunity to address those aforementioned issues/challenges. In this study, a customized cylindrical cell of NMC622 || graphite was used for fast operando neutron diffraction under various charging rates from 0.27 C to 4.4 C. Structural changes in both NMC622 and graphite are obtained and analyzed using sequential Rietveld refinements. The phase transition from stage II (LiC_{12}) to stage I (LiC_6) is demonstrated to be the rate-limiting step during Li intercalation into graphite under fast charging conditions. The dynamics of $LiC_{12} \rightarrow LiC_6$ transition is further investigated via the classical Johnson-Mehl-Avrami-Kolmogorov (JMAK) model, which is found to follow a one-dimension diffusion-controlled growth mechanism. These findings provide fundamental insights for further optimizing graphite-based anode for fast charging Li-ion batteries.

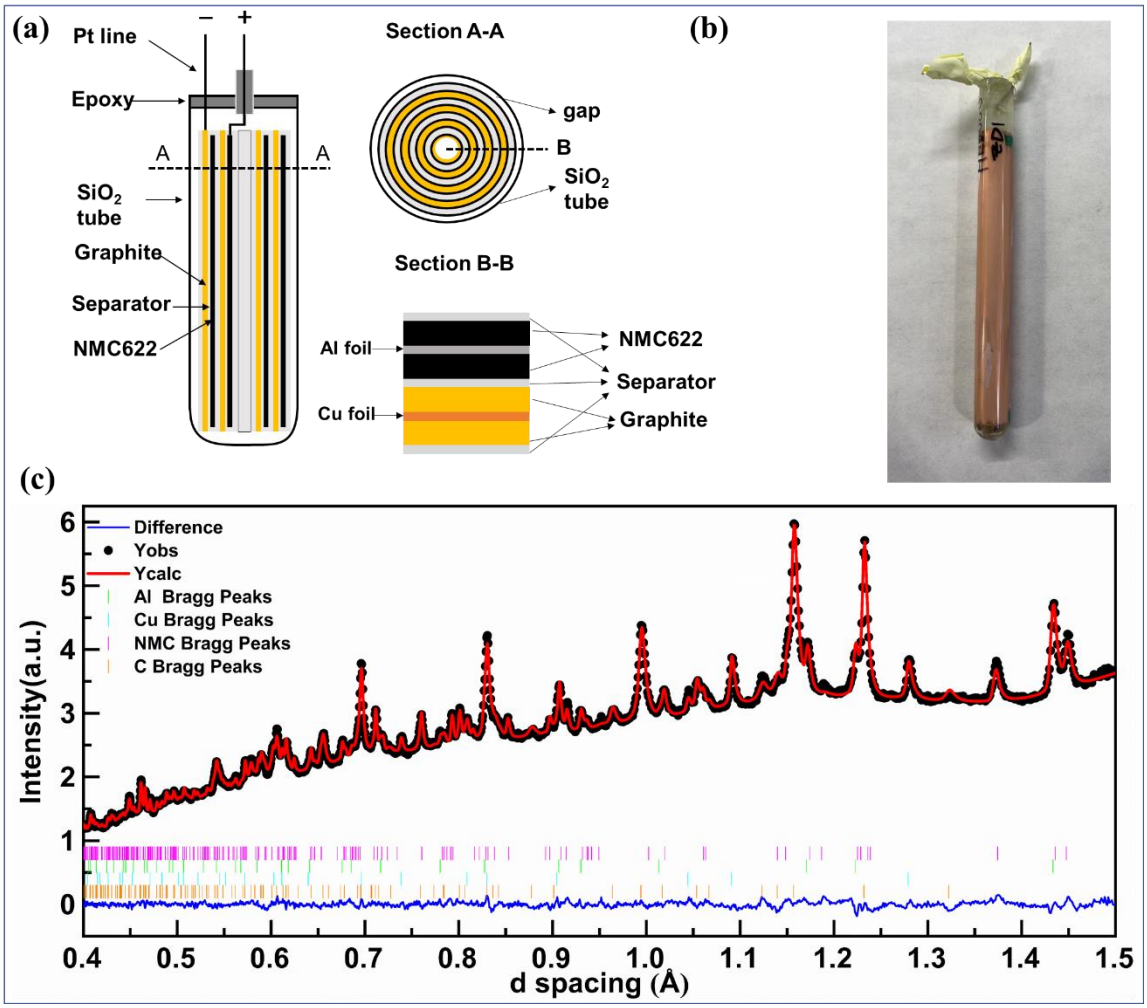

Figure 3.1. Experimental set-up for the operando neutron diffraction experiments: (a) schematic illustration of the cylindrical cell; (b) a typical cylindrical cell utilized in the operando experiment; (c) Rietveld refinement on collected NPD data.

3.2 Results and discussion

The NMC622 || graphite cylindrical cell was prepared at the DOE Battery Manufacturing R&D Facility (BMF) at Oak Ridge National Laboratory. The NMC622 electrode consisted of 3 wt % carbon black (Denka Li-100), 3 wt % polyvinylidene fluoride (PVDF, Solvay 5130), and 94 wt % NMC622 (Targray). The areal capacity was 2.78 mAh/cm2 with 30% porosity after calendaring. The thickness of NMC622 cathode and graphite anode was 57 μm and 59 μm, respectively. The graphite electrode consisted of 5 wt% of PVDF (KUREHA KF9300), 1 wt% of carbon black (Denka Li-100), and 94 wt% of graphite (Superior graphite, 1506T). The negative/positive (N/P) ratio was set at 1.1. The jelly roll was prepared by sandwiching the cathode

and anode with the separator (Celgard 2325). A thin-walled quartz tube was used to contain the jelly roll, which was filled with nonaqueous electrolyte (BASF, 1.2 M/L $LiPF_6$ EC/EMC with 30:70 wt%). The design for a typical cylindrical cell was schematically illustrated in **Figure 3.1a** and the cell prepared for this work was shown in **Figure 3.1b**. The cell was cycled between 2.8 and 4.2 V vs Li+/Li using a VMP-300 potentiostat (Biologic) with constant current constant voltage (CCCV) charging protocol from low to high charging rates: 0.27 C, 1.6 C, 2.4 C, 3.2 C, and 4.4 C. The detailed charging/discharging curves were shown in Figure S5 and S6.

The operando NPD experiments were carried out at the SNS's NOMAD beamline, and the cell was charged/discharged at 20 °C. The NPD data was collected in operando mode (no relaxation period). Due to the relatively lower (neutron) flux at NOMAD (which is already one of the highest fluxed neutron diffractometers worldwide) compared to the synchrotron X-ray diffractometers, the required data collection time in this operando study is relatively longer than that using synchrotron X-ray diffraction (seconds or less). To achieve good signal-to-noise ratio of operando diffraction data that allows accurate structure refinements, a minimum of ~1 min data collection time is needed, thus the data collection time was set as 62 seconds for the operando experiments.

The extracted information on staging kinetics is spatial averaged, due to the relatively large neutron beam size (~ 1×1 cm^2) and strong penetration of neutron beam. Therefore, information on spatial distribution of various GIC phases are lost. In addition, the spatial and temporal distributions of Li^+ within electrodes keep evolving during the data collection, and the Bragg peaks (intensity and peak position) from each phase keep changing due to evolving Li^+ contents within each phase. Therefore, the collected diffraction data is a superposition of these time evolving peaks from phases with different SOC, which is a time average result.

During the operando experiments, time-of-flight (*TOF*) are converted to *d*-spacing using the conventional second order polynomial $TOF = ZERO + DIFC \times d + DIFA \times d^2$, where *ZERO* is a constant, *DIFC* is the diffractometer constant and *DIFA* is an empirical term to correct for sample displacements and absorption induced peak shifts. *ZERO* and *DIFC* were determined from the refinement of a standard NIST Si-640e data set and held fixed. The same *DIFA* value was adopted for all sequential refinements since the cylindrical cell was not moved during the entire experiment. For the low-resolution frames (bank 2 and 3), a back to back exponential function convoluted with a symmetrical Gaussian function was used to describe the peak profile. For the high-resolution

frames (bank 4 and 5), the moderator induced line profile was modeled using a modified Ikeda-Carpenter-David function [164–166]. Lorenz polarization is corrected by multiplying $d^4Sin\theta$ [165]. Absorption correction was carried out using the empirical Lobanov formula [165,167]. TOPAS Academic V6 suite was utilized to perform the sequential Rietveld refinements on all diffraction patterns obtained during the charging/discharging process [168,169]. The weightings of Cu and Al were fixed to values refined from the initial patterns (before charging). The cation mixing extent and atomic displacements for the cathode were fixed during the sequential refinement. The Li content within NMC622 was fixed to the value from the electrochemical data. The lattice parameters of pristine NMC622 and Li-intercalated graphite are thus obtained from refinement using ex-situ diffraction data of pristine powders. The refinement result of one operando diffraction pattern is shown in **Figure 3.1c**.

The structural evolution of graphite anode and NMC622 cathode are first studied at relatively slow charging rate to demonstrate the feasibility and reliability of this cylindrical cell design. The contour plots of the operando diffraction data alongside the voltage profile of the cylindrical cell under 0.27 C charging and 1 C discharging are shown in **Figure 3.2**. The peak shifting, intensity variation, and appearance/disappearance of certain Bragg peaks clearly suggest the continuous structural changes of both NMC622 and GICs during lithium intercalation/de-intercalation. As shown in the enlarged contour plot (**Figure 3.3)**, the intercalation of Li^+ into graphite undergoes a sequential staging process: from the initial solid solution process (pristine graphite) to stage III (LiC_{30}), dilute stage II (LiC_{18}), stage II (LiC_{12}) and the final stage I (LiC_6), agreeing with previous studies [35,170]. This sequential staging process is mainly a response to reducing the elastic and electrostatic interactions of inserted Li ions between graphene layers [171]. Detailed phase transition process during Li intercalation (charging process) are summarized in Figure S7. Upon initial intercalation of Li^+, no new Bragg peaks are detected and the graphite (114) reflection (S.G. $P6_3/mmc$) keeps shifting to larger *d*-spacing, indicating the initial Li^+ intercalation follows a solid solution reaction. When ~ 0.15 Li^+ ($Li_{0.15}C_6$) are intercalated, the stage III of GICs (LiC_{30} with A(Li)ABA… stacking, S.G. *P*3) phase starts to emerge, as indicated by the appearance of a broad peak at ~ 1.49 Å (**Figure 3.3**, which corresponds to the 007 reflection). Further intercalation of Li^+ leads to the formation of the dilute stage II phase (LiC_{18} with AB(Li)BA⋯ stacking, S.G. $P6_3mc$) and then the stage II phase (LiC_{12} with AA(Li)AA⋯ stacking, S.G. *P*6/*mmm*). The difference between LiC_{18} and LiC_{12} is the detailed stacking sequences of neighboring graphene layers

between adjacent Li layers: the former follows the AB type registration while the latter follows the AA type stacking [172,173]. The rapid increase of the (002) reflections of LiC_{12} (~1.02 Å) indicates that all LiC_{18} from dilute stage II have eventually been transformed into stage II (LiC_{12}). With more Li^+ intercalation, the stage II (LiC_{12}) starts to gradually transform into the fully lithiated stage I (LiC_6) with a new set of (002) reflections (S.G. *P*6/*mmm*) at larger *d*-spacing of ~ 1.04 Å. A small amount of LiC_{12} still coexists with LiC_6 at the end of charging mainly due to the use of extra amounts of graphite (e.g., the N/P ratio of 1.1). During discharge, the phase transition is largely reversible (**Figures 3.2** and **3.3**).

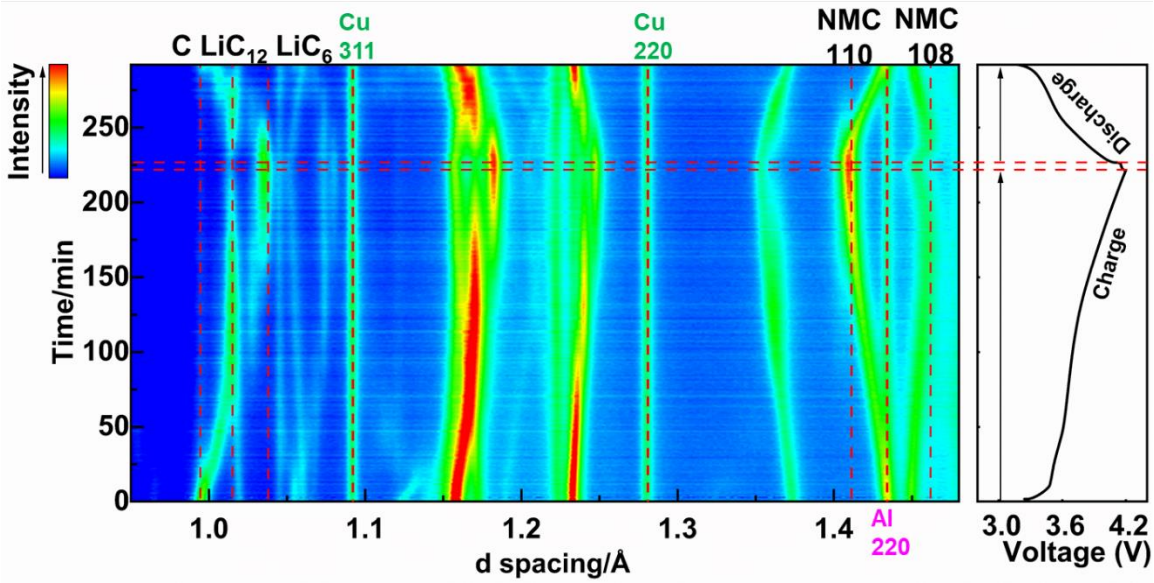

Figure 3.2. The structure/phase evolution of graphite and NMC622 under 0.27 C charge and 1 C discharge

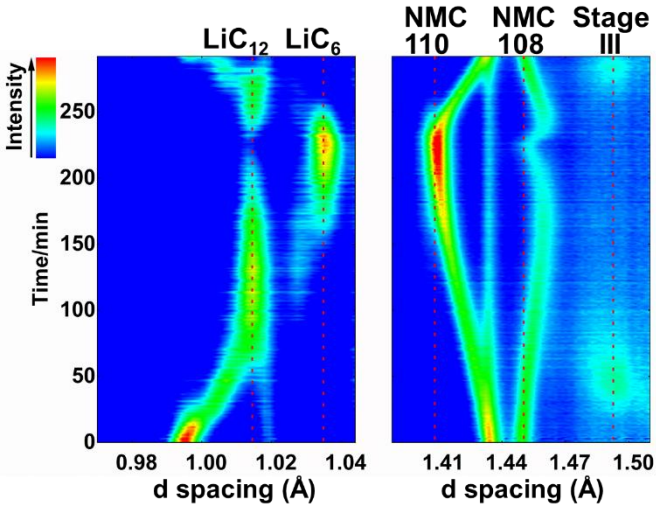

Figure 3.3. The formation of stage III (LiC_{30}), stage II (LiC_{12}), and stage I (LiC_6) under 0.27 C charge and 1C discharge.

For the cathode side, the de-intercalation of Li^+ from NMC622 leads to the oxidation of Ni^{2+}/Ni^{3+}, which compensates the charge loss caused by Li^+ removal [174–176]. The oxidation of transition metal (TM) cations decreases their ionic radii and increases the covalency between TM cations (e.g., Ni and Co) and ligand oxygen anion, leading to the decrease of average TM–O bond lengths and the subsequent decrease of lattice parameter *a* (from ~ 2.865 Å to ~ 2.817 Å, **Figure 3.4**). This is clearly indicated by the shift of the 110 reflection toward lower *d*-spacing (**Figure 3.3**), which changes from the initial ~ 1.43 Å to ~ 1.41 Å. Lattice parameter *c* first increases to its maximum value of ~ 14.52 Å (at x = ~ 0.5 in $Li_{1-x}Ni_{0.6}Mn_{0.2}Co_{0.2}O_2$), and then decreases to ~ 14.45 Å (x = ~ 0.622) at the end of charging (**Figure 3.4**). This trend is consistent with the observation of the shift of 108 reflection (**Figure 3.3)**, which first increases from ~ 1.44 Å to ~ 1.45 Å and then decreases to ~ 1.44 Å. The de-intercalation of Li^+, on one hand, effectively reduces the screening effect between adjacent oxygen planes, leading to the increase of electrostatic repulsion between oxygen planes (across the LiO_2 slab) and thus causes the increase of lattice *c*. On the other hand, the increase of the TM–O bond covalency results in the charge redistribution between TM cation and oxygen anion, leading to the partial charge depletion of ligand oxygen anion. This effectively reduces the electrostatic repulsion between oxygen anions across the inter-layer plane and leads to the decrease of lattice *c*. The change of lattice *c* is determined by the relative strengths of these two effects [157,177]. The changes in lattice parameters *a* and *c* are in

good agreement with previous studies on NMC cathode materials [178–180]. During cell discharging, the lattice parameters *a* and *c* follow the opposite trend of the charging process (**Figure 3.4**), consistent with the peak shifting in **Figure 3.3**. Due to the irreversible loss of Li ions from the formation of SEI and kinetic hindrance, lattice parameters *a* and *c* do not fully recover to their initial values [181,182].

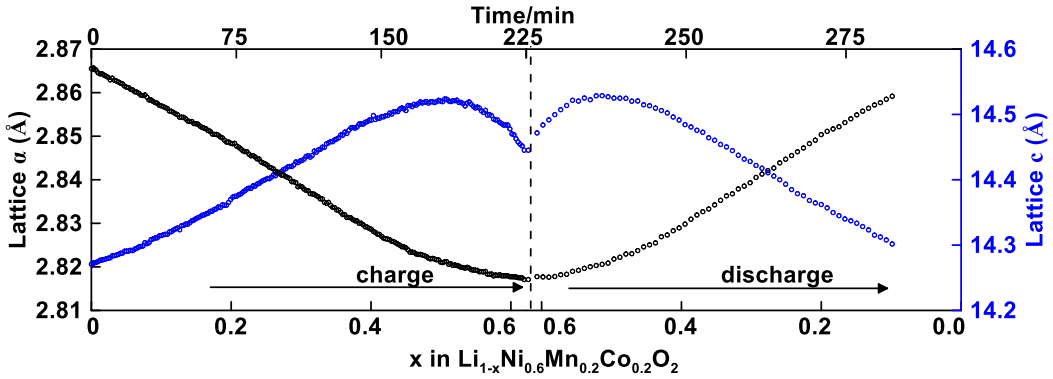

Figure 3.4. The lattice parameters a and c evolution of NMC622 under the 0.27 C charging and 1 C discharging.

Quantitative analysis was then carried out to better understand the structural evolution of NMC622 cathode and graphite anode at higher charging rates. **Figure 3.5** shows the variation of lattice parameters of NMC622 under different charging rates up to 4.4 C, which has similar trend compared to **Figure 3.4**. This indicates the crystal structure of NMC622 is well maintained during fast charging, which is consistent with previous reports on the capability of NMC to be intercalated/de-intercalated up to 10 C [183–185]. Small differences can be seen in lattice parameters under different charging rates, which is attributed to the averaging effect of powder diffraction analysis and larger Li concentration gradient within NMC622 under higher charging rate. During the charging process, Li ions de-intercalate from the surface layer of NMC622 particles first and a Li ion concentration gradient builds up from the surface to the core of the particle. Higher charging rate leads to greater concentration gradient, and the diffraction analysis is based upon the averaged data collected in 62 seconds and thus shows small variations [186–188].

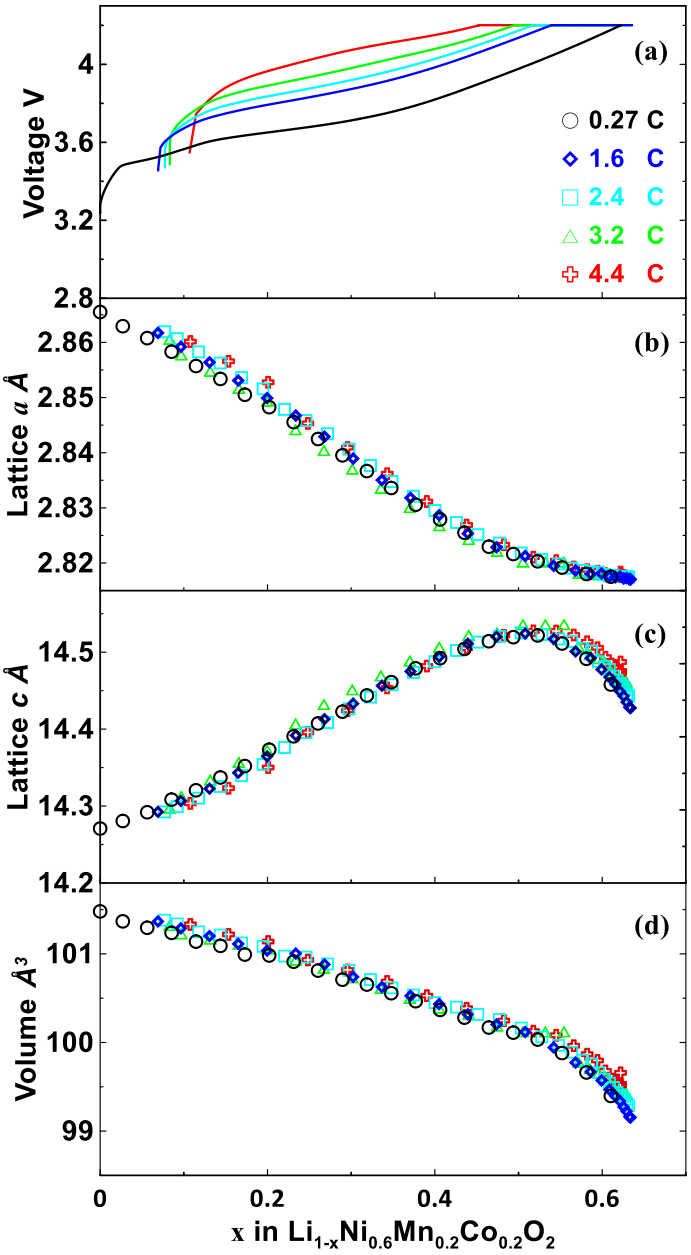

Figure 3.5. Lattice parameter evolution for NMC622 under different charging rates: (a) The evolution of charging voltage during charging; (b) The lattice parameter a; (c) The lattice parameter c; (d) The volume shrinkage during charging process.

For the anode side, the full diffraction patterns for the charging rates from 0.27 C to 4.4 C together with voltage profiles are shown in Figure S8, and corresponding contour plots for the whole charging/discharging processes are shown in Figure S9. The enlarged regions in **Figure 3.6** (0.98 Å to 1.06 Å and 1.40 Å to 1.52 Å) are utilized to elaborate the detailed phase transition of graphite under these rates (1.6 C ~ 4.4 C). The Li intercalation follows the same sequential staging

as revealed in **Figure 3.3** (slow charging at 0.27 C): from the emerging of (007) peak of LiC_{30} (stage III) at ~1.49 Å, to the (002) peak of LiC_{12} (stage II), and finally to the (002) peak of LiC_6 (stage I) at ~1.04 Å [147,189].

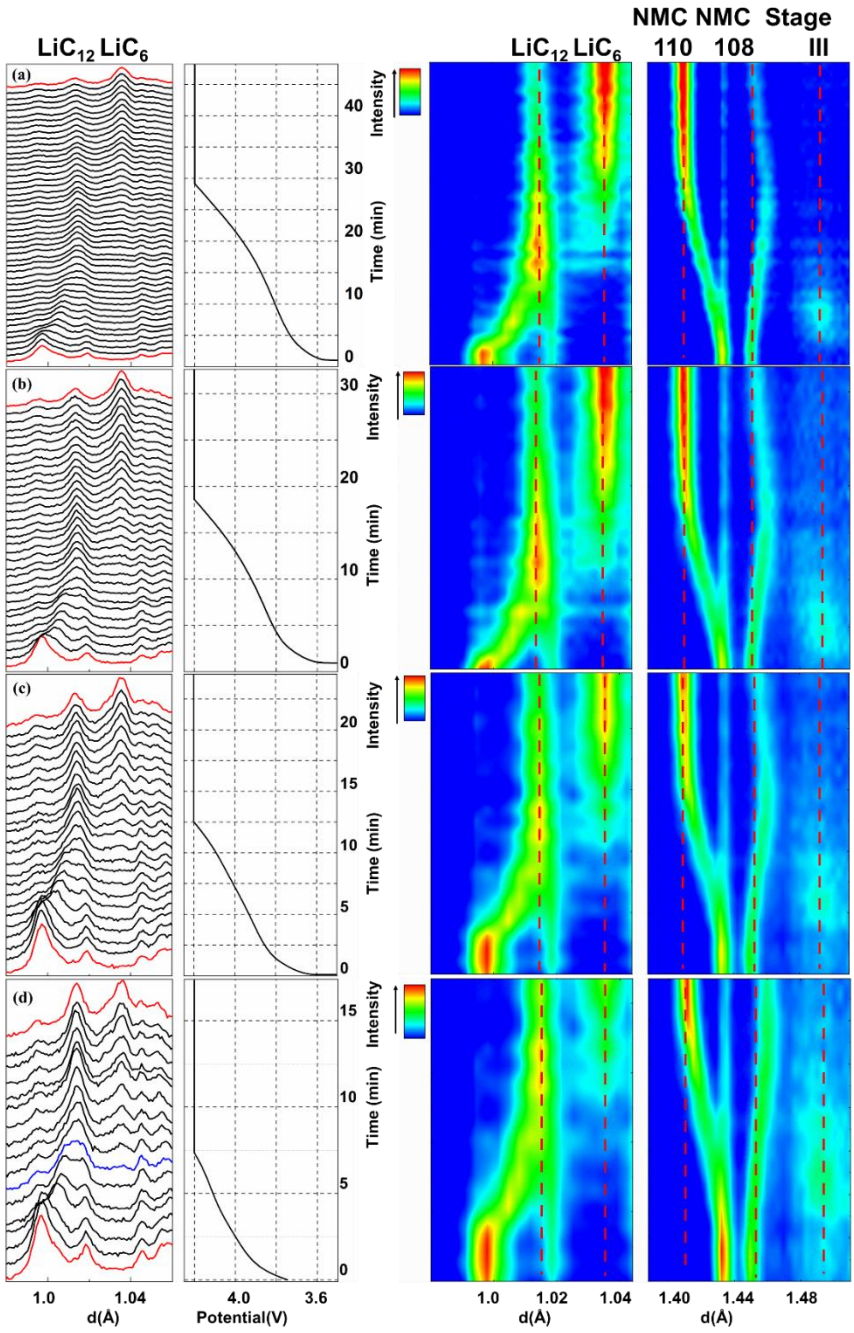

Figure 3.6. The phase evolution of graphite anode during the charging process under different charging rates: (a) 1.6 C; (b) 2.4 C; (c) 3.2 C; (d) 4.4 C.

For the 1.6 C and 2.4 C charging shown in **Figure 3.6**, LiC_{12} peak intensity increases to its maximum, and then starts to decrease with the increase of peak intensity of LiC_6. When the charging rate is increased to 3.2 C and 4.4 C, however, the peak of LiC_6 emerges and increases in intensity before LiC_{12} peak increases into its maximum intensity. Therefore, a simultaneous intensity increase of both LiC_{12} and LiC_6 reflections (for example, the 7^{th} diffraction pattern of 4.4 C) exists under higher charging rate. Numerical simulations by Dees et al. via electrochemical models presented the evolution of phase fraction in graphite anode at C/5, 1 C, and 4 C charging rates, and revealed that the monotonical increase of volume fraction for both LiC_{12} and LiC_6 phases only existed under 4 C charging, similar to our observation [190]. Quantitative analysis by Koffi P. C. Yao et al. via operando energy dispersive X-ray diffraction showed more detailed evolution of simultaneous increase of both LiC_{12} and LiC_6 under 1 C charging rate (with a 114 μm thick graphite anode). This phenomenon may be related to the inhomogeneous distribution of Li ions in the graphite electrode [149]. Figure S10 shows the SOC of the cell when LiC_6 phase emerges in the diffraction patterns (the uncertainty is from the capacity increment during neutron data collection period, 62 seconds in this case). A clear distinction can be noticed between 2.4 C and 3.2 C, where LiC_6 shows up at a relatively lower SOC under 3.2 C. This phenomenon is supported by other reports on high rate charging of Li-ion cells. Subsequently, LiC_6 starts to evolve from LiC_{12} in graphite electrode near separator while LiC_{12} forms at the expense of LiC_{18} (dilute stage II) in graphite electrode near current collector.

From the qualitative discussion above, it is shown that the LiC_{12}/LiC_6 two-phase reaction is slower than the solid solution reaction from C to LiC_{12}. It is therefore important to obtain the kinetics of the two-phase reaction between LiC_{12} and LiC_6. The relative weight ratio of LiC_6 and LiC_{12} can be obtained quantitatively by integrating the area of their respective diffraction peaks shown in Figure S11. **Figure 3.7** summarizes the time evolution of weight ratios (obtained from Rietveld refinement) of LiC_6 and LiC_{12} at 4 different charging rates (the ratios of LiC_6 and LiC_{12} under 0.27 C is included in Figure S12). Under a given charging rate, the weight ratio of LiC_6 keeps increasing while the weight ratio of LiC_{12} continues decreasing, which corresponds to the formation of LiC_6 at the consumption of LiC_{12}. The Johnson-Mehl-Avrami-Kolmogorov (JMAK) model, expressed in eqn (3.1), is then utilized to obtain more insight on the phase transition mechanism from LiC_{12} to LiC_6. The validity of JMAK model has been well proven in previous studies to probe the dynamics of phase transition in the solid reactions of electrode materials like

$LiFePO_4$ and graphite [191–193]. The Avrami exponents *n* of the JMAK model are extracted from the Sharp-Hancock plots and shown in **Figure 3.8**.

$$\left[-[\ln(1-a)]\right]^{1/n} = \mathrm{kt} \tag{3.1}$$

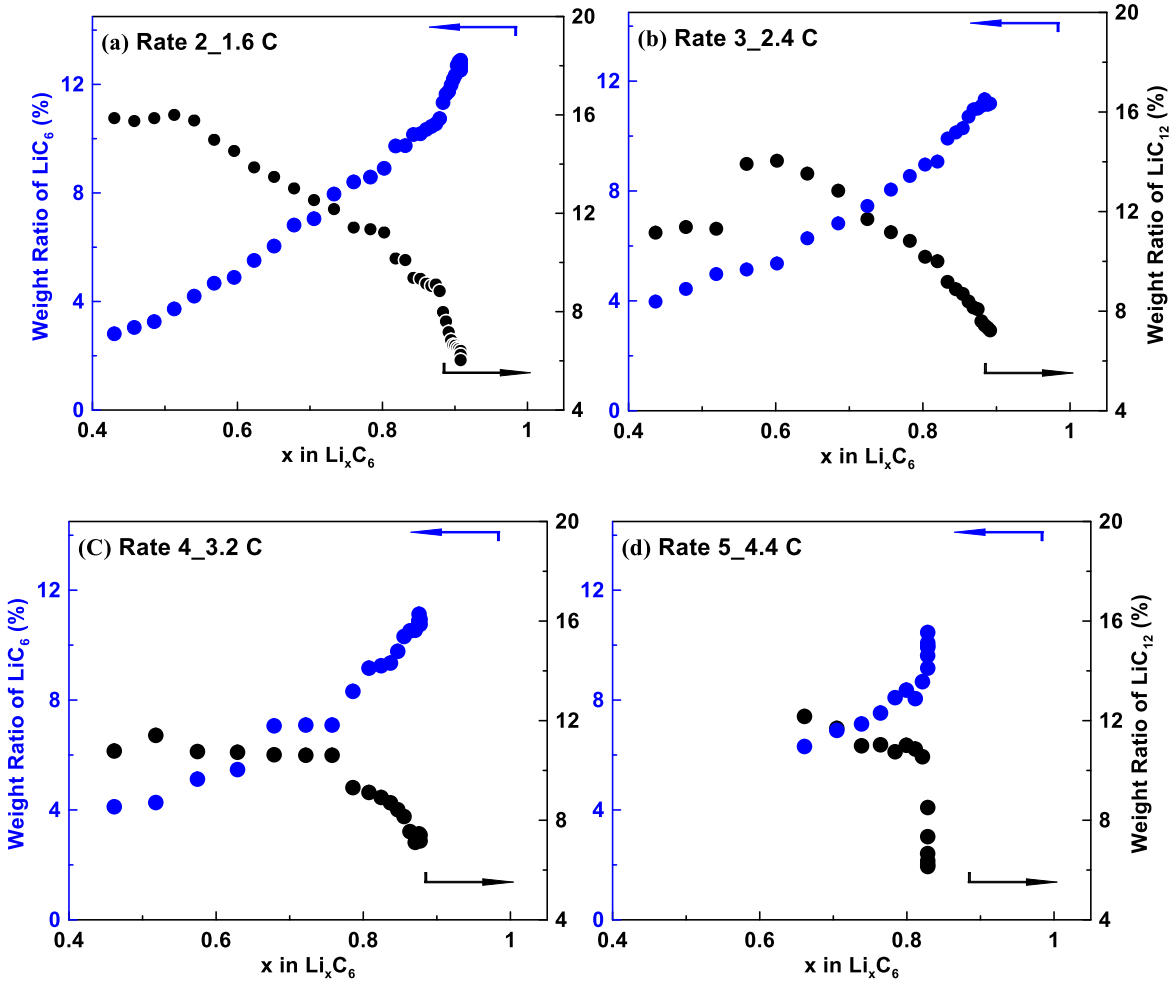

Figure 3.7. The time evolution of LiC12 and LiC6 for the whole charging process under the charging rate of (a) 1.6 C, (b) 2.4 C, (c) 3.2 C, (d) 4.4 C.

For the JMAK model, the nucleation-growth mechanism is utilized to describe the $LiC_{12} \rightarrow LiC_6$ transition, and it is debatable about its validity in describing this transition under high charging rates based on its inability to accurately capture the phase separation under nonequilibrium conditions. Combining direct optical images of a single crystal graphite anode under lithiation, Guo et al. utilized the Car-Hilliard reaction model to probe the lithiation of single crystal graphite [127]. Simulation results from this model well captured major lithiated phases

(stage I, stage II and stage III) which were supported by the experimental results from direct optical images. Furthermore, a multilayer free energy phase field model was developed by Smith et al. to describe the intercalation kinetics for these layer structure chemicals, especially the phase separation within them [194]. However, to further confirm the proposed models (JMAK or Car-Hilliard) from atomistic structure changes, operando pair distribution function (PDF) experiments (which not only probes the average phase transition but also the local/short-range structure changes) on the $LiC_{12} \rightarrow LiC_6$ transition of graphite anode are needed. This will be investigated in our future work to further verify the validity of JMAK model under higher charging rates.

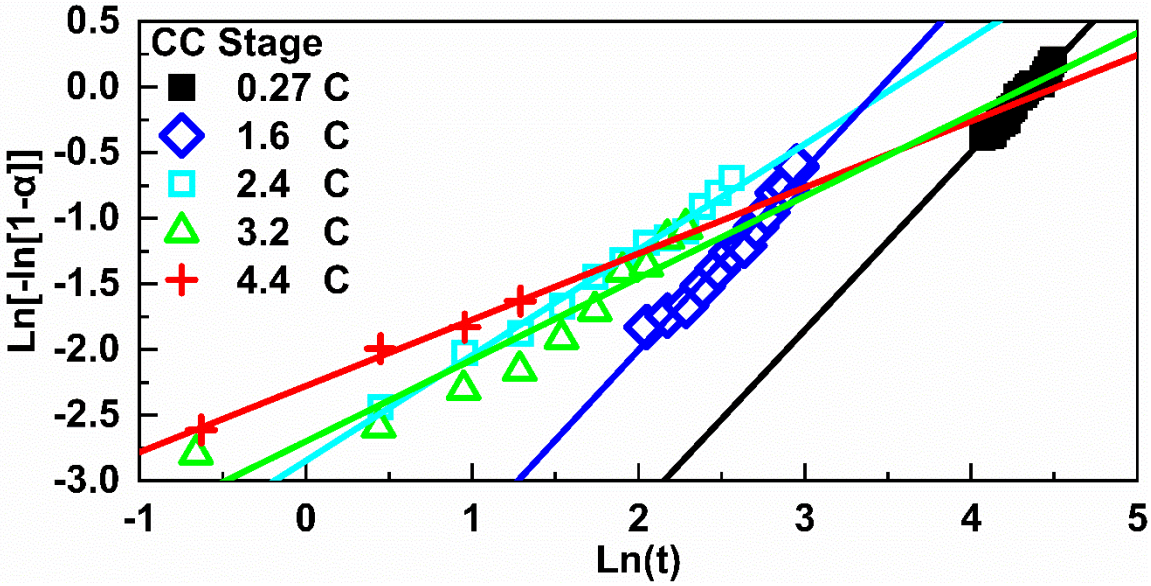

Figure 3.8. The Sharp-Hancock plot for LiC6 under 5 charging rates for the CC stage

$$n = a + bc \tag{3.2}$$

In equation (3.2), the Avrami exponent n is divided into three components: the nucleation rate a, growth dimensionality b and growth parameters c [195–197]. Parameter a reveals the detailed nucleation rate: $a = 0$ corresponds for a nucleation rate of zero , $a = 1$ for the constant nucleation, $a > 1$ for an increasing nucleation rate while $0 < a < 1$ for an decreasing nucleation rate [191]. Parameter b represents the growth dimensionality and its value varies from 1, to 2, and to 3, corresponding to 1D, 2D and 3D growth mechanisms, respectively. Parameter c represents the specific growth mode: 0.5 for the diffusion-controlled growth and 1 for phase boundary (interface)

controlled growth. The Avrami exponent *n* decreases with the increase of charging rates from ~1.3 at 0.27 C to ~ 0.5 at 4.4 C. Given the fitted values of *n* and available values of parameters *a*, *b*, and *c* in JMAK model, we propose $b = 1$ and $c = 0.5$ for the $LiC_{12} \rightarrow LiC_6$ transition, with *a* ranging from 0 to 1. These kinetic parameters are summarized in **Table 3.1**. Particularly, the nucleation index *a* keeps decreasing from ~ 0.8 at 0.27 C to almost 0 at 4.4 C, indicating nucleation rate decreases under increasing charging rates. Thus, with $b = 1$ indicating 1D growth and $c = 0.5$ of diffusion-controlled growth, the result suggests that the $LiC_{12} \rightarrow LiC_6$ transition is kinetically controlled by diffusion, 1D growth process with decreasing nucleation rate under increasing charging rates.

Table 3.1. Kinetic parameters for the formation of LiC_6 derived from NPD data under CC stage

Type	exponent n	*a*	R^2
0.27 C	1.356(40)	0.856(40)	0.974
1.6 C	1.373(62)	0.873(62)	0.979
2.4 C	0.804(27)	0.304(27)	0.988
3.2 C	0.622(77)	0.122(77)	0.889
4.4 C	0.504(77)	0.004(77)	0.991

$$Li^+ + LiC_{12} + e^- \rightarrow 2LiC_6 \qquad (3.3)$$

As shown in eqn (3.3), the $LiC_{12} \rightarrow LiC_6$ transition involves the following factors: (1) Li^+ diffusing from liquid electrolyte to the edges of graphite flakes; (2) Li^+ passing through the SEI layer; and (3) Li^+ intercalation/diffusion within bulk graphite and corresponding charge compensation. For Li^+ passing through the SEI layer, the studies by Dees et al. show that the interfacial impedance remains almost constant and there is no rate effects on this diffusion process up to 10 C [198,199]. In addition, graphite possesses good electronic conductivity in the order of 1.0×10^0 to 2.45×10^5 S/cm, much higher than Li^+ ionic conductivity within graphite [200,201]. Lithiated graphite also exhibits higher electrical conductivity at higher degree of Li^+ intercalation. Therefore, the influence of electronic conductivity on the formation of LiC_6 is negligible. It is seen that the Li^+ diffusion within lithiated graphite and liquid electrolyte are both involved for this transition. For Li^+ diffusion within graphite/GICs, most experimental studies indicate a range from 10^{-10} to 10^{-12} cm^2/s at room temperature, due to various methods used and the difference (graphite

type and microstructure) of graphite tested [202–210]. The typical value for Li^+ diffusion coefficient of liquid electrolyte is $D = 4 \times 10^{-6}$ cm^2/s, much higher than the Li^+ diffusion within graphite [211,212]. Moreover, both experiments and simulations suggest a decreasing Li^+ diffusion with more Li^+ intercalated, especially for the $LiC_{12} \rightarrow LiC_6$ transition (with $0.5 < x < 1$ for Li_xC_6), due to the larger energy barrier for the diffusion with dense Li ions between graphene layers [35]. Thus, the relatively sluggish Li^+ diffusion in the bulk graphite particles is the controlling factor for the $LiC_{12} \rightarrow LiC_6$ phase transition.

Besides this sluggish diffusivity of Li^+, the highest Gibbs free energy barrier for $LiC_{12} \rightarrow LiC_6$ phase transition is another possible reason for the relatively slower $LiC_{12} \rightarrow LiC_6$ phase transition kinetics and the delay in phase transition under higher charging rates. This has been reported by others. Smith et al. verified this highest energy barrier for $LiC_{12} \rightarrow LiC_6$ transition via the multi-layer phase field model with the Cahn-Hilliard reaction mechanism [194]. In line with this theoretical result, Donal P. Finegan et al. found the switch of lithiation along depth profile under 2 C charging: initially, lithiation occurred dominatingly in the frontal region, then it shifted to deeper regions, and finally went back to the frontal region [150]. This phenomenon indicates the high energy barrier for this $LiC_{12} \rightarrow LiC_6$ transition. The overpotential at the frontal region was initially less than that needed to overcome this barrier, thus lithiation occurred in deeper regions. Once this overpotential for the phase transition was satisfied, lithiation went back to the frontal regions. This is consistent with our current observations.

For nucleation rate parameter *a*, it is close to 1 at charging rates of 0.27 C and 1.6 C. This indicates that the nucleation rate for new LiC_6 phase is almost constant when the charging rate is low and/or moderate, suggesting a smooth transition from LiC_{12} to LiC_6. With the increase of charging rate to 2.4 C, parameter *a* decreases significantly to 0.304, which is due to insufficient Li ions available for the nucleation of new LiC_6 phase. The reason can be easily explained by the large concentration gradient needed for the high charge rate (large current) [213]. With further increase of the charge rate (current), parameter *a* decreases greatly and reaches near 0 at 4.4 C, which indicates the nucleation of new LiC_6 phase region is largely limited for fast charging.

In our study, Parameter *b* from the JMAK model suggests a one-dimensional growth of nucleated LiC_6, we attribute this 1D growth to the aggregation of LiC_6 along the *c* direction of

graphite flakes, as schematically shown in **Figure 3.9**. As revealed by the Daumas-Herold domain model and following theoretic studies, the well-formed LiC_{12} phase follows the AA(Li)AA⋯ stacking, and the space between every two neighboring graphene layers are available for further intercalation of Li^+ to form denser LiC_6 phase, as a response to reducing energy for the whole system [214]. Both simulation and experiments indicate that it is impossible for intercalated Li^+ to penetrate graphene layers along the *c* direction, given the large energy barrier of ~ 10 eV, and intercalated Li^+ only diffuses within *ab* plane of graphene layers [214]. Considering the nonuniform morphology of graphite edges and the randomness of Li intercalation, Li^+ intercalates into some graphene sheets earlier than other sheets. Meanwhile, intercalated Li^+ exhibits intralayer attraction and interlayer repulsion, and the interlayer long-ranged electrostatic repulsion is screened out only over certain layers of graphene along the *c* direction [171,215–219]. Thus, graphene layers intercalated by Li^+ would hinder the intercalations of adjacent graphene sheets. Combined with the randomness of Li^+ intercalation and the nonuniform morphology of graphite flakes, parallel Li^+ intercalations between empty graphene layers simultaneously are hindered. Thus, we propose some graphene layers are fully intercalated earlier than other layers, with adjacent layers less lithiated or even without any Li^+ intercalated, exhibiting a layer by layer intercalation behavior, to some extent. Following Li^+ will repeat this serial intercalation process until the full formation of LiC_6. Thus, the transition of LiC_{12} to LiC_6 exhibits a 1D growth mechanism. A similar 1D growth behavior was also observed by Evans et al. during the intercalation of Li^+ into layered TiS_2 [220]. And similar "selective" deintercalation of H_2SO_4 from certain graphene layers was also observed for the opposite transition from stage I GIC to stage II GIC transition [221]. Taken together, the monotonic decrease of *n* from the JMAK model with increased charging rates suggests one dimensional growth, diffusion-controlled with decreasing nucleation rates for the transition of LiC_6 from LiC_{12}.

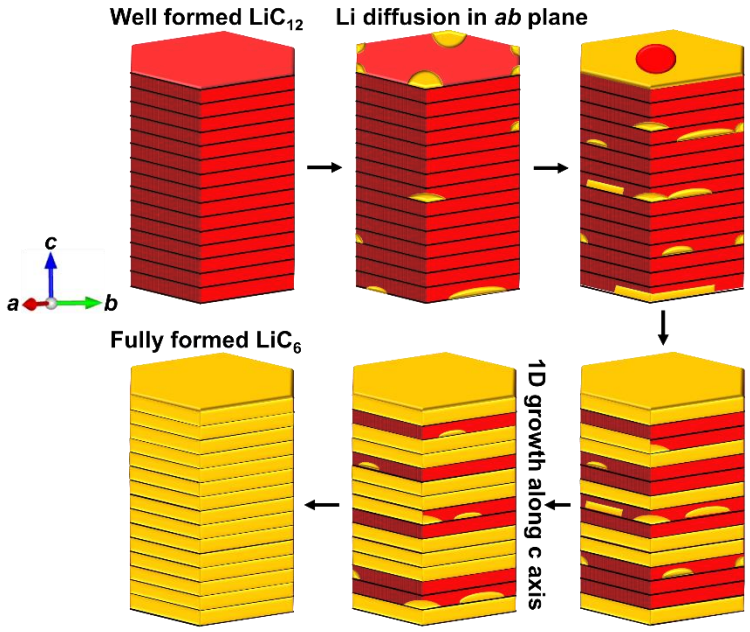

Figure 3.9. The 1D growth for the LiC_6 along *c* direction of graphite flake.

3.3 Conclusions

In this study, the fast operando neutron powder diffraction experiment is implemented via customized cylindrical cell. The good signal-to-noise ratio of collected operando data enables the multi-phase Rietveld refinement and quantitative structural analysis of both NMC622 cathode and graphite anode. It is found that the structural evolution of NMC622 during the Li deintercalation process is consistently determined by its lithium contents up to 4.4 C charging rate, suggesting that NMC622 cathode is unlikely the limiting factor for fast charging of NMC/graphite cell. Instead, we found that the stage II (LiC_{12}) → stage I (LiC_6) transition during lithiation of graphite is the rate limiting step when charging the full cell to above 3 C. This is further confirmed by quantitatively study of the evolution of LiC_{12} and LiC_6 using the Johnson-Mehl-Avrami-Kolmogorov (JMAK) model, where the Avrami exponent *n* decreases from ~ 1.3 to ~ 0.5 as the charging rate increases from 0.27 C to 4.4 C. This indicates that the stage II (LiC_{12}) → stage I (LiC_6) transition is a one-dimensional diffusion controlled growth with decreasing nucleation kinetics under increasing charging rates. In all, this study sheds light on the comprehensive understanding and further optimization of rate performance of LIBs using graphite anode.

4. EFFCTS OF SOLVENT FORMULTIONS IN ELECTROLYTES ON FAST CHARGING OF LI-ION CELLS

This chapter is from the following publication: **Wu, Xianyang**, et al. "Effects of solvent formulations in electrolytes on fast charging of Li-ion cells." *Electrochimica Acta* 353 (**2020**): 136453.

Contributions

Xianyang Wu: Design and implementation of experiment, data processing, writing, reviewing, and editing of original draft.

Tianyi Liu: Implementation of experiment, reviewing, and editing of original draft.

Yaocai Bai: Implementation of ICP-OES experiment, data analysis, editing of original draft.

Xu Feng: Implementation of XPS experiment, data analysis, reviewing of original draft.

Muhammad Mominur Rahman: Implementation of XAS experiment, reviewing of original draft.

Chengjun Sun: Implementation of XRD experiment, reviewing of original draft.

Feng Lin: Implementation of XAS experiment, reviewing of original draft.

Kejie Zhao: Conception and design of experiment, reviewing, and editing of original draft.

Zhijia Du: Conception and design of experiment, reviewing, and editing of original draft.

4.1 Introduction

Lithium ion battery (LIB) plays an indispensable role in portable electronics since its commercialization in the 1990s [222]. Due to its high energy density, high power density, high Coulombic efficiency and long cycle life, it is becoming the dominating power source for electric vehicles (EVs) [223]. The high demand from automobile industry for LIBs with higher energy density and better rate performances have stimulated intensive research on LIBs [224,225]. It is well recognized that the long charging time of electrical vehicles (EVs) and range anxiety is plaguing the wide application and full electrification of EVs. To overcome these challenges and amp up the EVs market, the US. Department of Energy (DOE) sets the goal to decrease charge time of high energy density Li-ion cells to 15 minutes or less [226,227]. The gaps between the state-of-the-art LIBs technology and fast charging has been systematically reviewed [10,14,228–230].

The most pronounced issue in fast charging is lithium plating [70,231]. Graphite is the extensively used anode materials due to its high specific/volumetric capacity, good rate capability, high Columbic efficiency and good cycle life [232]. However, the potential of reversible lithium intercalation/de-intercalation (into LiC_6) is around 80 mV, which is close to the metallic lithium plating/stripping potential. For fast charging with substantial polarization in the cell, Li plating is thermodynamically attainable when anode potential falls below 0 V (vs. Li^+/Li). Li plating is broadly known to cause deteriorate capacity fading and potential safety concerns [70,231].

In state-of-the-art high energy density of LIBs, a moderately thick electrode with high areal loading (3-4 mAh/cm^2) has been widely used [77]. In the thick electrode, the high tortuosity increases the cell resistance dramatically and leads to high risk of lithium plating [29,77,233]. Legrand et al has established an electrochemical modeling to predict the Li plating during the charging of a Li-ion cells [234]. The increased cell resistance also cause the cell to reach the cutoff voltage in a short time, reduce the effective charging time, and thus decrease the attainable energy [57]. Symmetric cells of graphite anode and layered $LiNi_{0.8}Mn_{0.1}Co_{0.1}O_2$ (NMC811) cathode were developed by Mao et al. and the graphite anode was identified as the limiting factor because the effective N/P ratio falls below 1.0 at high charging rates [233]. Moreover, Malifare et al. examined the graphite electrodes with different areal loading (2–6 mAh/cm^2) and porosity (0.1–0.45) to understand how Li plating occurred [235]. They found the electrolyte potential gradient from the Li+ concentration gradient leads to a large liquid phase overpotential across the cell in thick electrodes and thus leads to Li plating between the graphite electrode and the separator in a full cell.

To address the fast charging challenges in high energy density LIBs, the improvement of the mass-transport of the Li ions in the electrolyte phase is inevitable so that the enough Li ions are available for graphite intercalation and the anode potential is not suppressed below 0 V [57]. Colclasure et al. [236] showed that the transport property (ion conductivity and Li ion transference number) of electrolyte was the key factor to shorten the charging time for LIBs while maintaining high energy density via modeling results. This is consistent with Du et al that better fast charging performance of LIBs can be achieved using electrolyte with LiFSI as Li salts due to its higher ion conductivity and transference number over $LiPF_6$ [57]. Yang et al. proposed increasing cell temperature to an optimal value to improve fast charging with the trade-off between SEI growth and Li plating [237,238]. They believed the conduction and diffusion of Li ions in electrolyte are

enhanced to avoid Li plating. Improving the transport properties of non-aqueous electrolyte has also been identified by Liu et al. as one important direction to realize the fast charging technologies [230].

The utilization of various organic solvents as co-solvents, including esters and ethers, has been proved to be an effective way to lower the viscosity and thus enhance the Li ion conductivity of the electrolyte to further improve the overall performance of LIBs [239,240]. In this paper, various co-solvents, including MA, EA, EF, DMC are mixed with EC and EMC with $LiPF_6$ salt to study their effects on enhancing the fast charging performance in $LiNi_{0.6}Mn_{0.2}Co_{0.2}O_2$ (NMC622)/graphite Li-ion cells.

4.2 Experiments

The NMC622 and graphite electrodes are prepared at the DOE Battery Manufacturing R&D Facility (BMF) at Oak Ridge National Laboratory. The cathode consists of 94 wt% NMC622 (Targray), 3 wt% carbon black (Denka Li-100) and 3 wt% polyvinylidene fluoride (PVDF, Solvay 5130), with areal loading of 3.0 mAh/cm^2 and the calendared porosity is 30%. The graphite anode consists of 94 wt% graphite (Superior Graphite 1520T), 1 wt% carbon black (Timical C65) and 5 wt% polyvinylidene fluoride (PVDF, Kureha 9300). The areal loading was 3.5 mAh/cm^2 with a porosity of 30% after calendaring.

The electrolytes are made of 1.2 M $LiPF_6$ (Sigma-Aldrich, purity ≥ 99.99%) salts dissolved in a combination of EC, EMC and co-solvents (DMC, EMC, EA, EF and MA) with 30:50:20 wt% ratio. In the case of EMC, 1.2 M $LiPF_6$ in EC: EMC 3:7 by weight is widely recognized as Gen2 electrolyte. The pouch cells are assembled with the electrodes and separator (Celgard 2325) inside a dry room with a dew point of less than −50 °C and relative humidity (RH) of 0.1% at BMF. Then the cells are cycled between 2.8 and 4.2 V with constant voltage holding at 4.2 V (trickle charging) using a battery cycler, Maccor Series 4000, in an environmental chamber at 30 °C. The charging current was calculated from the nominal capacity (assuming 175 mAh/g of NMC622). A total time limit was imposed to guarantee that the duration of the charging step did not exceed the intended time for each C rate (15 minutes for 4C charging, 20 minutes for 3C, 30 minutes for 2C 1 hour for 1C charging). The long-term cycling performance was tested under fast charging at +4C/-1C for 200 cycles.

The conductivity of electrolytes was measured using a conductivity cell (Cole-Parmer). The conductivity cell constant was first calibrated with standard KCl solutions. Electrolyte conductivities were obtained from the electrochemical impedance spectroscopy (EIS) from 10 Hz to 1 MHz, with a 5-mV perturbation voltage using a potentiostat (Bio-Logic).

All the post-test analysis was conducted when the cells were fully discharged to 2.0 V and hold at 2.0 V for 10 hours. Pouch cells were opened in the Ar-filled glovebox and the cycled electrodes were rinsed with DMC for 3 times (2 minutes a time) to remove Li salts on the electrodes. The structures of the electrode materials were examined by X-ray diffraction (XRD) (PANalytical X'PERT operated at 45 kV and 40 mAh; Cu source, $\lambda = 1.54$ Å). XAS experiments on the Ni K-edge of pristine and cycled NMC622 electrodes were carried out in transmission mode at Beamline 20-BM-B of the APS.

The electrolyte in the pouch cell after long-term cycling was extracted and analyzed by ICP-OES following the same procedures reported by Thompson et al. [93]. The cycled pouch cells are cut open in the dry room and sealed in centrifuge tube, then they were centrifuged under 2200 rpm for 30 minutes. After dilution in ~2wt% HNO_3 solution, The Li concentrations were analyzed using Perkin Elmer Optima 2100DV ICP-OES.

X-ray photoelectron spectroscopy (XPS) characterization of the surface chemistry on negative and positive electrodes were conducted on a PHI VersaProbe III scanning XPS microscope, with monochromatic Al K-alpha X-ray source (1486.6 eV). The XPS spectra are acquired with 200 μm/50 W/15 kV X-ray settings and dual-beam charge neutralization. All binding energies were referenced to C-C peak at 284.8 eV. Atomic concentrations of these elements are determined from the integrated intensity of the elemental photoemission features corrected by relative atomic sensitivity factors. For the analysis of chemical states of elements, the PHI and NIST XPS Databases are used as reference. The atomic ratios of elements are determined from the integrated intensity of elemental photoemission features corrected by each element's relative atomic sensitivity factors using CasaXPS.

4.3 Results and discussions

Figure 4.1 shows ionic conductivities for all electrolytes with molarity ranging from 0.5 to 1.75 mol/L at 20, 30, and 40 °C. For convenience, the legends in the figures (here and after) are denoted by the co-solvent of the electrolyte in $LiPF_6$ dissolved in EC/EMC/Co-solvent 30/50/20

wt%. At a given temperature and solvent system, the ionic conductivity increases with the increase of salt concentration and reaches the maximum value at 1.0 M. Then the ionic conductivity decreases with further increasing salt concentration which can be attributed to the increasing viscosity and higher ion association [241–243]. The conductivity of a specific electrolyte composition is improved with increasing temperature, which is ascribed to the added thermal agitation into the system to increase the ion mobility [242]. This increased conductivity at elevated temperature can be beneficial to fast charging as the cell temperature is reported to increase during fast charging [244]. The utilization of these co-solvents shows the ionic conductivity changes with the electrolyte formulations with the trend of MA>EF>EA>DMC>EMC.

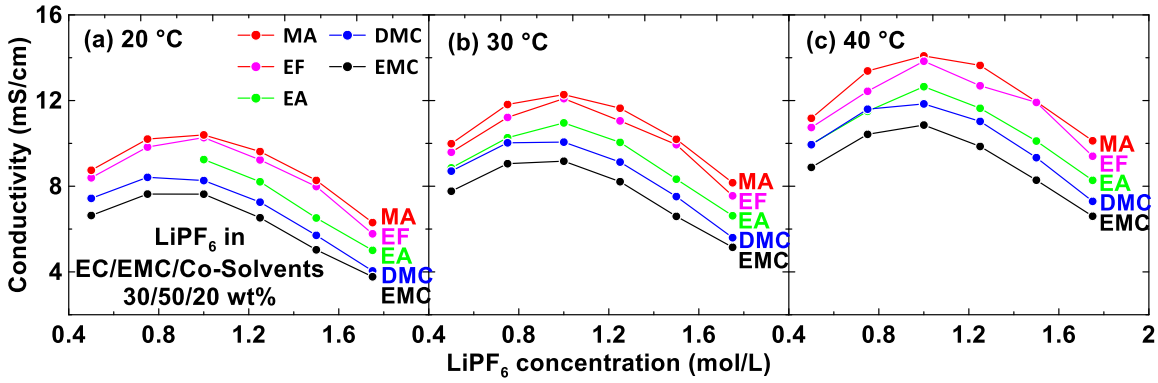

Figure 4.1. the ionic conductivities of 5 electrolytes under different temperatures: (a) 20 °C; (b) 30 °C; and (c) 40 °C

Pouch cells of NMC622/graphite filled with electrolyte of 1.2 M $LiPF_6$ in 5 different solvent systems show similar capacity at low charge/discharge rate (±C/3). The cells are then charged at different C rate at 2C (30-minute), 3C (20-minute) and 4C (15-minute), and their capacity retentions are summarized in **Figure 4.2**. With shorter charging time, the cell capacity retention drops gradually in all 5 cases, which largely due to the Li ions mass transport limitation in the electrolyte at higher C rate in high energy Li-ion cells [57]. However, the use of different solvents changes the capacity retention. For 15-minute fast charging, the capacity retentions with EF, MA, EA, DMC and EMC are 81.1%, 80.5%, 81.6%, 77.3% and 72.8%, respectively. The improvement can be ascribed to the increased ionic conductivity with co-solvents. Under higher charging C rate, the improved ion conductivity mitigates the polarization and prompts homogenous distribution of Li ions in mass transport [29,57].

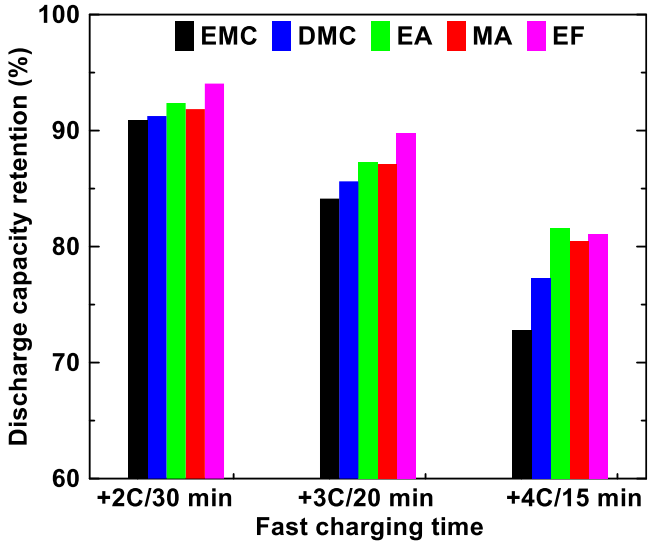

Figure 4.2. The cell discharge (under -1C rate) capacity retention under different charging rate/time using 5 different electrolytes compared to capacity under ±C/3.

Figure 4.3 shows the cycling performance of the pouch cells under fast charging conditions using different electrolyte formulations discussed above. The cells with EF electrolyte show the worst cycling performance with only ~40% of capacity retained after 160 cycles before the cells were stopped. The cells with MA and EA electrolytes show improved cycling performance compared to EF electrolyte, with 66.2% and 73.6% capacity retention after 200 fast charging cycles, respectively. The use of DMC in the electrolyte shows the best cycling performance among all electrolyte formulations with 88.7% capacity retention after 200 cycles. The Li plating on graphite electrodes after repeated fast charging cycles is also studied in **Figure 4.3**. All the electrodes show apparent Li plating on top of the graphite electrodes. However, the plating in electrolytes with EA, DMC and EMC is uniform and smooth surface, while it is non-uniform in electrolytes with EF and MA. The uniformity in Li plating is phenomenally related to the cycling performance to a certain extent.

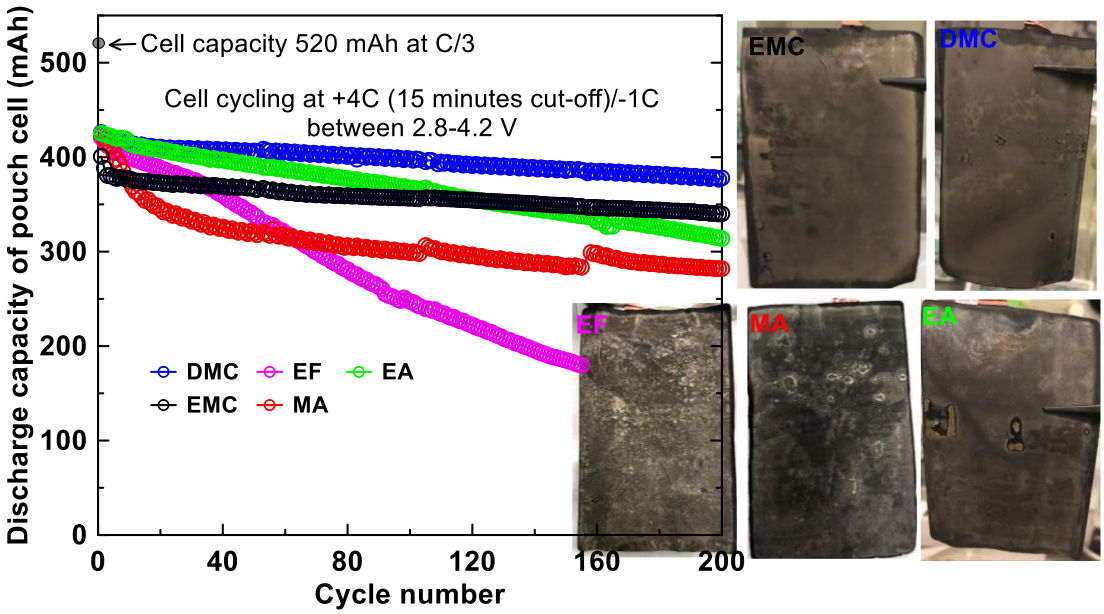

Figure 4.3. The long-term cycling performance of the pouch cell under fast charging conditions with different electrolytes of 1.2 M $LiPF_6$ in EC: EMC: Co-solvent 30:50:20 wt%. Li plating on graphite electrodes after 200 fast charging cycles.

To test the loss of active Li ion inventory in the NMC622 cathode, half Li coin cells were made using these cycled NMC622 electrodes with fresh Li foils and Gen2 electrolyte. **Figure 4.4** shows the 1st charging/discharging and 2nd charging voltage curves of these coin cells. During the first charging process, any remaining active Li ions are de-intercalated from the cathode structure. The discharging process determines how many Li ions can be intercalated back into the cathode structure. The loss of Li ion inventory (EF>MA>EA>EMC>DMC) in NMC622 agrees with the capacity of the pouch cells at the end of 200 fast charging cycles in **Figure 4.3**. Here, the loss of Li inventory from the NMC622 cathodes has two destinations: "dead" metallic Li plating and SEI growth (on both graphite and plated Li). Yang et al. reported the combination of computational modeling and experimental voltage relaxation to quantify the two factors [245,246]. Li plating in their report is induced by the ever-growing SEI which block ion mass transport and increase the cell resistance. Therefore, the Li inventory loss is mainly due to the SEI growth with contribution from lithium plating in late-stage of the long term cycling. In this fast charging study, limitation on the Li ion mass transport emerges at the very beginning of the fast charging cycles and leads to sever Li plating. Therefore, we speculate the Li inventory loss during fast charging cycles is mainly due to the Li plating. In **Figure 4.4**, all electrodes except the one from EF containing electrolyte

show similar discharging capacity, which indicates the layered NMC622 cathode structure is well maintained and capable for reversible intercalation/deintercalation. The EF electrode shows less capacity, which indicates the EF may have partly damaged the NMC622 structure.

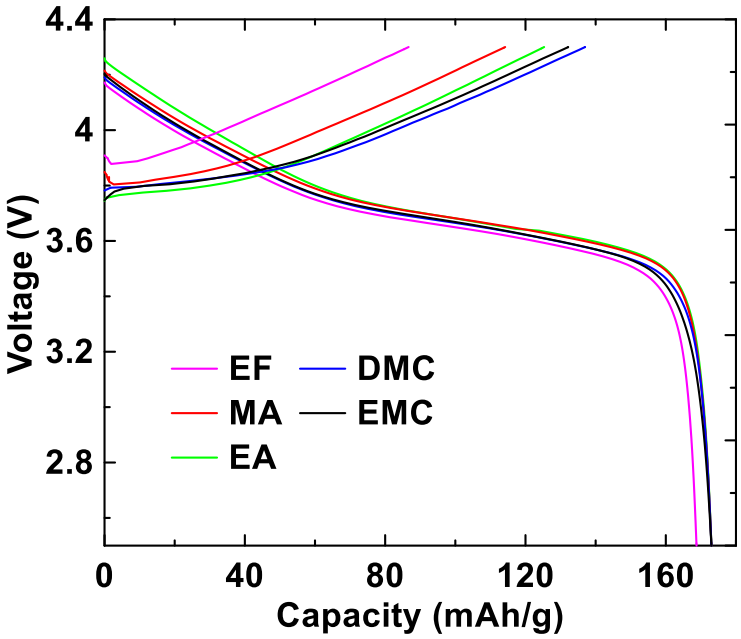

Figure 4.4. Voltage curves of Li cells assembled with NMC622 cathode after 200 cycles under +6C/-1C charge/discharge rates. The electrode was charged and discharged at a constant rate of C/10 between 2.5 and 4.2 V.

X-ray absorption near edge spectroscopy (XANES) and extended X-ray absorption fine structure (EXFAS) at Ni K edge were used to probe the change of oxidation state of Ni in the bulk NMC622 cathode, as most Mn and Co ions remain their oxidation state during the charging/discharging process. **Figure 4.5a** shows the normalized Ni K-edge XANES of the NMC622 electrodes after 200 fast charging cycles. Compared to the pristine NMC622 electrode, the absorption K edge of Ni from all the fast charging cycled NMC622 electrodes shifted from ~ 8347 eV to higher absorption energy, indicating the oxidation of Ni from Ni^{2+}/Ni^{3+} to higher Ni^{3+}/Ni^{4+} state for the charge compensation of active Li loss [247,248]. The shifting magnitude in energy is consistent with the loss of Li in the NMC622 electrodes (except for the one from EF) in **Figure 4.3** and **Figure 4.4**. **Figure 4. 5b** shows the Fourier transform radial distribution function for the Ni K-edge EXAFS and the fitting results are listed in **Table S1** to study the local environment of Ni ions [249]. Compared to the pristine NMC622 electrode, the average Ni-O bond

lengths for fast charging cycled electrodes decrease from initial value of ~ 2.0 Å to ~ 1.9 Å. The cycled NMC622 electrodes also show decrease in the Ni-TM average bond lengths, which indicates a higher oxidation state of Ni and expansion of the c lattice in the layered structure [248] . The decrease of the average bond lengths of both Ni-O and Ni-TM is due to the loss of active Li ions and decreasing Li screening effects on the negative oxygen charge in NMC622 structure as shown in **Figure 4. 4**.

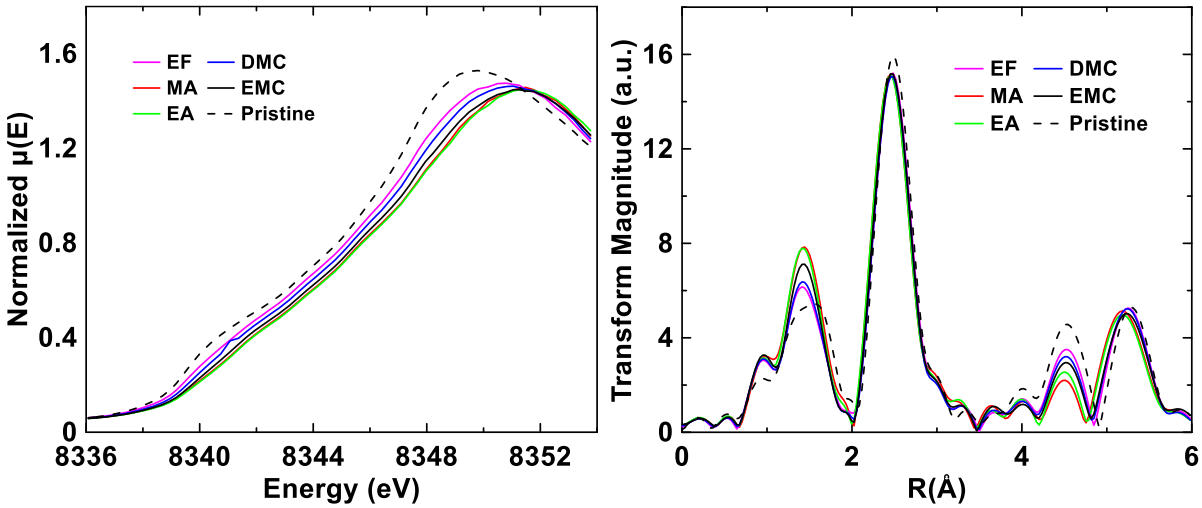

Figure 4.5. (a) XANES and (b) Fourier transform radial distribution function for the Ni K-edge EXAFS of the pristine and fast charging cycled NMC622 electrodes in different electrolytes.

Figure 4.6 shows the XRD patterns of the NMC622 electrodes with all major peaks indexed to the R$\bar{3}$m structure. It is clearly seen no new phase evolved in the cycled NMC622 samples, indicating the loss of active Li ion in the structure from the fast charging cycles did not affect the integration of the layered crystal structures of NMC622. Previous studies on layer NMC materials revealed the expansion of lattice constant *c* and the shrinkage of *a* when Li ions were de-intercalated from the layered structure [250,251]. Compared to the pristine NMC622, the (018) peaks of all the cycled electrodes shift to smaller angles (expansion of *c*) while the (110) peaks shift to larger angles (shrinkage of *a*), indicating the loss of Li ions in the Li ions layer of the structure. This is in accordance with the Li half-cell testing result in **Figure 4.4** and XAS result in **Figure 4.5**.

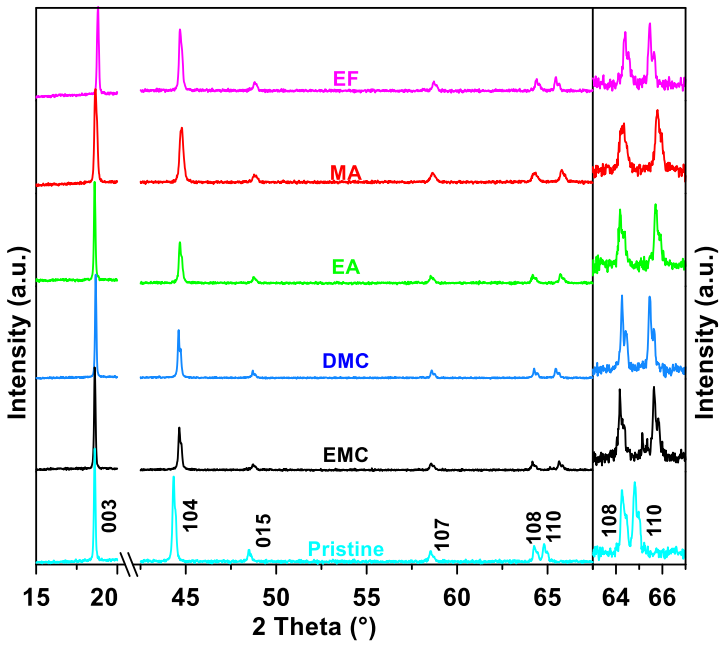

Figure 4.6. XRD patterns of pristine and cycled NMC622 electrodes after 200 fast charging cycles.

Figure 4.7 shows the Li ion concentration remaining in the electrolyte after 200 fast charging cycles measured by ICP-OES. The results show an increase of Li ion concentration in all electrolytes with different solvents after repeated fast charging cycles compared to the original Li ion concentration. Thompson et al have shown that Li ion concentration stay unchanged when cells are charged/discharged at low rate of C/3 [93]. This suggests that the solvent components are consumed at a higher rate compared to Li ions in the salt. Since the reductions of the solvent molecules are electrochemically induced reduction occurring on the negative electrodes [42,252], the high current fast charging and metallic Li plating on graphite may promote the solvent reduction and thus lead to the higher consuming rate of solvents in the electrolyte.

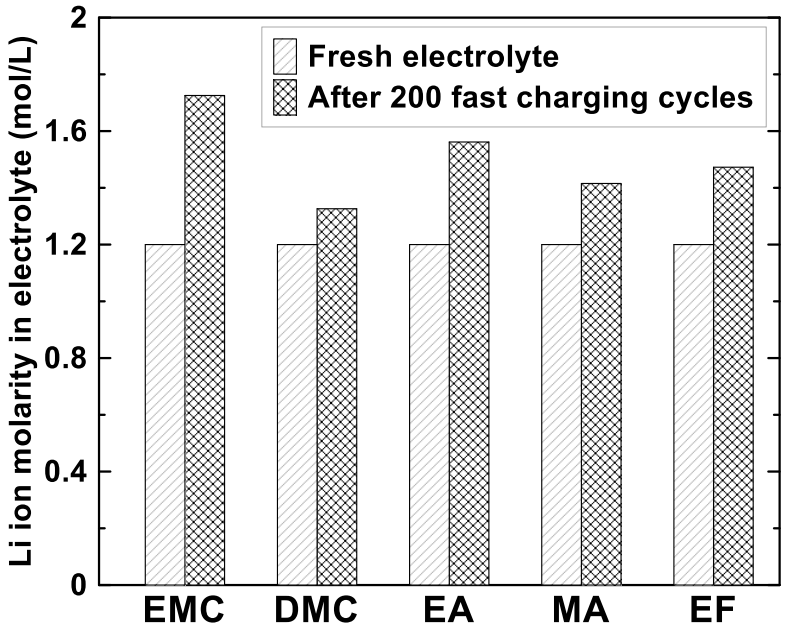

Figure 4.7. Change of salt concentration in the electrolyte after 200 fast charging cycles.

The surface chemistry on both negative and positive electrodes is studied by XPS after formation and after 200 fast-charging cycles. **Figure 4.8** and **Figure 4.9** show the detailed analysis of F1s, C1s, O1s and P2p for solid electrolyte interphase (SEI) on graphite electrodes and cathode electrolyte interphase (CEI) on NMC622 electrodes. It is well known that the SEI and CEI consist mainly of organic components including $(CH_2OCO_2Li)_2$ (lithium ethylene decarbonate, LEDC), organic carbonate (R_2CO_3), polyethylene glycol (PEO) oligomer, etc., and inorganic compounds such as Li_2CO_3, LiF, Li_2O, $LiPF_xO_y$ and Li_xPF_y [253–256]. The detailed peak assignments for the SEI/CEI layers are summarized on **Table S2 and S3**.

By comparing the F 1s spectra in **Figure 4.8a** between the pristine graphite electrode and electrodes after formation, a new Li-F peak at ~685 eV evolved which is from the decomposition of $LiPF_6$ [257]. The C-F peak is from the PVDF binder in the electrodes. In **Figure 4.8b**, the area ratio of Li-F/C-F is increased in all five samples compared to the counterparts in **Figure 4.8**a, indicating the increase of SEI thickness after 200 fast-charging cycles. In the DMC case, the area ratio of Li-F/C-F is the lowest, suggesting the thinnest SEI during fast charging cycles, which can be related to its best fast charging performance. In the C1s spectra, the peaks at 286.4, 288.6 and 289.8 are assigned to CO-, CO_2- and CO_3- like carbon environments which are from the reduction of solvents at the graphite surface besides the C-C in graphite and Li-C from residual Li in graphite

[253,258–260]. This solvent reduction is also confirmed in the O1s spectra. Compared to the pristine sample, the O1s spectra evolved with two peaks after formation and after the 200 fast-charging cycles. The peak at ~532 eV is assigned to CO_2-like oxygen from carbonate compounds such as lithium alkyl carbonates (ROCO2Li) and/or lithium carbonate; the second peak at ~533.6 eV is assigned to –C–O– bonds from $ROCO_2Li$ and/or ether derivatives [261,262]. The increase of the latter one after fast charging cycles is probably due to the increase of more ether derivatives such as PEO-like polymers [263,264]. PEO formation has been suggested to occur through PF_5 catalyzed electrolyte solvent polymerization reactions [263]. The P 2p spectra evolved after formation cycles of the cells due to $LiPF_6$ decomposition and the intensity increased after fast charging cycles. The P–F peaks are ascribed to the reduction of $LiPF_6$ on the graphite to form PF_5 and Li_xPF_y [265], and the P=O peaks are assigned to the $LiP_xO_yF_z$ from the hydrolysis $LiPF_6$ with trace water in the electrolyte [258].

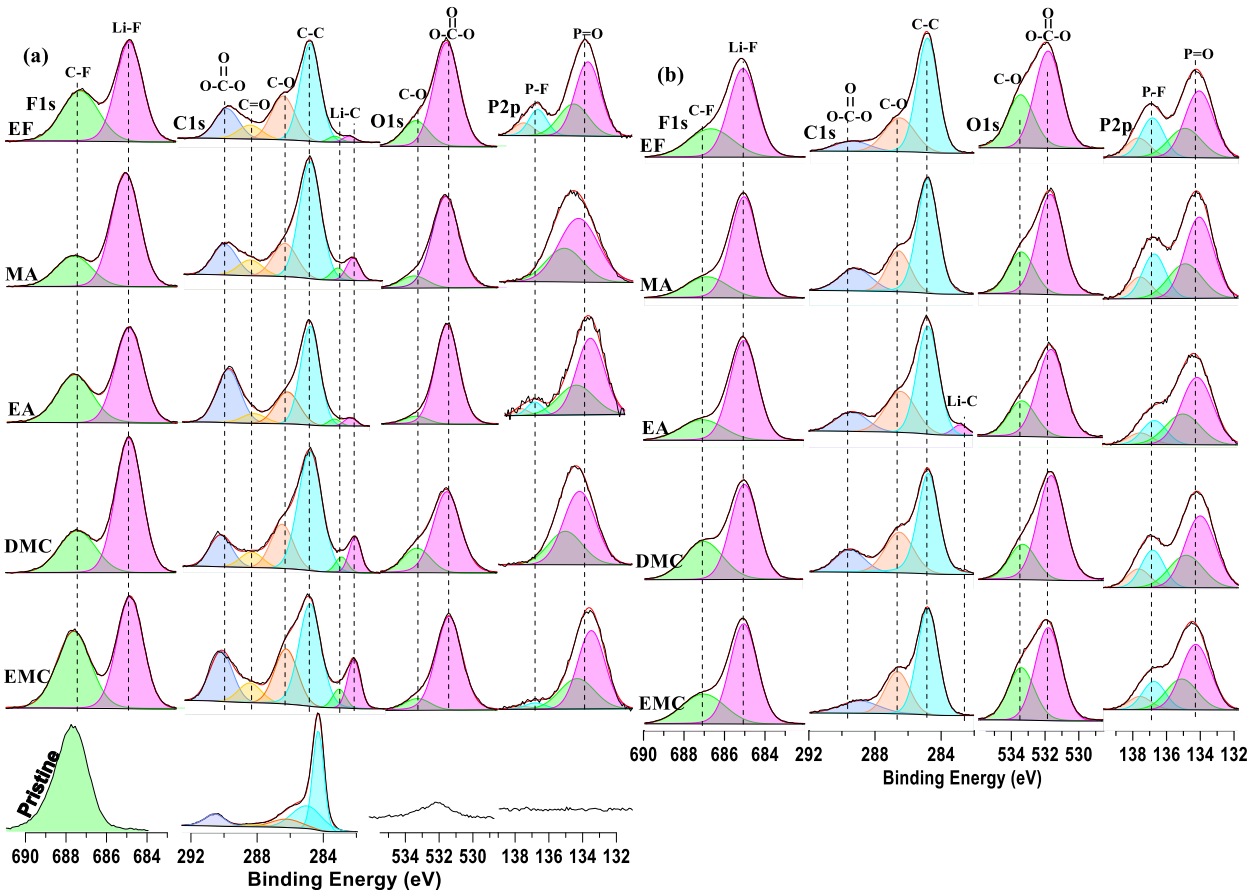

Figure 4.8. XPS spectra of negative electrodes (a) after formation cycles and (b) after 200 fast-charging cycles in cells with different electrolytes.

Figure 4.9 shows the F 1s, C 1s, O 1s and P 2p XPS spectra pf the NMC622 electrodes in pristine state, after formation and after 200 fast-charging cycles. In the F 1s spectra (**Figure 4.9a**), similar $LiPF_6$ decomposition occurred and LiF peak evolved after formation cycles besides the C-F peak from the PVDF binder. In **Figure 4.9b**, the intensity of Li-F increases for all five different solvent systems, indicating the increase of CEI thickness after 200 fast-charging cycles. The area ratio of Li-F/C-F in carbonates (DMC and EMC) is the lower than that in esters (EA, MA and EF), indicating a thinner and stable CEI in carbonate electrolytes. This is in accordance with the cycling performance shown in **Figure 4.3**. The C 1s spectra show little change between the pristine sample and the electrodes after formation in all five electrolytes. The peaks in C 1s spectra are ascribed to the PVDF binder and carbon blacks in the electrodes. The O 1s spectrum of the pristine electrode showed two peaks with the peak at 529.5 eV attributed to M-O from the lattice oxygen in NMC622 [262] and the peak at 531.5 eV assigned to CO_x-like oxygen from the carbon black [260]. After formation cycles, the O 1s peaks from the pristine electrode at 531.5 eV was replaced by two new peaks at ~531.7 and ~533.5 eV indicating the formation of CEI layers from electrolyte decomposition. The peak at ~531.7 is ascribed to CO_2-like oxygen from carbonate compounds ($ROCO_2Li$) and/or Li_2CO_3 [262,266], and the peak at ~533.5 eV is assigned to C–O bonds from ether derivatives and/or $ROCO_2Li$ [261,262]. After repeated fast-charging cycles, the intensity of CO_2-/C-O increased greatly by comparing the M-O peak, indicating the continuous decomposition of electrolyte and formation of carbonate compounds in the CEI layer. For the EF case, the M-O peak almost disappeared, indicating the CEI in this electrolyte is the thickest. This suggests the CEI may be not stable when EF is present in the electrolyte. The P-F and P=O peaks are shown after formation in P 2p spectra compared to the blank feature in pristine sample. The P-F/P=O peaks grow in intensity after fast charging cycles, which is another indication of the CEI growth from the salt decomposition.

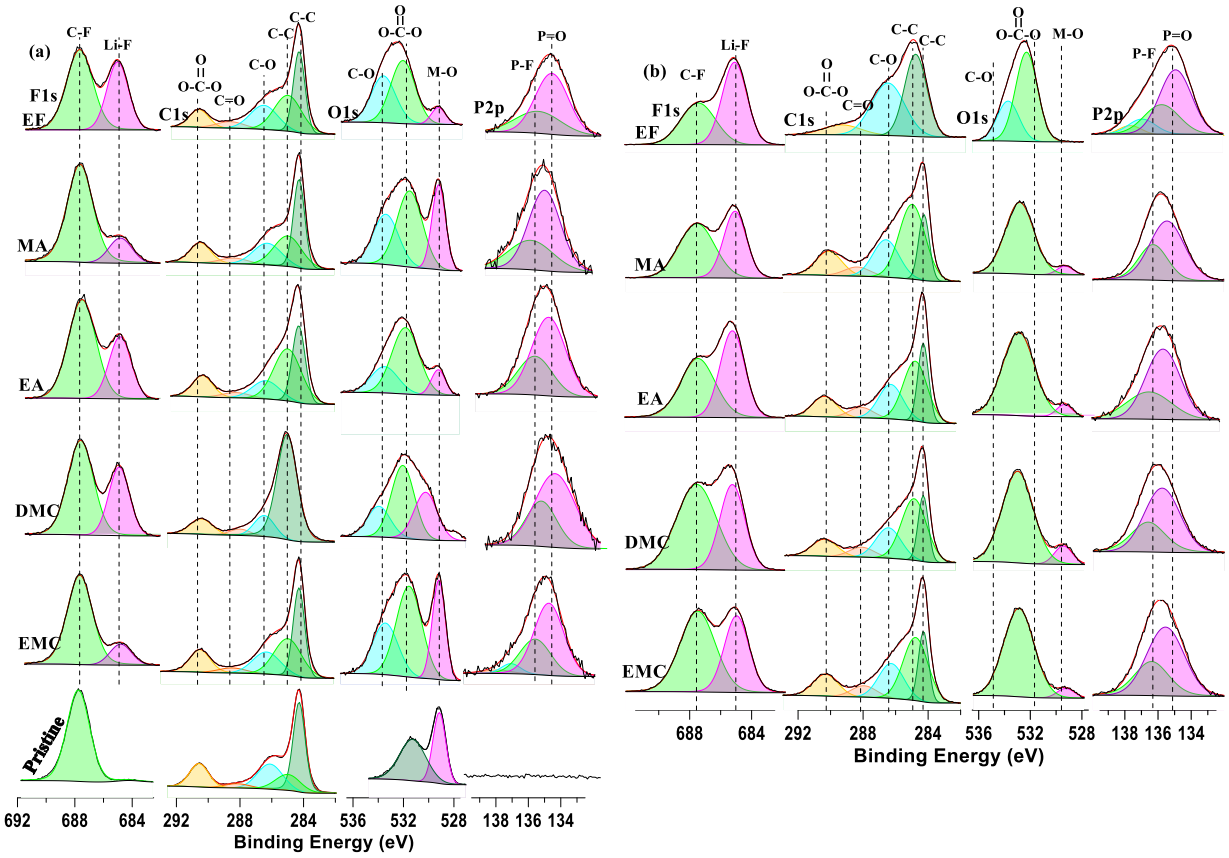

Figure 4.9. XPS spectra of positive electrodes (a) after formation cycles and (b) after 200 fast-charging cycles in cells with different electrolytes.

Figure 4.10 shows the evolution of the elemental ratio changes in SEI and CEI after formation and after 200 fast charging cycles. The electrolyte with DMC shows the smallest elemental change in **Figure 4.10a**, indicating the SEI is stable during fast-charging cycles. This agrees with the best fast-charging cycling performance in this electrolyte. The CEI elemental ratios in DMC, EMC and EA are stable in **Figure 4.10b**. In contrary, the MA and EF show notable changes, indicating an unstable interface during fast-charging cycles.

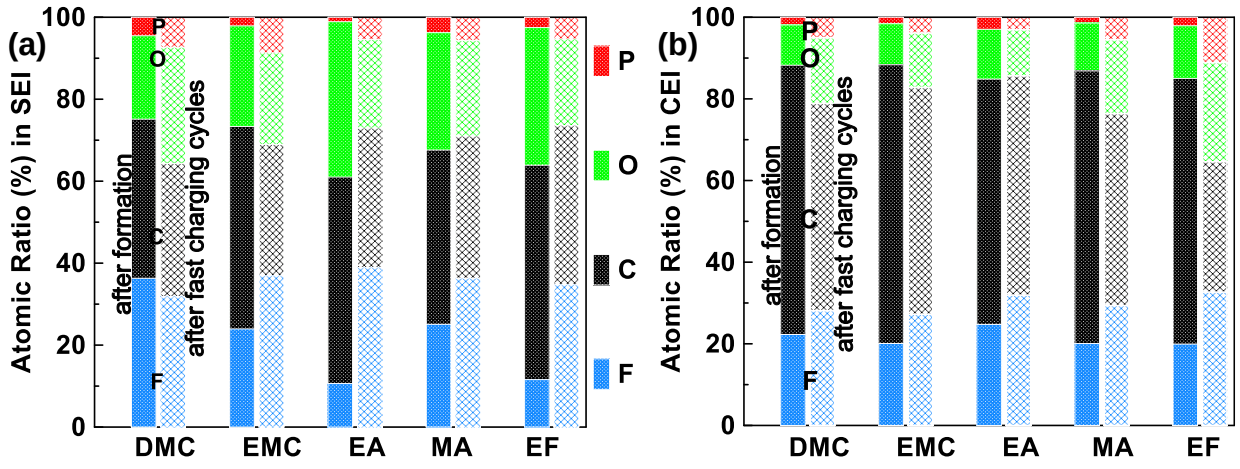

Figure 4.10. The evolution of atomic ratios among F, C, O and P for (a) SEI and (b) CEI after formation (75% filling) and after 200 fast charging cycles (diagonal cross).

4.4 Conclusions

Electrolytes with different solvent formulations were tested for fast charging of NMC622-graphite Li-ion cells. The conductivity of the electrolytes was increased by adding co-solvents such as EF, MA, EA, DMC into the EC/EMC based electrolyte formulation, and the capacity obtained from the fast charging was improved from the higher conductivity. However, different cycling performance was observed with the trend of performance in the sequence of DMC > EMC > EA > MA > EF. The lithium plating on graphite electrodes, the structural changes in NMC622 and the lithium inventory loss were analyzed after repeated fast-charging cycles. They were in accordance with the cycling performance. The Li salt/solvent ratio after repeated cycles showed the solvent was consumed faster than Li salt with an increase Li salt molarity in ICP-OES test. The SEI and CEI in different electrolyte formulations were analyzed by XPS. Both the SEI and CEI for DMC are thin and stable during fast charging cycles, compared to other solvent formulations. The present results suggest that DMC in the electrolyte formulation is encouraged in developing fast charging technologies for Li-ion cells.

5. CONCLUSIONS AND OUTLOOK

5.1 Summary and conclusions

Given its effect on the global BEV market, the realization of XFC has been attracting attention from the whole community. Considering fundamental electrochemistry principles of LIBs, it is well recognized that mitigation/prevention of Li plating is the most critical task for XFC. Thus, enhancing Li^+ transport properties within LIBs plays an irreplaceable role.

For LIBs under XFC, it is straightforward to probe the effects of increasing charging rates on LIBs. In this study, from the effects of increasing charging rates from 1C, 4C to 6C, to the structural evolution of both NMC622 cathode and graphite anode, and the utilization of various cosolvents in improving the rate performance, they were systematically studied via various characterization methods to realize the extreme fast charging of LIBs. Based on the findings obtained, it was realized that phase transitions within both NMC622 cathode, and graphite anode also plays a vital role for our understanding and further optimization of LIBs under XFC. Then, *operando* NPD experiments on cylindrical NMC622||graphite cell were implemented. Meanwhile, based on our findings for the whole LIBs system, it was realized that tuning transport properties of liquid electrolytes utilized by LIBs would contribute to enhanced rate performance for LIBs. Thus, we further probed various liquid electrolyte systems with different cosolvents. The main conclusions we find in our study are summarized here:

- Less available capacities are obtained under increasing charging rates, due to larger polarization/overpotential introduced into LIBs. For cycled electrodes, the crystal structure of the graphite anode remains the same, while the NMC622 cathode experience irreversible structural evolution due to loss of active Li^+ during the long term cycling. Also, the liquid electrolyte experiences relatively faster aging under higher charging rates, as revealed by the higher Li^+ concentration within cycled electrolytes.
- The crystal structure of NMC622 is mainly determined by Li^+ contents within it, and lattice *a* experiences a steady decreasing trend during the charging process while lattice *c* goes through a first increase and then decrease trend due to competing electrostatic force. For the phase transition of lithiated graphite, it shows

a typical sequential transition process under a slow charging rate: from pure graphite → stage III (LiC_{30}) → stage II (LiC_{12}) → stage I (LiC_6). While under a higher charging rate, the LiC_{12} and LiC_6 phases may coexist due to the inhomogeneous distribution of Li^+ under high charging rates. Further analysis via the JMAK model indicates that the $LiC_{12} \rightarrow LiC_6$ transition is a diffusion controlled, one-dimensional process with decreasing nucleation rate under increasing charging rates.

- Utilization of cosolvents with lower viscosity indeed improves the ion conductivity of liquid electrolytes, leading to enhanced rate performance. Via XAS and XRD on cycled NMC622, the increased valence state of Ni within NMC622 are consistent with its structural evolution. For the long term cycling performance, the solvent using dimethyl carbonate (DMC) dominates all tested electrolytes. Via comparison of the chemical components formed between electrolyte and electrode, the dominant performance of DMC is attributed to its capability to form more stable interphases with both NMC622 cathode and a graphite anode.

5.2 Outlook and future work

In our thesis work, we focus mainly on strategies to improve Li^+ transport properties to hinder the occurrence of Li plating on graphite anode. However, another strategy is to "accept" Li plating and make sure LIBs can even cycle a certain number of cycles with plated Li. Recently, significant progress has been made for LIBs using Li metal as the anode, via tuning liquid electrolytes and forming more stable SEI on Li metal. Thus, it is worth trying to tune the transport properties of liquid electrolytes developed for Li metal anode and get a tradeoff between cycling performance and cycle lives.

For future work, we want to further test the effects of various additives at trace concentrations on improving the long term cycling performance of LIBs under higher charging rates, given their validity in improving the long term cycling performance at relatively smaller charging rates well proven by the industry. Generally, additives sacrifice themselves via earlier reactions with electrodes, thus preventing the side reaction between organic solvents and electrodes. Then the aging of liquid electrolytes will be significantly mitigated/postponed. Fluorine electrolytes, which indicate replacing hydrogen within the solvent molecules with fluorine, were

widely seen as a promising solution to form a more stable SEI with graphite anode. Previous studies are mainly based on trial-and-error methods, and it is time-consuming to find additives with expected improvement. These days, more efficient screening of additives combing simulation and experiments will accelerate the study and commercialization of novel additives via high throughput theoretical computation.

Meanwhile, utilization of advanced slurry preparation/coating techniques, both leading to well-patterned coating for cathode and anode, has been well proven into an excellent way to decrease the tortuosity for LIBs. For reduced tortuosity within electrodes, it will indefinitely reduce the polarization/overpotential within liquid electrolytes as the diffusion path for Li^+ will be greatly shortened. This will definitely reduce the inhomogeneity of Li^+ within electrodes and extend the ratio CC stage under the CCCV charging protocol, thus enhancing the performance under XFC.

Besides these strategies focusing on liquid electrolytes and the structure of coated electrodes, utilization of electrodes with higher specific capacity and higher Li^+ diffusion is straightforward and will contribute significantly to the realization of XFC for LIBs. The NMC622 cathode probed in this study possesses a theoretical specific capacity of ~180 mAh/g. The $LiNiO_2$ cathode material, as the end member of $LiTMO_2$ cathode, possesses a theoretical capacity of ~270 mAh/g. Then the replacement of NMC622 with $LiNiO_2$ will significantly reduce the thickness of coated cathode, leading to reduced polarization within the cathode side and improvement of rate performance for the same energy density. At this stage, the commercial utilization of $LiNiO_2$ still suffers from its structural instability during the H2 → H3 phase transition and with severe side reaction between Ni^{3+}/ Ni^{4+} of $LiNiO_2$ and liquid electrolyte under high SOC. Recent progress on high nickel/cobalt-free cathode via replacing oxygen with fluorine for $LiTMO_2$ and doping $LiNiO_2$ with Al, Mg will mitigate these challenges and accelerate the commercial application of high nickel cathodes.

Combining all these strategies, we believe extreme fast charging for LIBs will be realized in the coming days and contribute significantly to the energy revolution from fossil fuel energies to cleaner renewable energies.

REFERENCES

[1] B. Looney, BP statistical review of world energy, (2020).

[2] E. D'Andrea, N. Rezaie, P. Prislan, J. Gričar, A. Collalti, J. Muhr, G. Matteucci, Frost and drought: Effects of extreme weather events on stem carbon dynamics in a Mediterranean beech forest, Plant. Cell Environ. 43 (2020) 2365–2379.

[3] R.P. Gregory, Climate disasters, carbon dioxide, and financial fundamentals, Q. Rev. Econ. Financ. 79 (2021) 45–58.

[4] S. Kacker, Our very own Inconvenient Truth: Carbon Neutrality and Climate Change, (2018).

[5] F. Schreyer, G. Luderer, R. Rodrigues, R.C. Pietzcker, L. Baumstark, M. Sugiyama, R.J. Brecha, F. Ueckerdt, Common but differentiated leadership: strategies and challenges for carbon neutrality by 2050 across industrialized economies, Environ. Res. Lett. 15 (2020) 114016.

[6] Z. Jia, B. Lin, How to achieve the first step of the carbon-neutrality 2060 target in China: the coal substitution perspective, Energy. (2021) 121179.

[7] B. Diouf, R. Pode, Potential of lithium-ion batteries in renewable energy, Renew. Energy. 76 (2015) 375–380. https://doi.org/10.1016/J.RENENE.2014.11.058.

[8] G. Crabtree, Perspective: The energy-storage revolution, Nature. 526 (2015) S92–S92. https://doi.org/10.1038/526S92a.

[9] M.A. Pellow, H. Ambrose, D. Mulvaney, R. Betita, S. Shaw, Research gaps in environmental life cycle assessments of lithium ion batteries for grid-scale stationary energy storage systems: End-of-life options and other issues, Sustain. Mater. Technol. 23 (2020) e00120. https://doi.org/10.1016/J.SUSMAT.2019.E00120.

[10] S. Ahmed, I. Bloom, A.N. Jansen, T. Tanim, E.J. Dufek, A. Pesaran, A. Burnham, R.B. Carlson, F. Dias, K. Hardy, M. Keyser, C. Kreuzer, A. Markel, A. Meintz, C. Michelbacher, M. Mohanpurkar, P.A. Nelson, D.C. Robertson, D. Scoffield, M. Shirk, T. Stephens, R. Vijayagopal, J. Zhang, Enabling fast charging – A battery technology gap assessment, J. Power Sources. 367 (2017) 250–262. https://doi.org/10.1016/j.jpowsour.2017.06.055.

[11] T. Chen, Y. Jin, H. Lv, A. Yang, M. Liu, B. Chen, Y. Xie, Q. Chen, Applications of lithium-ion batteries in grid-scale energy storage systems, Trans. Tianjin Univ. 26 (2020) 208–217.

[12] E.R. Logan, J.R. Dahn, Electrolyte Design for Fast-Charging Li-Ion Batteries, Trends Chem. 2 (2020) 354–366. https://doi.org/https://doi.org/10.1016/j.trechm.2020.01.011.

[13] D. Ronanki, A. Kelkar, S.S. Williamson, Extreme Fast Charging Technology—Prospects to Enhance Sustainable Electric Transportation, Energies. 12 (2019). https://doi.org/10.3390/en12193721.

[14] A. Tomaszewska, Z. Chu, X. Feng, S. O'Kane, X. Liu, J. Chen, C. Ji, E. Endler, R. Li, L. Liu, Y. Li, S. Zheng, S. Vetterlein, M. Gao, J. Du, M. Parkes, M. Ouyang, M. Marinescu, G. Offer, B. Wu, Lithium-ion battery fast charging: A review, ETransportation. 1 (2019) 100011. https://doi.org/https://doi.org/10.1016/j.etran.2019.100011.

[15] G.-L. Zhu, C.-Z. Zhao, J.-Q. Huang, C. He, J. Zhang, S. Chen, L. Xu, H. Yuan, Q. Zhang, Fast Charging Lithium Batteries: Recent Progress and Future Prospects, Small. 15 (2019) 1805389. https://doi.org/https://doi.org/10.1002/smll.201805389.

[16] W. Cai, Y.-X. Yao, G.-L. Zhu, C. Yan, L.-L. Jiang, C. He, J.-Q. Huang, Q. Zhang, A review on energy chemistry of fast-charging anodes, Chem. Soc. Rev. 49 (2020) 3806–3833. https://doi.org/10.1039/c9cs00728h.

[17] W. Xie, X. Liu, R. He, Y. Li, X. Gao, X. Li, Z. Peng, S. Feng, X. Feng, S. Yang, Challenges and opportunities toward fast-charging of lithium-ion batteries, J. Energy Storage. 32 (2020) 101837. https://doi.org/10.1016/J.EST.2020.101837.

[18] M. Li, M. Feng, D. Luo, Z. Chen, Fast Charging Li-Ion Batteries for a New Era of Electric Vehicles, Cell Reports Phys. Sci. 1 (2020) 100212. https://doi.org/https://doi.org/10.1016/j.xcrp.2020.100212.

[19] M. Weiss, R. Ruess, J. Kasnatscheew, Y. Levartovsky, N.R. Levy, P. Minnmann, L. Stolz, T. Waldmann, M. Wohlfahrt-Mehrens, D. Aurbach, M. Winter, Y. Ein-Eli, J. Janek, Fast Charging of Lithium-Ion Batteries: A Review of Materials Aspects, Adv. Energy Mater. 11 (2021) 2101126. https://doi.org/https://doi.org/10.1002/aenm.202101126.

[20] A. Manthiram, A reflection on lithium-ion battery cathode chemistry, Nat. Commun. 11 (2020) 1550. https://doi.org/10.1038/s41467-020-15355-0.

[21] M.M. Thackeray, K. Amine, LiMn2O4 spinel and substituted cathodes, Nat. Energy. 6 (2021) 566. https://doi.org/10.1038/s41560-021-00815-8.

[22] P. Peljo, H.H. Girault, Electrochemical potential window of battery electrolytes: the HOMO–LUMO misconception, Energy Environ. Sci. 11 (2018) 2306–2309. https://doi.org/10.1039/C8EE01286E.

[23] A. Grimaud, W.T. Hong, Y. Shao-Horn, J.M. Tarascon, Anionic redox processes for electrochemical devices, Nat. Mater. 15 (2016) 121–126. https://doi.org/10.1038/nmat4551.

[24] M. Ben Yahia, J. Vergnet, M. Saubanère, M.-L. Doublet, Unified picture of anionic redox in Li/Na-ion batteries, Nat. Mater. 18 (2019) 496–502. https://doi.org/10.1038/s41563-019-0318-3.

[25] J.B. Goodenough, K. Park, The Li-Ion Rechargeable Battery : A Perspective, (2013). https://doi.org/10.1021/ja3091438.

[26] E. Peled, The electrochemical behavior of alkali and alkaline earth metals in nonaqueous battery systems—the solid electrolyte interphase model, J. Electrochem. Soc. 126 (1979) 2047.

[27] A. Wang, S. Kadam, H. Li, S. Shi, Y. Qi, Review on modeling of the anode solid electrolyte interphase (SEI) for lithium-ion batteries, Npj Comput. Mater. 4 (2018) 15. https://doi.org/10.1038/s41524-018-0064-0.

[28] W. Zuo, M. Luo, X. Liu, J. Wu, H. Liu, J. Li, M. Winter, R. Fu, W. Yang, Y. Yang, Li-rich cathodes for rechargeable Li-based batteries: reaction mechanisms and advanced characterization techniques, Energy Environ. Sci. 13 (2020) 4450–4497.

[29] Z. Du, D.L. Wood, C. Daniel, S. Kalnaus, J. Li, Understanding limiting factors in thick electrode performance as applied to high energy density Li-ion batteries, J. Appl. Electrochem. 47 (2017) 405–415.

[30] A. Van der Ven, G. Ceder, Lithium diffusion mechanisms in layered intercalation compounds, J. Power Sources. 97–98 (2001) 529–531. https://doi.org/https://doi.org/10.1016/S0378-7753(01)00638-3.

[31] A. Van der Ven, Lithium Diffusion in Layered Li[sub x]CoO[sub 2], Electrochem. Solid-State Lett. 3 (1999) 301. https://doi.org/10.1149/1.1391130.

[32] Y. Wei, J. Zheng, S. Cui, X. Song, Y. Su, W. Deng, Z. Wu, X. Wang, W. Wang, M. Rao, Y. Lin, C. Wang, K. Amine, F. Pan, Kinetics Tuning of Li-Ion Diffusion in Layered Li(NixMnyCoz)O2, J. Am. Chem. Soc. 137 (2015) 8364–8367. https://doi.org/10.1021/jacs.5b04040.

[33] K. Kang, G. Ceder, Factors that affect Li mobility in layered lithium transition metal oxides, Phys. Rev. B. 74 (2006) 94105. https://doi.org/10.1103/PhysRevB.74.094105.

[34] S.S. Zhang, Design aspects of electrolytes for fast charge of Li-ion batteries, InfoMat. 3 (2021) 125–130. https://doi.org/10.1002/inf2.12159.

[35] Q. Liu, S. Li, S. Wang, X. Zhang, S. Zhou, Y. Bai, J. Zheng, X. Lu, Kinetically Determined Phase Transition from Stage II (LiC12) to Stage i (LiC6) in a Graphite Anode for Li-Ion Batteries, J. Phys. Chem. Lett. 9 (2018) 5567–5573. https://doi.org/10.1021/acs.jpclett.8b02750.

[36] K. Xu, Nonaqueous Liquid Electrolytes for Lithium-Based Rechargeable Batteries, Chem. Rev. 104 (2004) 4303–4418. https://doi.org/10.1021/cr030203g.

[37] K. Xu, Electrolytes and Interphases in Li-Ion Batteries and Beyond, Chem. Rev. 114 (2014) 11503–11618. https://doi.org/10.1021/cr500003w.

[38] X. Han, L. Lu, Y. Zheng, X. Feng, Z. Li, J. Li, M. Ouyang, A review on the key issues of the lithium ion battery degradation among the whole life cycle, ETransportation. 1 (2019) 100005. https://doi.org/https://doi.org/10.1016/j.etran.2019.100005.

[39] J.S. Edge, S. O'Kane, R. Prosser, N.D. Kirkaldy, A.N. Patel, A. Hales, A. Ghosh, W. Ai, J. Chen, J. Yang, S. Li, M.C. Pang, L. Bravo Diaz, A. Tomaszewska, M.W. Marzook, K.N. Radhakrishnan, H. Wang, Y. Patel, B. Wu, G.J. Offer, Lithium ion battery degradation: what you need to know, Phys. Chem. Chem. Phys. 23 (2021) 8200–8221. https://doi.org/10.1039/d1cp00359c.

[40] C. Fang, X. Wang, Y.S. Meng, Key Issues Hindering a Practical Lithium-Metal Anode, Trends Chem. 1 (2019) 152–158. https://doi.org/https://doi.org/10.1016/j.trechm.2019.02.015.

[41] D. Aurbach, E. Zinigrad, Y. Cohen, H. Teller, A short review of failure mechanisms of lithium metal and lithiated graphite anodes in liquid electrolyte solutions, Solid State Ionics. 148 (2002) 405–416. https://doi.org/https://doi.org/10.1016/S0167-2738(02)00080-2.

[42] S.S. Zhang, A review on electrolyte additives for lithium-ion batteries, J. Power Sources. 162 (2006) 1379–1394. https://doi.org/https://doi.org/10.1016/j.jpowsour.2006.07.074.

[43] A.M. Haregewoin, A.S. Wotango, B.-J. Hwang, Electrolyte additives for lithium ion battery electrodes: progress and perspectives, Energy Environ. Sci. 9 (2016) 1955–1988.

[44] J. Ming, Z. Cao, Y. Wu, W. Wahyudi, W. Wang, X. Guo, L. Cavallo, J.-Y. Hwang, A. Shamim, L.-J. Li, Y.-K. Sun, H.N. Alshareef, New Insight on the Role of Electrolyte Additives in Rechargeable Lithium Ion Batteries, ACS Energy Lett. 4 (2019) 2613–2622. https://doi.org/10.1021/acsenergylett.9b01441.

[45] F. Lin, I.M. Markus, D. Nordlund, T.C. Weng, M.D. Asta, H.L. Xin, M.M. Doeff, Surface reconstruction and chemical evolution of stoichiometric layered cathode materials for lithium-ion batteries, Nat. Commun. 5 (2014) 3529. https://doi.org/10.1038/ncomms4529.

[46] J. Li, H. Liu, J. Xia, A.R. Cameron, M. Nie, G.A. Botton, J.R. Dahn, The Impact of Electrolyte Additives and Upper Cut-off Voltage on the Formation of a Rocksalt Surface Layer in {LiNi}0.8Mn0.1Co0.1O2Electrodes, J. Electrochem. Soc. 164 (2017) A655--A665. https://doi.org/10.1149/2.0651704jes.

[47] R. Tatara, P. Karayaylali, Y. Yu, Y. Zhang, L. Giordano, F. Maglia, R. Jung, J.P. Schmidt, I. Lund, Y. Shao-Horn, The Effect of Electrode-Electrolyte Interface on the Electrochemical Impedance Spectra for Positive Electrode in Li-Ion Battery, J. Electrochem. Soc. 166 (2018) A5090–A5098. https://doi.org/10.1149/2.0121903jes.

[48] L. Giordano, P. Karayaylali, Y. Yu, Y. Katayama, F. Maglia, S. Lux, Y. Shao-Horn, Chemical reactivity descriptor for the oxide-electrolyte interface in Li-ion batteries, J. Phys. Chem. Lett. 8 (2017) 3881–3887.

[49] Y. Zhang, Y. Katayama, R. Tatara, L. Giordano, Y. Yu, D. Fraggedakis, J.G. Sun, F. Maglia, R. Jung, M.Z. Bazant, Y. Shao-Horn, Revealing electrolyte oxidation: Via carbonate dehydrogenation on Ni-based oxides in Li-ion batteries by in situ Fourier transform infrared spectroscopy, Energy Environ. Sci. 13 (2020) 183–199. https://doi.org/10.1039/c9ee02543j.

[50] R. Xu, H. Sun, L.S. De Vasconcelos, K. Zhao, Mechanical and structural degradation of LiNixMnyCozO2 cathode in Li-ion batteries: An experimental study, J. Electrochem. Soc. 164 (2017) A3333–A3341. https://doi.org/10.1149/2.1751713jes.

[51] R. Xu, K. Zhao, Corrosive fracture of electrodes in Li-ion batteries, J. Mech. Phys. Solids. 121 (2018) 258–280. https://doi.org/10.1016/J.JMPS.2018.07.021.

[52] R. Xu, Y. Yang, F. Yin, P. Liu, P. Cloetens, Y. Liu, F. Lin, K. Zhao, Heterogeneous damage in Li-ion batteries: Experimental analysis and theoretical modeling, J. Mech. Phys. Solids. 129 (2019) 160–183. https://doi.org/10.1016/J.JMPS.2019.05.003.

[53] Y. Yang, R. Xu, K. Zhang, S.-J. Lee, L. Mu, P. Liu, C.K. Waters, S. Spence, Z. Xu, C. Wei, D.J. Kautz, Q. Yuan, Y. Dong, Y.-S. Yu, X. Xiao, H.-K. Lee, P. Pianetta, P. Cloetens, J.-S. Lee, K. Zhao, F. Lin, Y. Liu, Quantification of Heterogeneous Degradation in Li-Ion Batteries, Adv. Energy Mater. 9 (2019) 1900674. https://doi.org/https://doi.org/10.1002/aenm.201900674.

[54] K.-H. Chen, M.J. Namkoong, V. Goel, C. Yang, S. Kazemiabnavi, S.M. Mortuza, E. Kazyak, J. Mazumder, K. Thornton, J. Sakamoto, N.P. Dasgupta, Efficient fast-charging of lithium-ion batteries enabled by laser-patterned three-dimensional graphite anode architectures, J. Power Sources. 471 (2020) 228475. https://doi.org/10.1016/j.jpowsour.2020.228475.

[55] X.G. Yang, T. Liu, Y. Gao, S. Ge, Y. Leng, D. Wang, C.Y. Wang, Asymmetric Temperature Modulation for Extreme Fast Charging of Lithium-Ion Batteries, Joule. 3 (2019) 3002–3019. https://doi.org/10.1016/j.joule.2019.09.021.

[56] K.R. Tallman, B. Zhang, L. Wang, S. Yan, K. Thompson, X. Tong, J. Thieme, A. Kiss, A.C. Marschilok, K.J. Takeuchi, D.C. Bock, E.S. Takeuchi, Anode Overpotential Control via Interfacial Modification: Inhibition of Lithium Plating on Graphite Anodes, ACS Appl. Mater. Interfaces. 11 (2019) 46864–46874. https://doi.org/10.1021/acsami.9b16794.

[57] Z. Du, D.L. Wood, I. Belharouak, Enabling fast charging of high energy density Li-ion cells with high lithium ion transport electrolytes, Electrochem. Commun. 103 (2019) 109–113. https://doi.org/10.1016/j.elecom.2019.04.013.

[58] J. Billaud, F. Bouville, T. Magrini, C. Villevieille, A.R. Studart, Magnetically aligned graphite electrodes for high-rate performance Li-ion batteries, Nat. Energy. 1 (2016) 16097. https://doi.org/10.1038/nenergy.2016.97.

[59] D. Dang, Y. Wang, S. Gao, Y.-T. Cheng, Freeze-dried low-tortuous graphite electrodes with enhanced capacity utilization and rate capability, Carbon N. Y. 159 (2020) 133–139. https://doi.org/https://doi.org/10.1016/j.carbon.2019.12.036.

[60] S. Park, S.Y. Jeong, T.K. Lee, M.W. Park, H.Y. Lim, J. Sung, J. Cho, S.K. Kwak, S.Y. Hong, N.-S. Choi, Replacing conventional battery electrolyte additives with dioxolone derivatives for high-energy-density lithium-ion batteries, Nat. Commun. 12 (2021) 838. https://doi.org/10.1038/s41467-021-21106-6.

[61] H. Liu, Z. Zhu, Q. Yan, S. Yu, X. He, Y. Chen, R. Zhang, L. Ma, T. Liu, M. Li, R. Lin, Y. Chen, Y. Li, X. Xing, Y. Choi, L. Gao, H.S. Cho, K. An, J. Feng, R. Kostecki, K. Amine, T. Wu, J. Lu, H.L. Xin, S.P. Ong, P. Liu, A disordered rock salt anode for fast-charging lithium-ion batteries, Nature. 585 (2020) 63–67. https://doi.org/10.1038/s41586-020-2637-6.

[62] K. Siegbahn, K. Edvarson, β-Ray spectroscopy in the precision range of 1 : 105, Nucl. Phys. 1 (1956) 137–159. https://doi.org/https://doi.org/10.1016/S0029-5582(56)80022-9.

[63] L. Ley, R.A. Pollak, F.R. McFeely, S.P. Kowalczyk, D.A. Shirley, Total valence-band densities of states of III-V and II-VI compounds from x-ray photoemission spectroscopy, Phys. Rev. B. 9 (1974) 600–621. https://doi.org/10.1103/PhysRevB.9.600.

[64] R.I.R. Blyth, H. Buqa, F.P. Netzer, M.G. Ramsey, J.O. Besenhard, P. Golob, M. Winter, XPS studies of graphite electrode materials for lithium ion batteries, Appl. Surf. Sci. 167 (2000) 99–106. https://doi.org/https://doi.org/10.1016/S0169-4332(00)00525-0.

[65] R. Petibon, L. Rotermund, K.J. Nelson, A.S. Gozdz, J. Xia, J.R. Dahn, Study of Electrolyte Components in Li Ion Cells Using Liquid-Liquid Extraction and Gas Chromatography Coupled with Mass Spectrometry, J. Electrochem. Soc. 161 (2014) A1167–A1172. https://doi.org/10.1149/2.117406jes.

[66] L. Madec, L. Ma, K.J. Nelson, R. Petibon, J.-P. Sun, I.G. Hill, J.R. Dahn, The Effects of a Ternary Electrolyte Additive System on the Electrode/Electrolyte Interfaces in High Voltage Li-Ion Cells, J. Electrochem. Soc. 163 (2016) A1001–A1009. https://doi.org/10.1149/2.1051606jes.

[67] Z.A. Needell, J. McNerney, M.T. Chang, J.E. Trancik, Potential for widespread electrification of personal vehicle travel in the United States, Nat. Energy. 1 (2016). https://doi.org/10.1038/nenergy.2016.112.

[68] S. Ahmed, I. Bloom, A.N. Jansen, T. Tanim, E.J. Dufek, A. Pesaran, A. Burnham, R.B. Carlson, F. Dias, K. Hardy, Enabling fast charging–A battery technology gap assessment, J. Power Sources. 367 (2017) 250–262.

[69] Q. Liu, C. Du, B. Shen, P. Zuo, X. Cheng, Y. Ma, G. Yin, Y. Gao, Understanding undesirable anode lithium plating issues in lithium-ion batteries, RSC Adv. 6 (2016) 88683–88700. https://doi.org/10.1039/c6ra19482f.

[70] T. Waldmann, B.-I. Hogg, M. Wohlfahrt-Mehrens, Li plating as unwanted side reaction in commercial Li-ion cells–A review, J. Power Sources. 384 (2018) 107–124.

[71] C. Pastor-Fernández, K. Uddin, G.H. Chouchelamane, W.D. Widanage, J. Marco, A Comparison between Electrochemical Impedance Spectroscopy and Incremental Capacity-Differential Voltage as Li-ion Diagnostic Techniques to Identify and Quantify the Effects of Degradation Modes within Battery Management Systems, J. Power Sources. 360 (2017) 301–318. https://doi.org/10.1016/j.jpowsour.2017.03.042.

[72] J. Liu, Q. Duan, M. Ma, C. Zhao, J. Sun, Q. Wang, Aging mechanisms and thermal stability of aged commercial 18650 lithium ion battery induced by slight overcharging cycling, J. Power Sources. 445 (2020) 227263. https://doi.org/10.1016/j.jpowsour.2019.227263.

[73] Y. Gao, J. Jiang, C. Zhang, W. Zhang, Z. Ma, Y. Jiang, Lithium-ion battery aging mechanisms and life model under different charging stresses, J. Power Sources. 356 (2017) 103–114.

[74] J.C. Burns, D.A. Stevens, J.R. Dahn, In-Situ Detection of Lithium Plating Using High Precision Coulometry, J. Electrochem. Soc. 162 (2015) A959–A964. https://doi.org/10.1149/2.0621506jes.

[75] C. Uhlmann, J. Illig, M. Ender, R. Schuster, E. Ivers-Tiffée, In situ detection of lithium metal plating on graphite in experimental cells, J. Power Sources. (2015). https://doi.org/10.1016/j.jpowsour.2015.01.046.

[76] S.S. Zhang, K. Xu, T.R. Jow, Study of the charging process of a LiCoO2-based Li-ion battery, J. Power Sources. 160 (2006) 1349–1354. https://doi.org/10.1016/j.jpowsour.2006.02.087.

[77] K.G. Gallagher, S.E. Trask, C. Bauer, T. Woehrle, S.F. Lux, M. Tschech, P. Lamp, B.J. Polzin, S. Ha, B. Long, Optimizing areal capacities through understanding the limitations of lithium-ion electrodes, J. Electrochem. Soc. 163 (2015) A138.

[78] A.J. Smith, J.C. Burns, D. Xiong, J.R. Dahn, Interpreting High Precision Coulometry Results on Li-ion Cells, J. Electrochem. Soc. 158 (2011) A1136. https://doi.org/10.1149/1.3625232.

[79] D. Aurbach, E. Zinigrad, H. Teller, P. Dan, Factors Which Limit the Cycle Life of Rechargeable Lithium (Metal) Batteries, J. Electrochem. Soc. 147 (2000) 1274. https://doi.org/10.1149/1.1393349.

[80] F. Ding, W. Xu, X. Chen, J. Zhang, M.H. Engelhard, Y. Zhang, B.R. Johnson, J. V. Crum, T.A. Blake, X. Liu, J.-G. Zhang, Effects of Carbonate Solvents and Lithium Salts on Morphology and Coulombic Efficiency of Lithium Electrode, J. Electrochem. Soc. 160 (2013) A1894–A1901. https://doi.org/10.1149/2.100310jes.

[81] R. Weber, M. Genovese, A.J. Louli, S. Hames, C. Martin, I.G. Hill, J.R. Dahn, Long cycle life and dendrite-free lithium morphology in anode-free lithium pouch cells enabled by a dual-salt liquid electrolyte, Nat. Energy. 4 (2019) 683–689. https://doi.org/10.1038/s41560-019-0428-9.

[82] M. Broussely, P. Biensan, F. Bonhomme, P. Blanchard, S. Herreyre, K. Nechev, R.J. Staniewicz, Main aging mechanisms in Li ion batteries, J. Power Sources. 146 (2005) 90–96. https://doi.org/10.1016/j.jpowsour.2005.03.172.

[83] Z. Li, J. Huang, B. Yann Liaw, V. Metzler, J. Zhang, A review of lithium deposition in lithium-ion and lithium metal secondary batteries, J. Power Sources. 254 (2014) 168–182. https://doi.org/10.1016/j.jpowsour.2013.12.099.

[84] X. Zhu, Z. Wang, C. Wang, L. Huang, Overcharge investigation of large format lithium-ion pouch cells with Li (Ni0. 6Co0. 2Mn0. 2) O2 cathode for electric vehicles: degradation and failure mechanisms, J. Electrochem. Soc. 165 (2018) A3613.

[85] X. Zhu, H. Wang, S. Allu, Y. Gao, E. Cakmak, E.J. Hopkins, G.M. Veith, Z. Wang, Investigation on capacity loss mechanisms of lithium-ion pouch cells under mechanical indentation conditions, J. Power Sources. 465 (2020) 228314. https://doi.org/10.1016/j.jpowsour.2020.228314.

[86] S. Huang, X. Wu, G.M. Cavalheiro, X. Du, B. Liu, Z. Du, G. Zhang, In Situ Measurement of Lithium-Ion Cell Internal Temperatures during Extreme Fast Charging, J. Electrochem. Soc. 166 (2019) A3254–A3259. https://doi.org/10.1149/2.0441914jes.

[87] X.G. Yang, G. Zhang, S. Ge, C.Y. Wang, Fast charging of lithium-ion batteries at all temperatures, Proc. Natl. Acad. Sci. U. S. A. 115 (2018) 7266–7271. https://doi.org/10.1073/pnas.1807115115.

[88] J. Vetter, P. Novák, M.R. Wagner, C. Veit, K.-C. Möller, J.O. Besenhard, M. Winter, M. Wohlfahrt-Mehrens, C. Vogler, A. Hammouche, Ageing mechanisms in lithium-ion batteries, J. Power Sources. 147 (2005) 269–281. https://doi.org/10.1016/j.jpowsour.2005.01.006.

[89] T. Waldmann, M. Wilka, M. Kasper, M. Fleischhammer, M. Wohlfahrt-Mehrens, Temperature dependent ageing mechanisms in Lithium-ion batteries – A Post-Mortem study, J. Power Sources. 262 (2014) 129–135. https://doi.org/10.1016/j.jpowsour.2014.03.112.

[90] J. Neuefeind, M. Feygenson, J. Carruth, R. Hoffmann, K.K. Chipley, The Nanoscale Ordered MAterials Diffractometer NOMAD at the Spallation Neutron Source SNS, Nucl. Instruments Methods Phys. Res. Sect. B Beam Interact. with Mater. Atoms. 287 (2012) 68–75. https://doi.org/10.1016/j.nimb.2012.05.037.

[91] A.A. Coelho, P.A. Chater, A. Kern, Fast synthesis and refinement of the atomic pair distribution function, J. Appl. Crystallogr. 48 (2015) 869–875. https://doi.org/10.1107/S1600576715007487.

[92] J. Self, C.P. Aiken, R. Petibon, J.R. Dahn, Survey of Gas Expansion in Li-Ion NMC Pouch Cells, J. Electrochem. Soc. 162 (2015) A796–A802. https://doi.org/10.1149/2.0081506jes.

[93] L.M. Thompson, W. Stone, A. Eldesoky, N.K. Smith, C.R.M. McFarlane, J.S. Kim, M.B. Johnson, R. Petibon, J.R. Dahn, Quantifying Changes to the Electrolyte and Negative Electrode in Aged NMC532/Graphite Lithium-Ion Cells, J. Electrochem. Soc. 165 (2018) A2732–A2740. https://doi.org/10.1149/2.0721811jes.

[94] Z. Du, D.L. Wood, C. Daniel, S. Kalnaus, J. Li, Understanding limiting factors in thick electrode performance as applied to high energy density Li-ion batteries, J. Appl. Electrochem. 47 (2017) 405–415. https://doi.org/10.1007/s10800-017-1047-4.

[95] Q.Q. Liu, R. Petibon, C.Y. Du, J.R. Dahn, Effects of Electrolyte Additives and Solvents on Unwanted Lithium Plating in Lithium-Ion Cells, J. Electrochem. Soc. 164 (2017) A1173–A1183. https://doi.org/10.1149/2.1081706jes.

[96] S.S. Choi, H.S. Lim, Factors that affect cycle-life and possible degradation mechanisms of a Li-ion cell based on LiCoO2, J. Power Sources. 111 (2002) 130–136. https://doi.org/10.1016/S0378-7753(02)00305-1.

[97] J.C. Burns, N.N. Sinha, D.J. Coyle, G. Jain, C.M. VanElzen, W.M. Lamanna, A. Xiao, E. Scott, J.P. Gardner, J.R. Dahn, The Impact of Varying the Concentration of Vinylene Carbonate Electrolyte Additive in Wound Li-Ion Cells, J. Electrochem. Soc. 159 (2011) A85–A90. https://doi.org/10.1149/2.028202jes.

[98] A.S. Mussa, A. Liivat, F. Marzano, M. Klett, B. Philippe, C. Tengstedt, G. Lindbergh, K. Edström, R.W. Lindström, P. Svens, Fast-charging effects on ageing for energy-optimized automotive LiNi1/3Mn1/3Co1/3O2/graphite prismatic lithium-ion cells, J. Power Sources. 422 (2019) 175–184. https://doi.org/https://doi.org/10.1016/j.jpowsour.2019.02.095.

[99] S.S. Zhang, Unveiling Capacity Degradation Mechanism of Li-ion Battery in Fast-charging Process, ChemElectroChem. 7 (2020) 555–560. https://doi.org/10.1002/celc.201902050.

[100] K. Kumai, H. Miyashiro, Y. Kobayashi, K. Takei, R. Ishikawa, Gas generation mechanism due to electrolyte decomposition in commercial lithium-ion cell, J. Power Sources. (1999). https://doi.org/10.1016/S0378-7753(98)00234-1.

[101] X. Teng, C. Zhan, Y. Bai, L. Ma, Q. Liu, C. Wu, F. Wu, Y. Yang, J. Lu, K. Amine, In Situ Analysis of Gas Generation in Lithium-Ion Batteries with Different Carbonate-Based Electrolytes, ACS Appl. Mater. Interfaces. (2015). https://doi.org/10.1021/acsami.5b08399.

[102] N.E. Galushkin, N.N. Yazvinskaya, D.N. Galushkin, Mechanism of Gases Generation during Lithium-Ion Batteries Cycling, J. Electrochem. Soc. 166 (2019) A897–A908. https://doi.org/10.1149/2.0041906jes.

[103] D.J. Xiong, L.D. Ellis, R. Petibon, T. Hynes, Q.Q. Liu, J.R. Dahn, Studies of Gas Generation, Gas Consumption and Impedance Growth in Li-Ion Cells with Carbonate or Fluorinated Electrolytes Using the Pouch Bag Method, J. Electrochem. Soc. 164 (2016) A340–A347. https://doi.org/10.1149/2.1091702jes.

[104] L.D. Ellis, J.P. Allen, L.M. Thompson, J.E. Harlow, W.J. Stone, I.G. Hill, J.R. Dahn, Quantifying, Understanding and Evaluating the Effects of Gas Consumption in Lithium-Ion Cells, J. Electrochem. Soc. 164 (2017) A3518–A3528. https://doi.org/10.1149/2.0191714jes.

[105] C. Mao, R.E. Ruther, L. Geng, Z. Li, D.N. Leonard, H.M. Meyer, R.L. Sacci, D.L. Wood, Evaluation of Gas Formation and Consumption Driven by Crossover Effect in High-Voltage Lithium-Ion Batteries with Ni-Rich NMC Cathodes, ACS Appl. Mater. Interfaces. 11 (2019) 43235–43243. https://doi.org/10.1021/acsami.9b15916.

[106] H. Yoshida, T. Fukunaga, T. Hazama, M. Terasaki, M. Mizutani, M. Yamachi, Degradation mechanism of alkyl carbonate solvents used in lithium-ion cells during initial charging, J. Power Sources. 68 (1997) 311–315. https://doi.org/10.1016/S0378-7753(97)02635-9.

[107] H. Kim, S. Grugeon, G. Gachot, M. Armand, L. Sannier, S. Laruelle, Ethylene bis-carbonates as telltales of SEI and electrolyte health, role of carbonate type and new additives, Electrochim. Acta. 136 (2014) 157–165.

[108] X. Zeng, M. Li, D. Abd El-Hady, W. Alshitari, A.S. Al-Bogami, J. Lu, K. Amine, Commercialization of Lithium Battery Technologies for Electric Vehicles, Adv. Energy Mater. (2019). https://doi.org/10.1002/aenm.201900161.

[109] X.G. Yang, C.Y. Wang, Understanding the trilemma of fast charging, energy density and cycle life of lithium-ion batteries, J. Power Sources. 402 (2018) 489–498. https://doi.org/10.1016/J.JPOWSOUR.2018.09.069.

[110] X. Wu, T. Liu, Y. Bai, X. Feng, M.M. Rahman, C.J. Sun, F. Lin, K. Zhao, Z. Du, Effects of solvent formulations in electrolytes on fast charging of Li-ion cells, Electrochim. Acta. 353 (2020) 136453. https://doi.org/10.1016/J.ELECTACTA.2020.136453.

[111] X. Wu, Y. Bai, Z. Li, J. Liu, K. Zhao, Z. Du, Effects of charging rates on LiNi0.6Mn0.2Co0.2O2 (NMC622)/graphite Li-ion cells, J. Energy Chem. 56 (2021) 121–126. https://doi.org/10.1016/J.JECHEM.2020.08.008.

[112] X.G. Yang, T. Liu, Y. Gao, S. Ge, Y. Leng, D. Wang, C.Y. Wang, Asymmetric Temperature Modulation for Extreme Fast Charging of Lithium-Ion Batteries, Joule. 3 (2019) 3002–3019. https://doi.org/10.1016/J.JOULE.2019.09.021.

[113] K.H. Chen, M.J. Namkoong, V. Goel, C. Yang, S. Kazemiabnavi, S.M. Mortuza, E. Kazyak, J. Mazumder, K. Thornton, J. Sakamoto, N.P. Dasgupta, Efficient fast-charging of lithium-ion batteries enabled by laser-patterned three-dimensional graphite anode architectures, J. Power Sources. 471 (2020) 228475. https://doi.org/10.1016/J.JPOWSOUR.2020.228475.

[114] E.R. Logan, J.R. Dahn, Electrolyte Design for Fast-Charging Li-Ion Batteries, Trends Chem. 2 (2020) 354–366. https://doi.org/10.1016/J.TRECHM.2020.01.011.

[115] Y. Li, Y. Lu, P. Adelhelm, M.-M. Titirici, Y.-S. Hu, Intercalation chemistry of graphite: alkali metal ions and beyond, Chem. Soc. Rev. 48 (2019) 4655–4687. https://doi.org/10.1039/C9CS00162J.

[116] N. Daumas, A. Herold, Relations between phase concept and reaction mechanics in graphite insertion compounds, Comptes Rendus Hebd. Des Seances L Acad. Des Sci. Ser. C. 268 (1969) 373.

[117] T.R. Ferguson, M.Z. Bazant, Nonequilibrium Thermodynamics of Porous Electrodes, J. Electrochem. Soc. 159 (2012) A1967–A1985. https://doi.org/10.1149/2.048212jes.

[118] J.W. Cahn, J.E. Hilliard, Free Energy of a Nonuniform System. I. Interfacial Free Energy, J. Chem. Phys. 28 (1958) 258–267. https://doi.org/10.1063/1.1744102.

[119] C.J. Wen, R.A. Huggins, Thermodynamic and mass transport properties of "LiAl," J. Electrochem. Soc. 126 (1979) 1225–1234. https://doi.org/10.1016/0025-5408(80)90024-0.

[120] C. Ho, Application of A-C Techniques to the Study of Lithium Diffusion in Tungsten Trioxide Thin Films, J. Electrochem. Soc. 127 (1980) 343. https://doi.org/10.1149/1.2129668.

[121] C.J. Wen, C. Ho, B.A. Boukamp, I.D. Raistrick, W. Weppner, R.A. Huggins, Use of electrochemical methods to determine chemical-diffusion coefficients in alloys: application to 'LiAI,' Int. Mater. Rev. 26 (1981) 253–268. https://doi.org/10.1179/095066081790149195.

[122] M.D. Levi, E. Markevich, D. Aurbach, Comparison between Cottrell diffusion and moving boundary models for determination of the chemical diffusion coefficients in ion-insertion electrodes, Electrochim. Acta. 51 (2005) 98–110. https://doi.org/10.1016/j.electacta.2005.04.007.

[123] Y. Zhu, C. Wang, Galvanostatic intermittent titration technique for phase-transformation electrodes, J. Phys. Chem. C. 114 (2010) 2830–2841. https://doi.org/10.1021/jp9113333.

[124] J. Li, X. Xiao, F. Yang, M.W. Verbrugge, Y.T. Cheng, Potentiostatic intermittent titration technique for electrodes governed by diffusion and interfacial reaction, J. Phys. Chem. C. 116 (2012) 1472–1478. https://doi.org/10.1021/jp207919q.

[125] S.J. Harris, A. Timmons, D.R. Baker, C. Monroe, Direct in situ measurements of Li transport in Li-ion battery negative electrodes, Chem. Phys. Lett. 485 (2010) 265–274. https://doi.org/10.1016/j.cplett.2009.12.033.

[126] P. Maire, H. Kaiser, W. Scheifele, P. Novák, Colorimetric determination of lithium-ion mobility in graphite composite electrodes, J. Electroanal. Chem. 644 (2010) 127–131. https://doi.org/10.1016/j.jelechem.2009.09.011.

[127] Y. Guo, R.B. Smith, Z. Yu, D.K. Efetov, J. Wang, P. Kim, M.Z. Bazant, L.E. Brus, Li Intercalation into Graphite: Direct Optical Imaging and Cahn-Hilliard Reaction Dynamics, J. Phys. Chem. Lett. 7 (2016) 2151–2156. https://doi.org/10.1021/acs.jpclett.6b00625.

[128] K.E. Thomas-Alyea, C. Jung, R.B. Smith, M.Z. Bazant, In Situ Observation and Mathematical Modeling of Lithium Distribution within Graphite, J. Electrochem. Soc. 164 (2017) E3063–E3072. https://doi.org/10.1149/2.0061711jes.

[129] B. Shi, Y. Kang, H. Xie, H. Song, Q. Zhang, In situ measurement and experimental analysis of lithium mass transport in graphite electrodes, Electrochim. Acta. 284 (2018) 142–148. https://doi.org/10.1016/j.electacta.2018.07.079.

[130] G.L. Doll, P.C. Eklund, J.E. Fischer, Raman scattering study of the high-frequency graphitic intralayer modes in Li-graphite and the stage dependence of the mode frequency in donor graphite intercalation compounds, Phys. Rev. B. 36 (1987) 4940–4945. https://doi.org/10.1103/PhysRevB.36.4940.

[131] M. Inaba, In Situ Raman Study on Electrochemical Li Intercalation into Graphite, J. Electrochem. Soc. 142 (1995) 20. https://doi.org/10.1149/1.2043869.

[132] Y. Luo, W.-B. Cai, D.A. Scherson, In Situ, Real-Time Raman Microscopy of Embedded Single Particle Graphite Electrodes, J. Electrochem. Soc. 149 (2002) A1100. https://doi.org/10.1149/1.1492286.

[133] Q. Shi, K. Dokko, D.A. Scherson, In Situ Raman Microscopy of a Single Graphite Microflake Electrode in a Li+-Containing Electrolyte, J. Phys. Chem. B. 108 (2004) 4789–4793. https://doi.org/10.1021/jp037015e.

[134] S. Migge, G. Sandmann, D. Rahner, H. Dietz, W. Plieth, Studying lithium intercalation into graphite particles via in situ Raman spectroscopy and confocal microscopy, J. Solid State Electrochem. 9 (2005) 132–137. https://doi.org/10.1007/s10008-004-0563-4.

[135] C. Sole, N.E. Drewett, L.J. Hardwick, Insitu Raman study of lithium-ion intercalation into microcrystalline graphite, Faraday Discuss. 172 (2014) 223–237. https://doi.org/10.1039/c4fd00079j.

[136] H. Song, T. Fukutsuka, T. Abe, In situ Raman investigation of electrolyte solutions in the vicinity of graphite negative electrodes, (2016) 27486–27492. https://doi.org/10.1039/c6cp05489g.

[137] U. Boesenberg, D. Sokaras, D. Nordlund, T.C. Weng, E. Gorelov, T.J. Richardson, R. Kostecki, J. Cabana, Electronic structure changes upon lithium intercalation into graphite – Insights from ex situ and operando x-ray Raman spectroscopy, Carbon N. Y. 143 (2019) 371–377. https://doi.org/10.1016/J.CARBON.2018.11.031.

[138] A.M. Dimiev, K. Shukhina, N. Behabtu, M. Pasquali, J.M. Tour, Stage Transitions in Graphite Intercalation Compounds: Role of the Graphite Structure, J. Phys. Chem. C. 123 (2019) 19246–19253. https://doi.org/10.1021/acs.jpcc.9b06726.

[139] A. Schirmer, P. Heitjans, Diffusive Motion in Stage-1 and Stage-2 Li-Graphite Intercalation Compounds: Results of ß-NMR and Quasielastic Neutron Scattering, Zeitschrift Für Naturforsch. A. 50 (1995) 643–652. https://doi.org/10.1515/zna-1995-0704.

[140] M. Letellier, F. Chevallier, In situ 7Li NMR during lithium electrochemical insertion into graphite and a carbon/carbon composite, J. Phys. Chem. Solids. 7 (2006) 1228–1232. https://doi.org/10.1016/j.crci.2003.11.010.

[141] H. He, C. Huang, C.-W. Luo, J.-J. Liu, Z.-S. Chao, Dynamic study of Li intercalation into graphite by in situ high energy synchrotron XRD, Electrochim. Acta. 92 (2013) 148–152. https://doi.org/https://doi.org/10.1016/j.electacta.2012.12.135.

[142] J.K. Mathiesen, R.E. Johnsen, A.S. Blennow, P. Norby, Understanding the structural changes in lithiated graphite through high-resolution operando powder X-ray diffraction, Carbon N. Y. 153 (2019) 347–354. https://doi.org/10.1016/J.CARBON.2019.06.103.

[143] M. Morcrette, Y. Chabre, G. Vaughan, G. Amatucci, J.B. Leriche, S. Patoux, C. Masquelier, J.M. Tarascon, In situ X-ray diffraction techniques as a powerful tool to study battery electrode materials, Electrochim. Acta. 47 (2002) 3137–3149. https://doi.org/10.1016/S0013-4686(02)00233-5.

[144] M. Bianchini, J.B. Leriche, J.-L. Laborier, L. Gendrin, E. Suard, L. Croguennec, C. Masquelier, A New Null Matrix Electrochemical Cell for Rietveld Refinements of In-Situ or Operando Neutron Powder Diffraction Data, J. Electrochem. Soc. 160 (2013) A2176–A2183. https://doi.org/10.1149/2.076311jes.

[145] Y. Orikasa, T. Maeda, Y. Koyama, H. Murayama, K. Fukuda, H. Tanida, H. Arai, E. Matsubara, Y. Uchimoto, Z. Ogumi, Transient phase change in two phase reaction between LiFePO4 and FePO4 under battery operation, Chem. Mater. 25 (2013) 1032–1039. https://doi.org/10.1021/cm303411t.

[146] Y. Shen, E.E. Pedersen, M. Christensen, B.B. Iversen, An electrochemical cell for in operando studies of lithium/sodium batteries using a conventional x-ray powder diffractometer, Rev. Sci. Instrum. 85 (2014) 104103. https://doi.org/10.1063/1.4896198.

[147] L. Boulet-Roblin, P. Borel, D. Sheptyakov, C. Tessier, P. Novák, C. Villevieille, Operando Neutron Powder Diffraction Using Cylindrical Cell Design: The Case of LiNi0.5Mn1.5O4 vs Graphite, J. Phys. Chem. C. 120 (2016) 17268–17273. https://doi.org/10.1021/acs.jpcc.6b05777.

[148] S.-M. Bak, Z. Shadike, R. Lin, X. Yu, X.-Q. Yang, In situ/operando synchrotron-based X-ray techniques for lithium-ion battery research, NPG Asia Mater. 10 (2018) 563–580. https://doi.org/10.1038/s41427-018-0056-z.

[149] K.P.C. Yao, J.S. Okasinski, K. Kalaga, I.A. Shkrob, D.P. Abraham, Quantifying lithium concentration gradients in the graphite electrode of Li-ion cells using: Operando energy dispersive X-ray diffraction, Energy Environ. Sci. 12 (2019) 656–665. https://doi.org/10.1039/c8ee02373e.

[150] D.P. Finegan, A. Quinn, D.S. Wragg, A.M. Colclasure, X. Lu, C. Tan, T.M.M. Heenan, R. Jervis, D.J.L. Brett, S. Das, T. Gao, D.A. Cogswell, M.Z. Bazant, M. Di Michiel, S. Checchia, P.R. Shearing, K. Smith, Spatial dynamics of lithiation and lithium plating during high-rate operation of graphite electrodes, Energy Environ. Sci. 13 (2020) 2570–2584. https://doi.org/10.1039/D0EE01191F.

[151] Ö. Bergstöm, A.M. Andersson, K. Edström, T. Gustafsson, A neutron diffraction cell for studying lithium-insertion processes in electrode materials, J. Appl. Crystallogr. 31 (1998) 823–825. https://doi.org/10.1107/S002188989800538X.

[152] H. Berg, J.O. Thomas, Neutron diffraction study of electrochemically delithiated LiMn2O4 spinel, Solid State Ionics. 126 (1999) 227–234. https://doi.org/10.1016/S0167-2738(99)00235-0.

[153] M.A. Rodriguez, D. Ingersoll, S.C. Vogel, D.J. Williams, Simultaneous in Situ Neutron Diffraction Studies of the Anode and Cathode in a Lithium-Ion Cell, Electrochem. Solid-State Lett. 7 (2004) 2003–2005. https://doi.org/10.1149/1.1628664.

[154] M.A. Rodriguez, M.H. Van Benthem, D. Ingersoll, S.C. Vogel, H.M. Reiche, In situ analysis of LiFePO 4 batteries: Signal extraction by multivariate analysis , Powder Diffr. 25 (2010) 143–148. https://doi.org/10.1154/1.3393786.

[155] A. Aatiq, M. Ménétrier, L. Croguennec, E. Suard, C. Delmas, On the structure of Li3Ti2(Po4)3, J. Mater. Chem. 12 (2002) 2971–2978. https://doi.org/10.1039/b203652p.

[156] L. Croguennec, E. Suard, P. Willmann, C. Delmas, Structural and electrochemical characterization of the LiNi1-yTiyO2 electrode materials obtained by direct solid-state reactions, Chem. Mater. 14 (2002) 2149–2157. https://doi.org/10.1021/cm011265v.

[157] A.O. Kondrakov, H. Geßwein, K. Galdina, L. De Biasi, V. Meded, E.O. Filatova, G. Schumacher, W. Wenzel, P. Hartmann, T. Brezesinski, J. Janek, Charge-transfer-induced lattice collapse in Ni-rich NCM cathode materials during delithiation, J. Phys. Chem. C. 121 (2017) 24381–24388. https://doi.org/10.1021/acs.jpcc.7b06598.

[158] Y. Ren, X. Zuo, Synchrotron X-Ray and Neutron Diffraction, Total Scattering, and Small-Angle Scattering Techniques for Rechargeable Battery Research, Small Methods. 2 (2018) 1800064. https://doi.org/10.1002/smtd.201800064.

[159] N. Sharma, V.K. Peterson, Overcharging a lithium-ion battery: Effect on the LixC 6 negative electrode determined by in situ neutron diffraction, J. Power Sources. 244 (2013) 695–701. https://doi.org/10.1016/j.jpowsour.2012.12.019.

[160] L. Vitoux, M. Reichardt, S. Sallard, P. Novák, D. Sheptyakov, C. Villevieille, A cylindrical cell for operando neutron diffraction of Li-ion battery electrode materials, Front. Energy Res. 6 (2018) 1–16. https://doi.org/10.3389/fenrg.2018.00076.

[161] J. Wilhelm, S. Seidlmayer, S. Erhard, M. Hofmann, R. Gilles, A. Jossen, In Situ Neutron Diffraction Study of Lithiation Gradients in Graphite Anodes during Discharge and Relaxation, J. Electrochem. Soc. 165 (2018) A1846–A1856. https://doi.org/10.1149/2.1231809jes.

[162] W.K. Pang, V.K. Peterson, A custom battery for operando neutron powder diffraction studies of electrode structure, J. Appl. Crystallogr. 48 (2015) 280–290. https://doi.org/10.1107/S1600576715000679.

[163] G. Liang, C. Didier, Z. Guo, W.K. Pang, V.K. Peterson, Understanding Rechargeable Battery Function Using In Operando Neutron Powder Diffraction, Adv. Mater. 32 (2020) 1–12. https://doi.org/10.1002/adma.201904528.

[164] S. Ikeda, J.M. Carpenter, Wide-energy-range, high-resolution measurements of neutron pulse shapes of polyethylene moderators, Nucl. Inst. Methods Phys. Res. A. 239 (1985) 536–544. https://doi.org/10.1016/0168-9002(85)90033-6.

[165] A.C.L. R.B.V.D, GSAS, 1994.

[166] R.A. Young, The Rietveld method Oxford Univ, Press, 1995.

[167] L. Lobanov, N. N. A. d. V., No Title, in: 6th Eur. Powder Diffr. Con-Ference, Budapest, Hungary, 1988: p. Abstract P12-16.

[168] H.M. Rietveld, A profile refinement method for nuclear and magnetic structures, J. Appl. Crystallogr. 2 (1969) 65–71. https://doi.org/10.1107/s0021889869006558.

[169] A.A. Coelho, TOPAS and TOPAS-Academic: An optimization program integrating computer algebra and crystallographic objects written in C++, J. Appl. Crystallogr. 51 (2018) 210–218. https://doi.org/10.1107/S1600576718000183.

[170] J.R. Dahn, Phase diagram of LixC6, Phys. Rev. B. 44 (1991) 9170–9177. https://doi.org/10.1103/PhysRevB.44.9170.

[171] S.A. Safran, Cooperative effects and staging n graphite intercalation compounds, Synth. Met. 2 (1980) 1–15. https://doi.org/10.1016/0379-6779(80)90026-0.

[172] D. Billaud, F.X. Henry, M. Lelaurain, P. Willmann, Revisited structures of dense and dilute stage II lithium-graphite intercalation compounds, J. Phys. Chem. Solids. 57 (1996) 775–781. https://doi.org/10.1016/0022-3697(95)00348-7.

[173] A. Missyul, I. Bolshakov, R. Shpanchenko, XRD study of phase transformations in lithiated graphite anodes by Rietveld method, Powder Diffr. 32 (2017) S56–S62. https://doi.org/DOI: 10.1017/S0885715617000458.

[174] W.S. Yoon, M. Balasubramanian, K.Y. Chung, X.Q. Yang, J. McBreen, C.P. Grey, D.A. Fischer, Investigation of the charge compensation mechanism on the electrochemically Li-ion deintercalated Li1-xCo1/3Ni1/3Mn 1/3O2 electrode system by combination of soft and hard X-ray absorption spectroscopy, J. Am. Chem. Soc. 127 (2005) 17479–17487. https://doi.org/10.1021/ja0530568.

[175] W. Lee, S. Muhammad, T. Kim, H. Kim, E. Lee, M. Jeong, S. Son, J.H. Ryou, W.S. Yoon, New Insight into Ni-Rich Layered Structure for Next-Generation Li Rechargeable Batteries, Adv. Energy Mater. 8 (2018) 1–12. https://doi.org/10.1002/aenm.201701788.

[176] C. Tian, D. Nordlund, H.L. Xin, Y. Xu, Y. Liu, D. Sokaras, F. Lin, M.M. Doeff, Depth-Dependent Redox Behavior of LiNi 0.6 Mn 0.2 Co 0.2 O 2 , J. Electrochem. Soc. 165 (2018) A696–A704. https://doi.org/10.1149/2.1021803jes.

[177] K. Min, K. Kim, C. Jung, S.W. Seo, Y.Y. Song, H.S. Lee, J. Shin, E. Cho, A comparative study of structural changes in lithium nickel cobalt manganese oxide as a function of Ni content during delithiation process, J. Power Sources. 315 (2016) 111–119. https://doi.org/10.1016/j.jpowsour.2016.03.017.

[178] I.A. Bobrikov, N.Y. Samoylova, S. V. Sumnikov, O.Y. Ivanshina, R.N. Vasin, A.I. Beskrovnyi, A.M. Balagurov, In-situ time-of-flight neutron diffraction study of the structure evolution of electrode materials in a commercial battery with LiNi0.8Co0.15Al0.05O2 cathode, J. Power Sources. 372 (2017) 74–81. https://doi.org/10.1016/j.jpowsour.2017.10.052.

[179] K. Märker, P.J. Reeves, C. Xu, K.J. Griffith, C.P. Grey, Evolution of Structure and Lithium Dynamics in LiNi 0.8 Mn 0.1 Co 0.1 O 2 (NMC811) Cathodes during Electrochemical Cycling, Chem. Mater. 31 (2019) 2545–2554. https://doi.org/10.1021/acs.chemmater.9b00140.

[180] C. Hong, Q. Leng, J. Zhu, S. Zheng, H. He, Y. Li, R. Liu, J. Wan, Y. Yang, Revealing the correlation between structural evolution and Li+diffusion kinetics of nickel-rich cathode materials in Li-ion batteries, J. Mater. Chem. A. 8 (2020) 8540–8547. https://doi.org/10.1039/d0ta00555j.

[181] J. Kasnatscheew, M. Evertz, B. Streipert, R. Wagner, R. Klöpsch, B. Vortmann, H. Hahn, S. Nowak, M. Amereller, A.C. Gentschev, P. Lamp, M. Winter, The truth about the 1st cycle Coulombic efficiency of LiNi1/3Co1/3Mn1/3O2 (NCM) cathodes, Phys. Chem. Chem. Phys. 18 (2016) 3956–3965. https://doi.org/10.1039/c5cp07718d.

[182] J. Li, J. Harlow, N. Stakheiko, N. Zhang, J. Paulsen, J. Dahn, Dependence of Cell Failure on Cut-Off Voltage Ranges and Observation of Kinetic Hindrance in LiNi 0.8 Co 0.15 Al 0.05 O 2 , J. Electrochem. Soc. 165 (2018) A2682–A2695. https://doi.org/10.1149/2.0491811jes.

[183] S.L. Wu, W. Zhang, X. Song, A.K. Shukla, G. Liu, V. Battaglia, V. Srinivasan, High rate capability of Li(Ni 13Mn 13Co 13)O 2 electrode for Li-ion batteries, J. Electrochem. Soc. 159 (2012) 438–444. https://doi.org/10.1149/2.062204jes.

[184] W. Hu, C. Zhang, H. Jiang, M. Zheng, Q.H. Wu, Q. Dong, Improving the electrochemistry performance of layer LiNi0.5Mn0.3Co0.2O2 material at 4.5 V cutoff potential using lithium metaborate, Electrochim. Acta. 243 (2017) 105–111. https://doi.org/10.1016/j.electacta.2017.05.075.

[185] B. Luo, B. Jiang, P. Peng, J.J. Huang, J. Chen, M. Li, L. Chu, Y. Li, Improving the electrochemical performance of LiNi1/3Co1/3Mn1/3O2 cathode material via tungsten modification, Electrochim. Acta. 297 (2019) 398–405. https://doi.org/10.1016/j.electacta.2018.11.202.

[186] M.D. Radin, S. Hy, M. Sina, C. Fang, H. Liu, J. Vinckeviciute, M. Zhang, M.S. Whittingham, Y.S. Meng, A. Van der Ven, Narrowing the Gap between Theoretical and Practical Capacities in Li-Ion Layered Oxide Cathode Materials, Adv. Energy Mater. 7 (2017) 1–33. https://doi.org/10.1002/aenm.201602888.

[187] V.J. Ovejas, A. Cuadras, State of charge dependency of the overvoltage generated in commercial Li-ion cells, J. Power Sources. 418 (2019) 176–185. https://doi.org/10.1016/j.jpowsour.2019.02.046.

[188] M.E. Ferraro, B.L. Trembacki, V.E. Brunini, D.R. Noble, S.A. Roberts, Electrode Mesoscale as a Collection of Particles: Coupled Electrochemical and Mechanical Analysis of NMC Cathodes, J. Electrochem. Soc. 167 (2020) 013543. https://doi.org/10.1149/1945-7111/ab632b.

[189] B. Vadlamani, K. An, M. Jagannathan, K.S.R. Chandran, An In-Situ Electrochemical Cell for Neutron Diffraction Studies of Phase Transitions in Small Volume Electrodes of Li-Ion Batteries, J. Electrochem. Soc. 161 (2014) A1731–A1741. https://doi.org/10.1149/2.0951410jes.

[190] D.W. Dees, M.-T.F. Rodrigues, K. Kalaga, S.E. Trask, I.A. Shkrob, D.P. Abraham, A.N. Jansen, Apparent Increasing Lithium Diffusion Coefficient with Applied Current in Graphite, J. Electrochem. Soc. 167 (2020) 120528. https://doi.org/10.1149/1945-7111/abaf9f.

[191] J.L. Allen, T. Richard Jow, J. Wolfenstine, Kinetic study of the electrochemical FePO4 to LiFePO4 phase transition, Chem. Mater. 19 (2007) 2108–2111. https://doi.org/10.1021/cm062963o.

[192] K.G. Gallagher, D.W. Dees, A.N. Jansen, D.P. Abraham, S.-H. Kang, A Volume Averaged Approach to the Numerical Modeling of Phase-Transition Intercalation Electrodes Presented for Li x C 6 , J. Electrochem. Soc. 159 (2012) A2029–A2037. https://doi.org/10.1149/2.015301jes.

[193] K. Xiang, K. Yang, W.C. Carter, M. Tang, Y.-M. Chiang, Mesoscopic Phase Transition Kinetics in Secondary Particles of Electrode-Active Materials in Lithium-Ion Batteries, Chem. Mater. 30 (2018) 4216–4225. https://doi.org/10.1021/acs.chemmater.7b05407.

[194] R.B. Smith, E. Khoo, M.Z. Bazant, Intercalation Kinetics in Multiphase-Layered Materials, J. Phys. Chem. C. 121 (2017) 12505–12523. https://doi.org/10.1021/acs.jpcc.7b00185.

[195] S. Ranganathan, M. Von Heimendahl, The three activation energies with isothermal transformations: applications to metallic glasses, J. Mater. Sci. 16 (1981) 2401–2404. https://doi.org/10.1007/BF01113575.

[196] G. Ruitenberg, A.K. Petford-Long, R.C. Doole, Determination of the isothermal nucleation and growth parameters for the crystallization of thin Ge 2Sb 2Te 5 films, J. Appl. Phys. 92 (2002) 3116–3123. https://doi.org/10.1063/1.1503166.

[197] X.P. Wang, G. Corbel, S. Kodjikian, Q.F. Fang, P. Lacorre, Isothermal kinetic of phase transformation and mixed electrical conductivity in Bi3NbO7, J. Solid State Chem. 179 (2006) 3338–3346. https://doi.org/10.1016/j.jssc.2006.06.031.

[198] D. Dees, E. Gunen, D. Abraham, A. Jansen, J. Prakash, Alternating Current Impedance Electrochemical Modeling of Lithium-Ion Positive Electrodes, J. Electrochem. Soc. 152 (2005) A1409. https://doi.org/10.1149/1.1928169.

[199] D.W. Dees, A.N. Jansen, D.P. Abraham, Theoretical examination of reference electrodes for lithium-ion cells, J. Power Sources. 174 (2007) 1001–1006. https://doi.org/10.1016/j.jpowsour.2007.06.128.

[200] A.K. Dutta, Electrical conductivity of single crystals of graphite, Phys. Rev. 90 (1953) 187–192. https://doi.org/10.1103/PhysRev.90.187.

[201] M.S. Dresselhaus, G. Dresselhaus, Intercalation compounds of graphite, Adv. Phys. 30 (1981) 139–326. https://doi.org/10.1080/00018738100101367.

[202] N. Takami, A. Satoh, M. Hara, T. Ohsaki, Structural and Kinetic Characterization of Lithium Intercalation into Carbon Anodes for Secondary Lithium Batteries, J. Electrochem. Soc. 142 (1995) 371–379. https://doi.org/10.1149/1.2044017.

[203] M.D. Levi, D. Aurbach, The mechanism of lithium intercalation in graphite film electrodes in aprotic media. Part 1. High resolution slow scan rate cyclic voltammetric studies and modeling, J. Electroanal. Chem. 421 (1997) 79–88. https://doi.org/10.1016/S0022-0728(96)04832-2.

[204] M.D. Levi, E.A. Levi, D. Aurbach, The mechanism of lithium intercalation in graphite film electrodes in aprotic media. Part 2. Potentiostatic intermittent titration and in situ XRD studies of the solid-state ionic diffusion, J. Electroanal. Chem. 421 (1997) 89–97.

[205] K. Dokko, Y. Fujita, M. Mohamedi, M. Umeda, I. Uchida, J.R. Selman, Electrochemical impedance study of Li-ion insertion into mesocarbon microbead single particle electrode: Part II. Disordered carbon, Electrochim. Acta. 47 (2001) 933–938. https://doi.org/10.1016/S0013-4686(01)00809-X.

[206] H. Yang, H.J. Bang, J. Prakash, Evaluation of Electrochemical Interface Area and Lithium Diffusion Coefficient for a Composite Graphite Anode, J. Electrochem. Soc. 151 (2004) A1247. https://doi.org/10.1149/1.1763139.

[207] J. Shim, K.A. Striebel, Electrochemical characterization of thermally oxidized natural graphite anodes in lithium-ion batteries, J. Power Sources. 164 (2007) 862–867. https://doi.org/10.1016/j.jpowsour.2006.09.111.

[208] K. Persson, V.A. Sethuraman, L.J. Hardwick, Y. Hinuma, Y.S. Meng, A. Van Der Ven, V. Srinivasan, R. Kostecki, G. Ceder, Lithium diffusion in graphitic carbon, J. Phys. Chem. Lett. 1 (2010) 1176–1180. https://doi.org/10.1021/jz100188d.

[209] I. Umegaki, S. Kawauchi, H. Sawada, H. Nozaki, Y. Higuchi, K. Miwa, Y. Kondo, M. Månsson, M. Telling, F.C. Coomer, S.P. Cottrell, T. Sasaki, T. Kobayashi, J. Sugiyama, Li-ion diffusion in Li intercalated graphite C6Li and C12Li probed by μ+SR, Phys. Chem. Chem. Phys. 19 (2017) 19058–19066. https://doi.org/10.1039/c7cp02047c.

[210] M. Park, X. Zhang, M. Chung, G.B. Less, A.M. Sastry, A review of conduction phenomena in Li-ion batteries, J. Power Sources. 195 (2010) 7904–7929. https://doi.org/10.1016/j.jpowsour.2010.06.060.

[211] Z. Du, D.L. Wood, C. Daniel, S. Kalnaus, J. Li, Understanding limiting factors in thick electrode performance as applied to high energy density Li-ion batteries, J. Appl. Electrochem. (2017). https://doi.org/10.1007/s10800-017-1047-4.

[212] B. Vijayaraghavan, D.R. Ely, Y.-M. Chiang, R. García-García, R.E. García, An Analytical Method to Determine Tortuosity in Rechargeable Battery Electrodes, J. Electrochem. Soc. 159 (2012) A548–A552. https://doi.org/10.1149/2.jes113224.

[213] J. Newman, K.E. Thomas-Alyea, Electrochemical systems, John Wiley \& Sons, 2012.

[214] S. Krishnan, G. Brenet, E. Machado-Charry, D. Caliste, L. Genovese, T. Deutsch, P. Pochet, Revisiting the domain model for lithium intercalated graphite, Appl. Phys. Lett. 103 (2013). https://doi.org/10.1063/1.4850877.

[215] S.A. Safran, D.R. Hamann, Long-Range Elastic Interactions and Staging in Graphite Intercalation Compounds, Phys. Rev. Lett. 42 (1979) 1410–1413. https://doi.org/10.1103/PhysRevLett.42.1410.

[216] G. Kirczenow, Interference phenomena in the theory of Daumas-Hérold domain walls, Phys. Rev. Lett. 49 (1982) 1853–1856. https://doi.org/10.1103/PhysRevLett.49.1853.

[217] G. Forgács, G. Uiman, Possible mechanism for the staging transition in graphite-intercalation compounds, Phys. Rev. Lett. 52 (1984) 633–636. https://doi.org/10.1103/PhysRevLett.52.633.

[218] G. Kirczenow, Domain model of stage order and disorder in intercalation compounds, Phys. Rev. B. 31 (1985) 5376–5386. https://doi.org/10.1103/PhysRevB.31.5376.

[219] G. Kirczenow, Kinetics of stage ordering and stage transitions, Phys. Rev. Lett. 55 (1985) 2810–2813. https://doi.org/10.1103/PhysRevLett.55.2810.

[220] J.S.O. Evans, S.J. Price, H.V. Wong, D. O'Hare, Kinetic study of the intercalation of cobaltocene by layered metal dichalcogenides with time-resolved in situ X-ray powder diffraction, J. Am. Chem. Soc. 120 (1998) 10837–10846. https://doi.org/10.1021/ja9819099.

[221] A.M. Dimiev, G. Ceriotti, N. Behabtu, D. Zakhidov, M. Pasquali, R. Saito, J.M. Tour, Direct real-time monitoring of stage transitions in graphite intercalation compounds, ACS Nano. 7 (2013) 2773–2780. https://doi.org/10.1021/nn400207e.

[222] M. Li, J. Lu, Z. Chen, K. Amine, 30 Years of Lithium-Ion Batteries, Adv. Mater. 30 (2018) 1–24. https://doi.org/10.1002/adma.201800561.

[223] X. Zeng, M. Li, D. Abd El-Hady, W. Alshitari, A.S. Al-Bogami, J. Lu, K. Amine, Commercialization of Lithium Battery Technologies for Electric Vehicles, Adv. Energy Mater. 9 (2019) 1900161. https://doi.org/10.1002/aenm.201900161.

[224] L. Noel, G. Zarazua de Rubens, B.K. Sovacool, J. Kester, Fear and loathing of electric vehicles: The reactionary rhetoric of range anxiety, Energy Res. Soc. Sci. 48 (2019) 96–107. https://doi.org/https://doi.org/10.1016/j.erss.2018.10.001.

[225] X. Shi, J. Pan, H. Wang, H. Cai, Battery electric vehicles: What is the minimum range required?, Energy. 166 (2019) 352–358. https://doi.org/https://doi.org/10.1016/j.energy.2018.10.056.

[226] D. Howell, S. Boyd, B. Cunningham, S. Gillard, L. Slezak, S. Ahmed, I. Bloom, A. Burnham, K. Hardy, A.N. Jansen, Enabling fast charging: enabling fast charging: a technology gap assessment, 2017.

[227] S. Boyd, Batteries and electrification R&D overview, US Dep. Energy Veh. Technol. Off. Annu. Merit Rev. Meet. (2018).

[228] M. Keyser, A. Pesaran, Q. Li, S. Santhanagopalan, K. Smith, E. Wood, S. Ahmed, I. Bloom, E. Dufek, M. Shirk, A. Meintz, C. Kreuzer, C. Michelbacher, A. Burnham, T. Stephens, J. Francfort, B. Carlson, J. Zhang, R. Vijayagopal, K. Hardy, F. Dias, M. Mohanpurkar, D. Scoffield, A.N. Jansen, T. Tanim, A. Markel, Enabling fast charging – Battery thermal considerations, J. Power Sources. 367 (2017) 228–236. https://doi.org/https://doi.org/10.1016/j.jpowsour.2017.07.009.

[229] A. Meintz, J. Zhang, R. Vijayagopal, C. Kreutzer, S. Ahmed, I. Bloom, A. Burnham, R.B. Carlson, F. Dias, E.J. Dufek, J. Francfort, K. Hardy, A.N. Jansen, M. Keyser, A. Markel, C. Michelbacher, M. Mohanpurkar, A. Pesaran, D. Scoffield, M. Shirk, T. Stephens, T. Tanim, Enabling fast charging – Vehicle considerations, J. Power Sources. 367 (2017) 216–227. https://doi.org/https://doi.org/10.1016/j.jpowsour.2017.07.093.

[230] Y. Liu, Y. Zhu, Y. Cui, Challenges and opportunities towards fast-charging battery materials, Nat. Energy. 4 (2019) 540–550. https://doi.org/10.1038/s41560-019-0405-3.

[231] Q. Liu, C. Du, B. Shen, P. Zuo, X. Cheng, Y. Ma, G. Yin, Y. Gao, Understanding undesirable anode lithium plating issues in lithium-ion batteries, RSC Adv. 6 (2016) 88683–88700. https://doi.org/10.1039/c6ra19482f.

[232] J.R. Dahn, T. Zheng, Y. Liu, J.S. Xue, Mechanisms for Lithium Insertion in Carbonaceous Materials, Science (80-.). 270 (1995) 590. https://doi.org/10.1126/science.270.5236.590.

[233] C. Mao, R.E. Ruther, J. Li, Z. Du, I. Belharouak, Identifying the limiting electrode in lithium ion batteries for extreme fast charging, Electrochem. Commun. 97 (2018) 37–41. https://doi.org/https://doi.org/10.1016/j.elecom.2018.10.007.

[234] N. Legrand, B. Knosp, P. Desprez, F. Lapicque, S. Raël, Physical characterization of the charging process of a Li-ion battery and prediction of Li plating by electrochemical modelling, J. Power Sources. (2014). https://doi.org/10.1016/j.jpowsour.2013.06.130.

[235] S. Malifarge, B. Delobel, C. Delacourt, Experimental and Modeling Analysis of Graphite Electrodes with Various Thicknesses and Porosities for High-Energy-Density Li-Ion Batteries, J. Electrochem. Soc. 165 (2018) A1275–A1287. https://doi.org/10.1149/2.0301807jes.

[236] A.M. Colclasure, A.R. Dunlop, S.E. Trask, B.J. Polzin, A.N. Jansen, K. Smith, Requirements for Enabling Extreme Fast Charging of High Energy Density Li-Ion Cells while Avoiding Lithium Plating, J. Electrochem. Soc. 166 (2019) A1412–A1424. https://doi.org/10.1149/2.0451908jes.

[237] X.G. Yang, C.Y. Wang, Understanding the trilemma of fast charging, energy density and cycle life of lithium-ion batteries, J. Power Sources. 402 (2018) 489–498. https://doi.org/10.1016/j.jpowsour.2018.09.069.

[238] X.-G. Yang, G. Zhang, S. Ge, C.-Y. Wang, Fast charging of lithium-ion batteries at all temperatures, Proc. Natl. Acad. Sci. 115 (2018) 7266–7271. https://doi.org/10.1073/pnas.1807115115.

[239] K. Xu, Electrolytes and Interphases in Li-Ion Batteries and Beyond, Chem. Rev. 114 (2014) 11503–11618. https://doi.org/10.1021/cr500003w.

[240] D.S. Hall, A. Eldesoky, E.R. Logan, E.M. Tonita, X. Ma, J.R. Dahn, Exploring Classes of Co-Solvents for Fast-Charging Lithium-Ion Cells, J. Electrochem. Soc. 165 (2018) A2365–A2373. https://doi.org/10.1149/2.1351810jes.

[241] M.S. Ding, K. Xu, S.S. Zhang, K. Amine, G.L. Henriksen, T.R. Jow, Change of Conductivity with Salt Content, Solvent Composition, and Temperature for Electrolytes of LiPF 6 in Ethylene Carbonate-Ethyl Methyl Carbonate, J. Electrochem. Soc. (2001). https://doi.org/10.1149/1.1403730.

[242] M.S. Ding, T.R. Jow, Conductivity and viscosity of PC-DEC and PC-EC solutions of LiPF6, J. Electrochem. Soc. (2003). https://doi.org/10.1149/1.1566019.

[243] K. Xu, Nonaqueous liquid electrolytes for lithium-based rechargeable batteries, Chem. Rev. (2004). https://doi.org/10.1021/cr030203g.

[244] S. Huang, X. Wu, G.M. Cavalheiro, X. Du, B. Liu, Z. Du, G. Zhang, In Situ Measurement of Lithium-Ion Cell Internal Temperatures during Extreme Fast Charging, J. Electrochem. Soc. 166 (2019) 3254–3259. https://doi.org/10.1149/2.0441914jes.

[245] X.-G. Yang, Y. Leng, G. Zhang, S. Ge, C.-Y. Wang, Modeling of lithium plating induced aging of lithium-ion batteries: Transition from linear to nonlinear aging, J. Power Sources. 360 (2017) 28–40. https://doi.org/https://doi.org/10.1016/j.jpowsour.2017.05.110.

[246] X.-G. Yang, S. Ge, T. Liu, Y. Leng, C.-Y. Wang, A look into the voltage plateau signal for detection and quantification of lithium plating in lithium-ion cells, J. Power Sources. 395 (2018) 251–261. https://doi.org/https://doi.org/10.1016/j.jpowsour.2018.05.073.

[247] J. Xu, E. Hu, D. Nordlund, A. Mehta, S.N. Ehrlich, X.-Q. Yang, W. Tong, Understanding the Degradation Mechanism of Lithium Nickel Oxide Cathodes for Li-Ion Batteries, ACS Appl. Mater. Interfaces. 8 (2016) 31677–31683. https://doi.org/10.1021/acsami.6b11111.

[248] W.-S. Yoon, M. Balasubramanian, K.Y. Chung, X.-Q. Yang, J. McBreen, C.P. Grey, D.A. Fischer, Investigation of the Charge Compensation Mechanism on the Electrochemically Li-Ion Deintercalated Li1-xCo1/3Ni1/3Mn1/3O2 Electrode System by Combination of Soft and Hard X-ray Absorption Spectroscopy, J. Am. Chem. Soc. 127 (2005) 17479–17487. https://doi.org/10.1021/ja0530568.

[249] B. Ravel, M. Newville, ATHENA, ARTEMIS, HEPHAESTUS: Data analysis for X-ray absorption spectroscopy using IFEFFIT, in: J. Synchrotron Radiat., 2005. https://doi.org/10.1107/S0909049505012719.

[250] I. Belharouak, W. Lu, D. Vissers, K. Amine, Safety characteristics of Li(Ni0.8Co0.15Al 0.05)O2 and Li(Ni1/3Co1/3Mn 1/3)O2, Electrochem. Commun. (2006). https://doi.org/10.1016/j.elecom.2005.12.007.

[251] C.-H. Shen, S.-Y. Shen, F. Fu, C.-G. Shi, H.-Y. Zhang, M.J. Pierre, H. Su, Q. Wang, B.-B. Xu, L. Huang, J.-T. Li, S.-G. Sun, New insight into structural transformation in Li-rich layered oxide during the initial charging, J. Mater. Chem. A. 3 (2015) 12220–12229. https://doi.org/10.1039/C5TA01849H.

[252] T. Sasaki, T. Abe, Y. Iriyama, M. Inaba, Z. Ogumi, Formation mechanism of alkyl dicarbonates in Li-ion cells, J. Power Sources. 150 (2005) 208–215. https://doi.org/https://doi.org/10.1016/j.jpowsour.2005.02.021.

[253] G. Zhuang, Y. Chen, P.N. Ross, The Reaction of Lithium with Dimethyl Carbonate and Diethyl Carbonate in Ultrahigh Vacuum Studied by X-ray Photoemission Spectroscopy, Langmuir. 15 (1999) 1470–1479. https://doi.org/10.1021/la980454y.

[254] K. Edström, T. Gustafsson, J.O. Thomas, The cathode–electrolyte interface in the Li-ion battery, Electrochim. Acta. 50 (2004) 397–403. https://doi.org/https://doi.org/10.1016/j.electacta.2004.03.049.

[255] R. Dedryvère, H. Martinez, S. Leroy, D. Lemordant, F. Bonhomme, P. Biensan, D. Gonbeau, Surface film formation on electrodes in a LiCoO2/graphite cell: A step by step XPS study, J. Power Sources. 174 (2007) 462–468. https://doi.org/https://doi.org/10.1016/j.jpowsour.2007.06.033.

[256] S.J. An, J. Li, C. Daniel, D. Mohanty, S. Nagpure, D.L. Wood, The state of understanding of the lithium-ion-battery graphite solid electrolyte interphase (SEI) and its relationship to formation cycling, Carbon N. Y. 105 (2016) 52–76. https://doi.org/10.1016/j.carbon.2016.04.008.

[257] P. Niehoff, M. Winter, Composition and Growth Behavior of the Surface and Electrolyte Decomposition Layer of/on a Commercial Lithium Ion Battery LixNi1/3Mn1/3Co1/3O2 Cathode Determined by Sputter Depth Profile X-ray Photoelectron Spectroscopy, Langmuir. 29 (2013) 15813–15821. https://doi.org/10.1021/la403276p.

[258] A.M. Andersson, D.P. Abraham, R. Haasch, S. MacLaren, J. Liu, K. Amine, Surface characterization of electrodes from high power lithium-ion batteries, J. Electrochem. Soc. 149 (2002) 1358–1369. https://doi.org/10.1149/1.1505636.

[259] A.M. Andersson, A. Henningson, H. Siegbahn, U. Jansson, K. Edström, Electrochemically lithiated graphite characterised by photoelectron spectroscopy, in: J. Power Sources, 2003. https://doi.org/10.1016/S0378-7753(03)00277-5.

[260] D. Pantea, H. Darmstadt, S. Kaliaguine, C. Roy, Electrical conductivity of conductive carbon blacks: influence of surface chemistry and topology, Appl. Surf. Sci. 217 (2003) 181–193. https://doi.org/https://doi.org/10.1016/S0169-4332(03)00550-6.

[261] M. Nie, D. Chalasani, D.P. Abraham, Y. Chen, A. Bose, B.L. Lucht, Lithium Ion Battery Graphite Solid Electrolyte Interphase Revealed by Microscopy and Spectroscopy, J. Phys. Chem. C. 117 (2013) 1257–1267. https://doi.org/10.1021/jp3118055.

[262] L. Madec, R. Petibon, K. Tasaki, J. Xia, J.P. Sun, I.G. Hill, J.R. Dahn, Mechanism of action of ethylene sulfite and vinylene carbonate electrolyte additives in LiNi1/3Mn1/3Co1/3O2/graphite pouch cells: electrochemical, GC-MS and XPS analysis, Phys. Chem. Chem. Phys. 17 (2015) 27062–27076. https://doi.org/10.1039/C5CP04221F.

[263] S.E. Sloop, J.B. Kerr, K. Kinoshita, The role of Li-ion battery electrolyte reactivity in performance decline and self-discharge, J. Power Sources. 119–121 (2003) 330–337. https://doi.org/https://doi.org/10.1016/S0378-7753(03)00149-6.

[264] S. Malmgren, K. Ciosek, M. Hahlin, T. Gustafsson, M. Gorgoi, H. Rensmo, K. Edström, Comparing anode and cathode electrode/electrolyte interface composition and morphology using soft and hard X-ray photoelectron spectroscopy, Electrochim. Acta. 97 (2013) 23–32. https://doi.org/https://doi.org/10.1016/j.electacta.2013.03.010.

[265] M. Herstedt, M. Stjerndahl, A. Nytén, T. Gustafsson, H. Rensmo, H. Siegbahn, N. Ravet, M. Armand, J.O. Thomas, K. Edström, Surface Chemistry of Carbon-Treated LiFePO[sub 4] Particles for Li-Ion Battery Cathodes Studied by PES, Electrochem. Solid-State Lett. 6 (2003) A202. https://doi.org/10.1149/1.1594413.

[266] Y. Qian, P. Niehoff, M. Börner, M. Grützke, X. Mönnighoff, P. Behrends, S. Nowak, M. Winter, F.M. Schappacher, Influence of electrolyte additives on the cathode electrolyte interphase (CEI) formation on LiNi1/3Mn1/3Co1/3O2 in half cells with Li metal counter electrode, J. Power Sources. 329 (2016) 31–40. https://doi.org/https://doi.org/10.1016/j.jpowsour.2016.08.023.

APPENDIX A. SUPPORTING INFORMATION

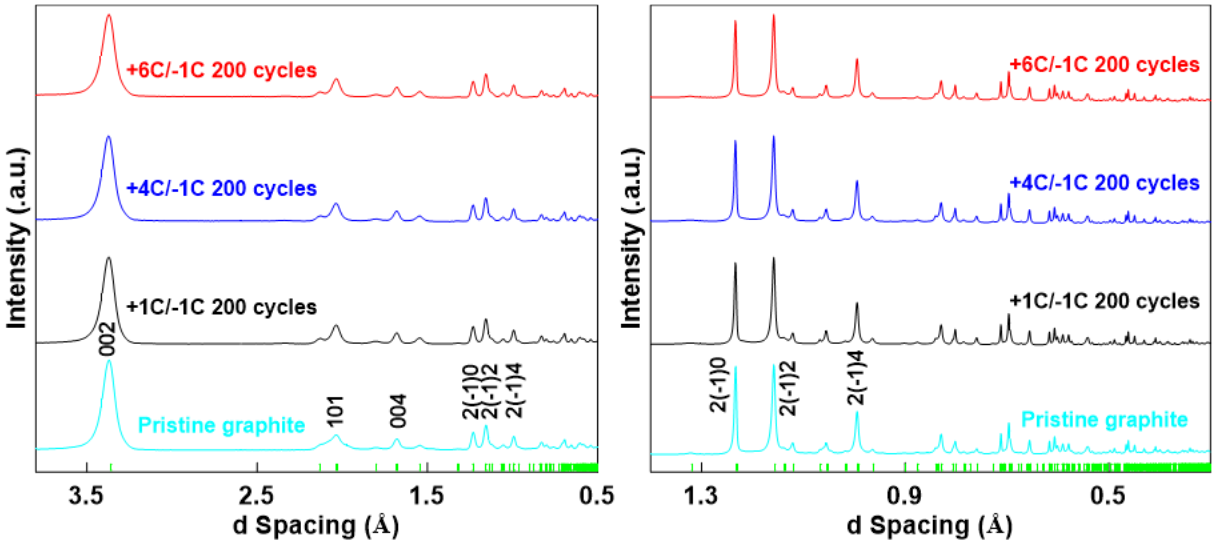

Figure S1. Neutron power diffraction of pristine graphite and graphite after repeated cycles. (a) bank #1 and (b) bank #4.

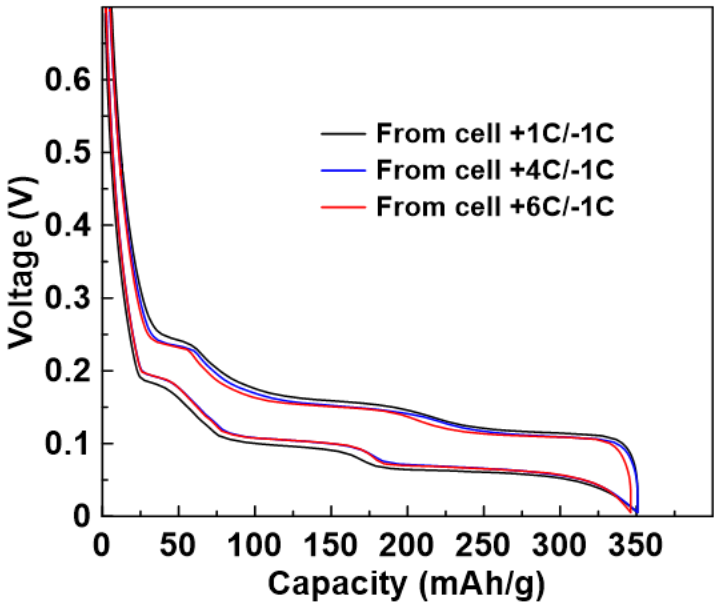

Figure S2**.** Voltage curves at C/10 rate of Li coin cells assembled with graphite anode after 200 cycles under +1C/-1C, +4C/-1C and +6C/-1C charge/discharge rates.

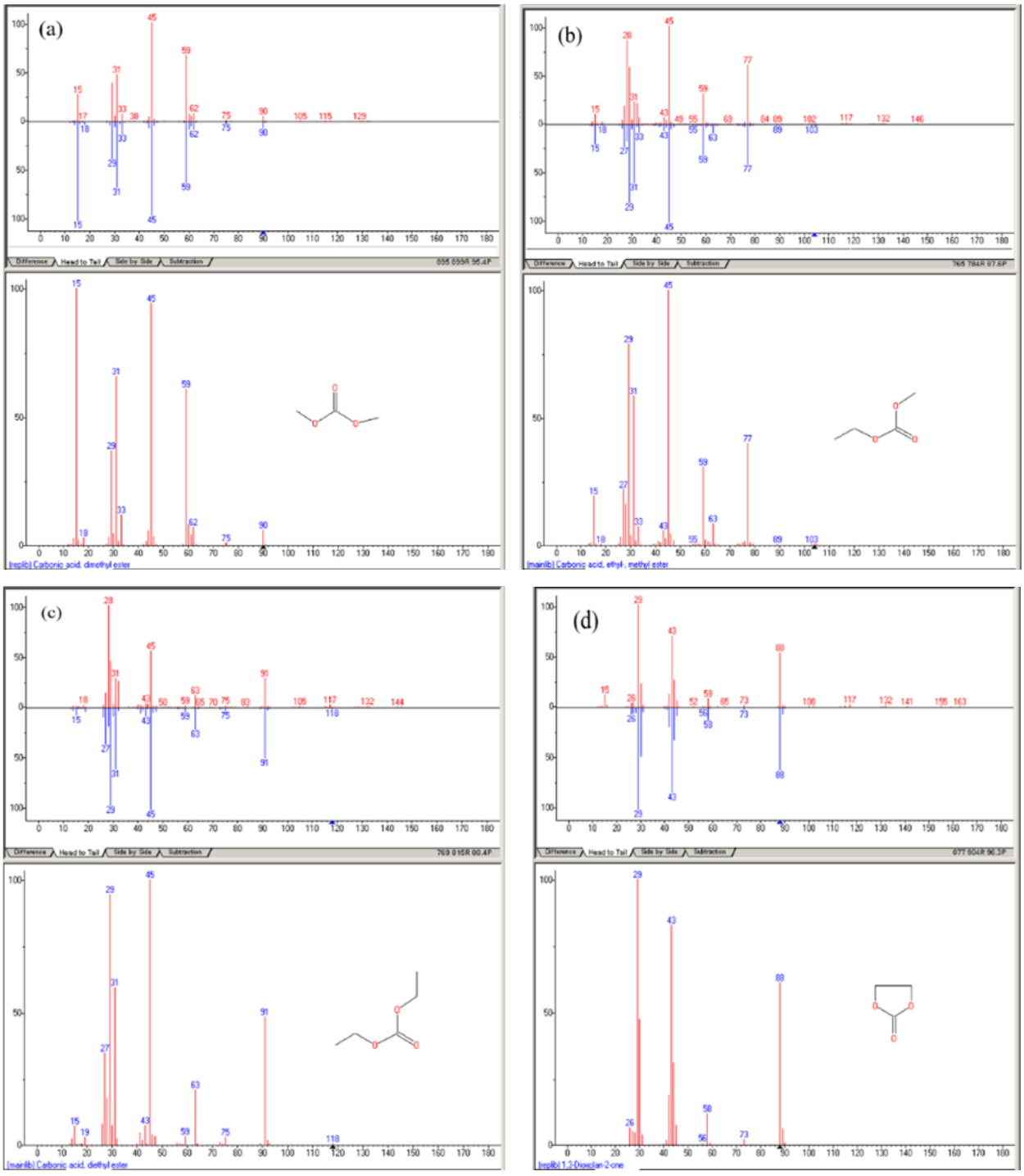

Figure S3: The MS spectroscopy for extracted electrolyte: (a) DMC; (b) EMC; (c) DEC; and (d) EC

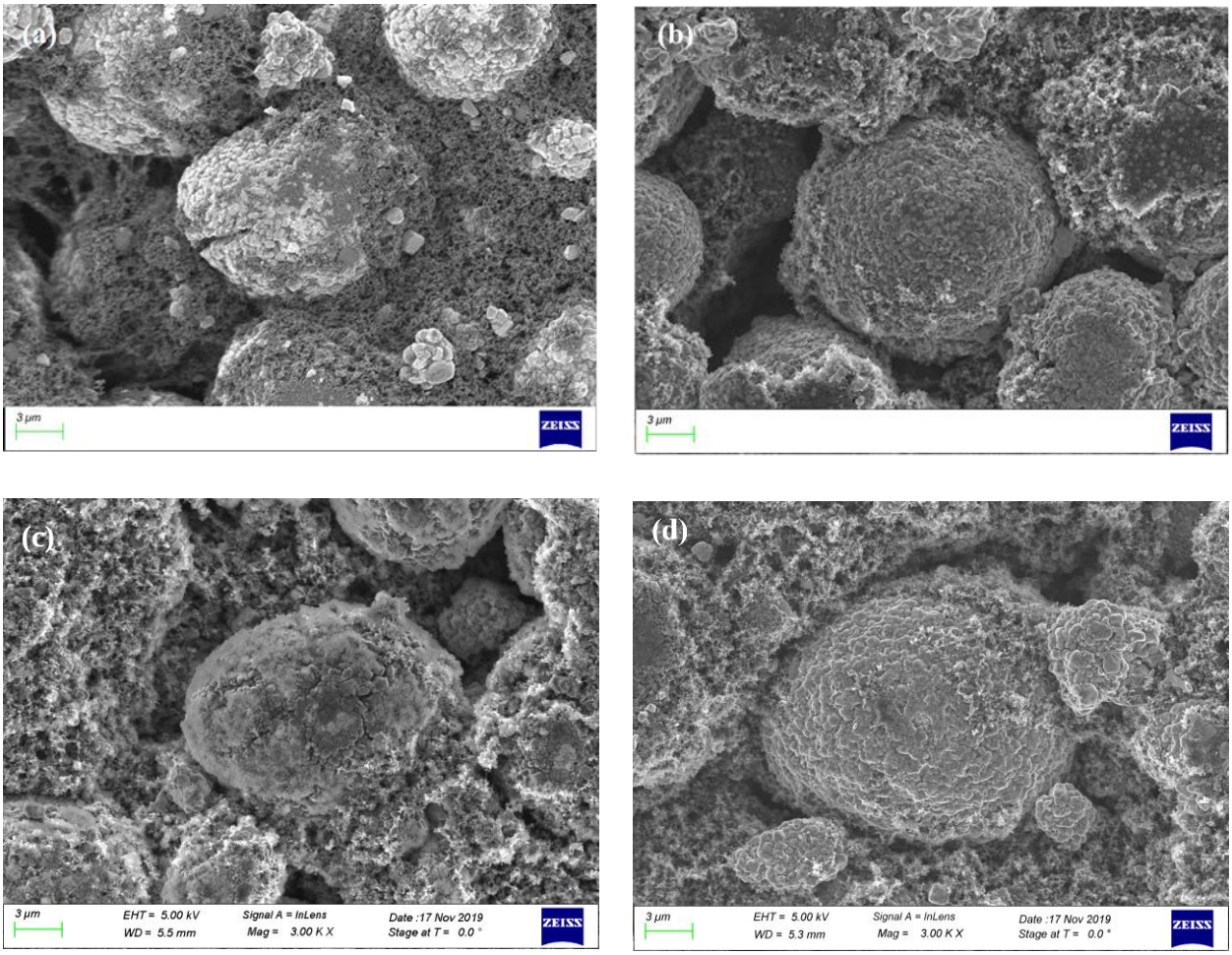

Figure S4: The SEM images of NMC622 under various charging rates: (a) Pristine NMC622; (b) NMC622 cycled under +1C/-1C; (c) NMC622 cycled under +4C/-1C; (d) NMC622 cycled under +6C/-1C.

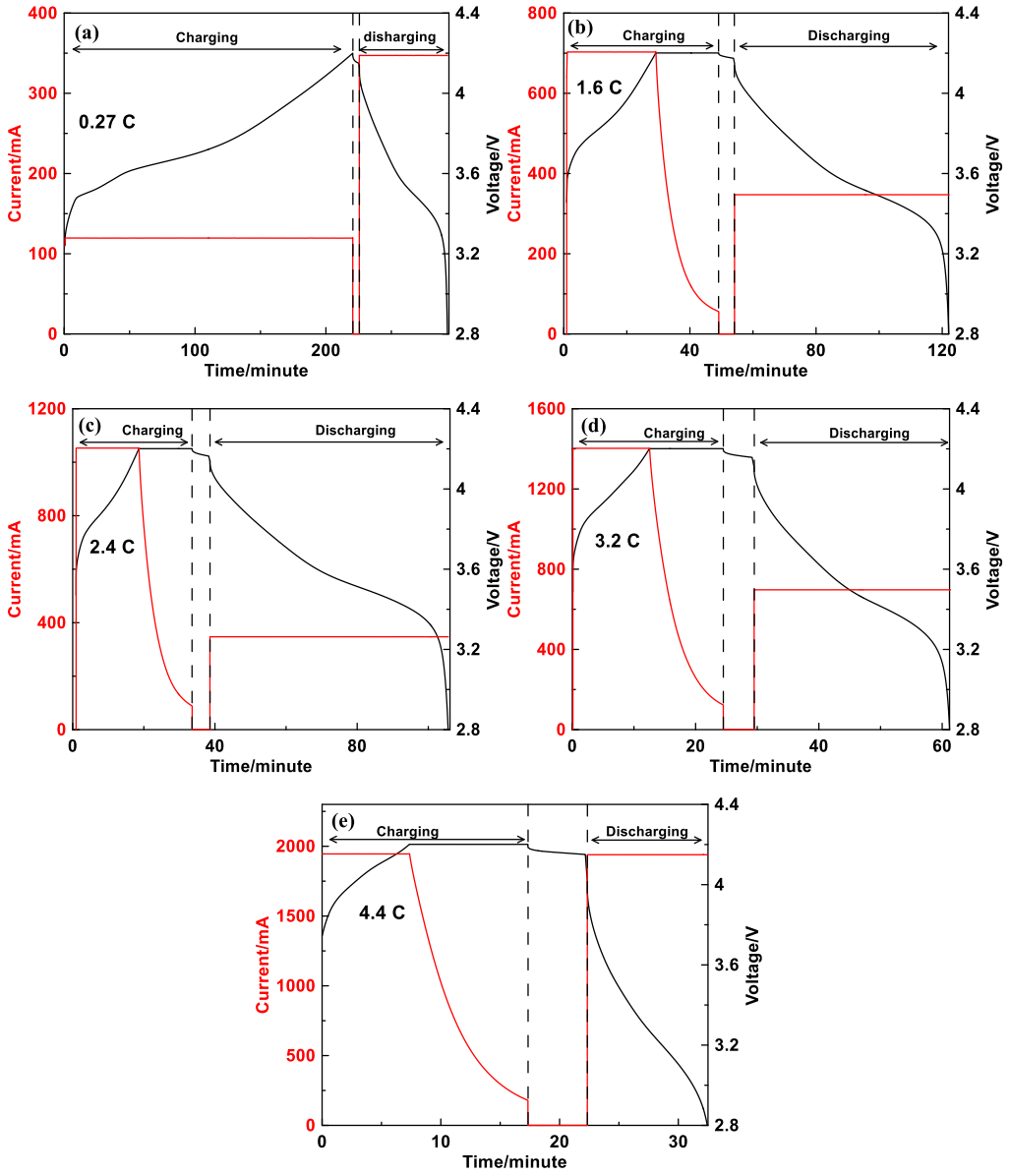

Figure S5. The detailed electrochemical performance of the cylindrical cell under 5 charging rates (a) Rate 1, 0.27 C; (b) Rate 2, 1.6 C; (c) Rate 3, 2.4 C; (d) Rate 4, 3.2 C; (e) Rate 5, 4.4 C.

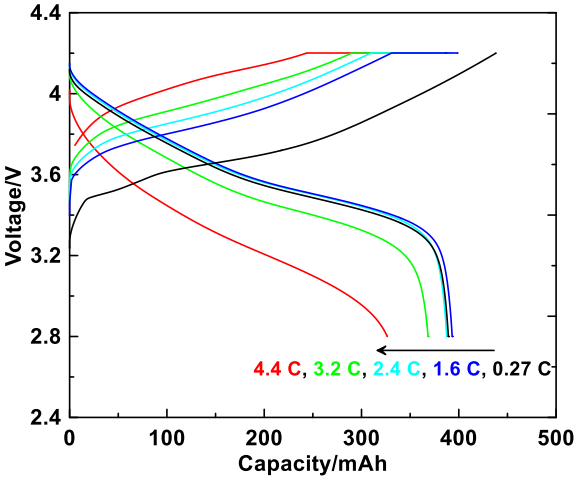

Figure S6. The voltage-capacity curve under all the 5 charging rates

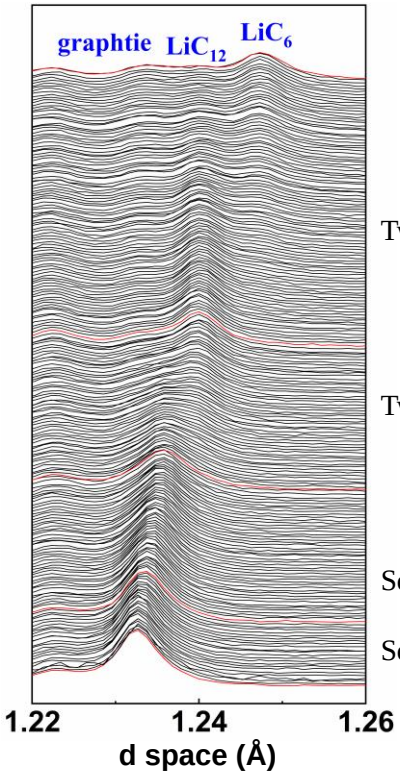

Two phases: Stage II to Stage I

Two phases: dilute Stage II and Stage II

Solid solution: Stage III

Solid solution process

Figure S7. The phase transition of lithiated graphite during the 0.27 C charging

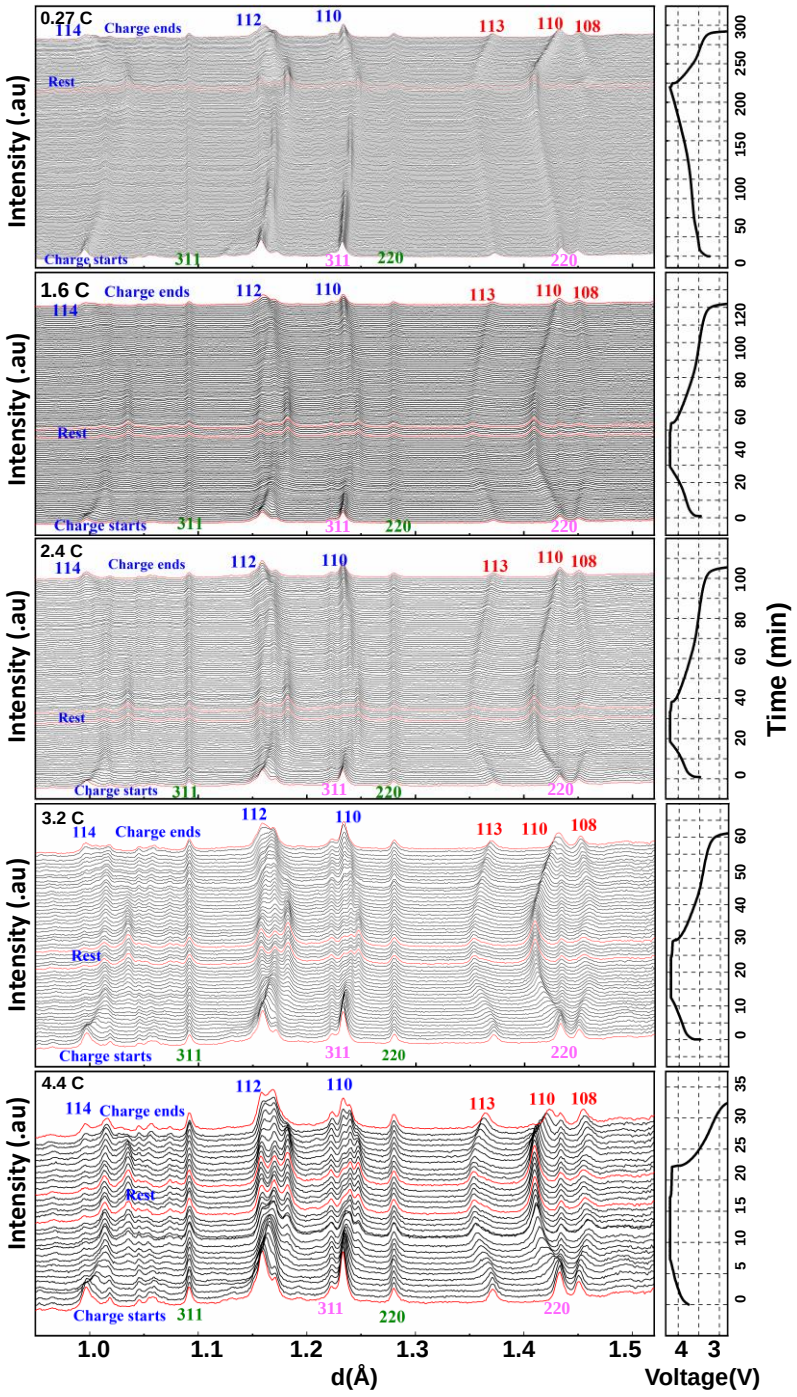

Figure S8. The diffraction patterns alongside with the voltage profile for all 5 rates, with major Bragg peaks from lithiated graphite, NMC622, Cu, Al current collector labelled in blue, red, olive and magenta.

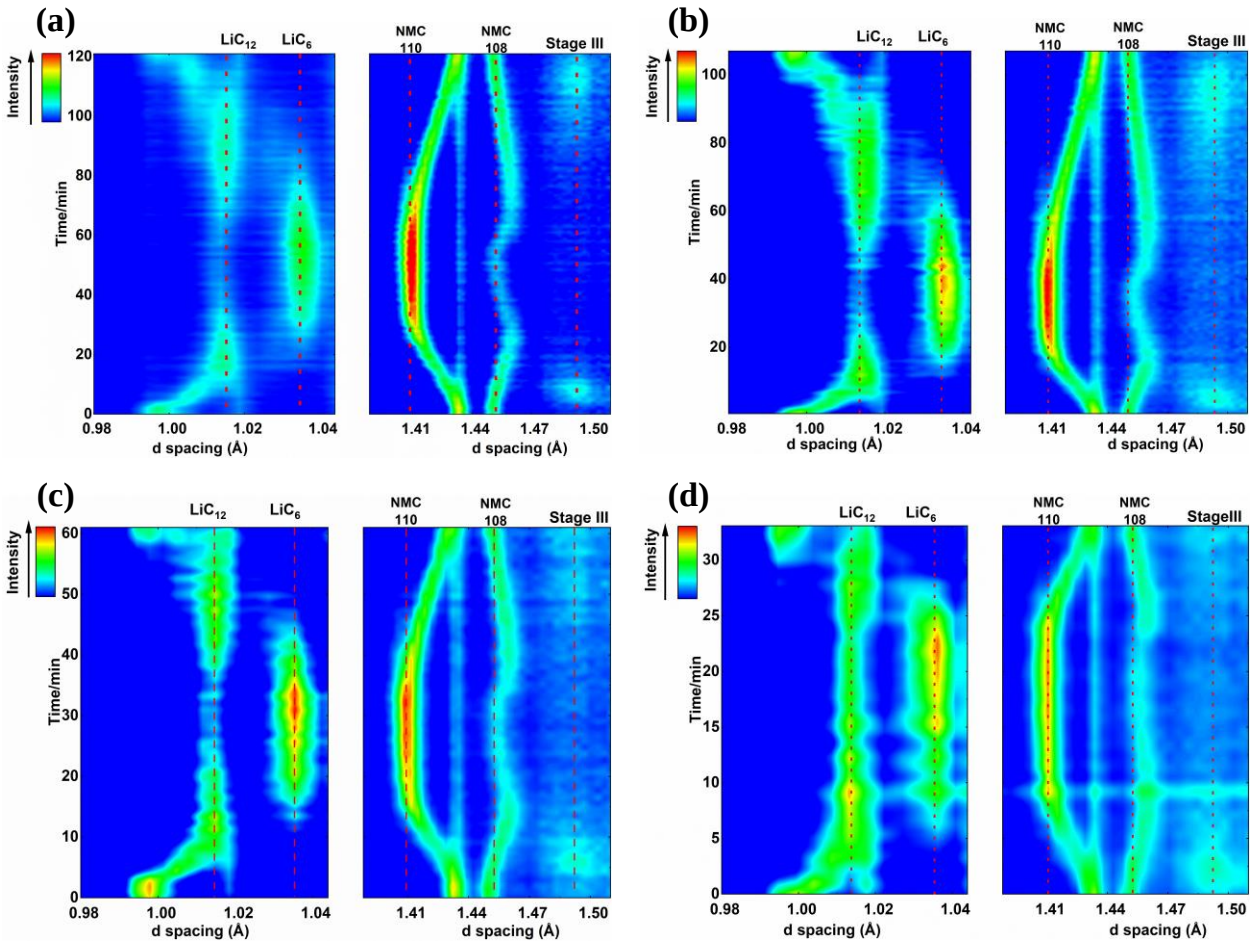

Figure S9. The phase evolution of Stage III, Stage II (LiC_{12}), Stage I (LiC_6) under higher charging rates: (a) 1.6 C; (b) 2.4 C; (c) 3.2 C; (d) 4.4 C.

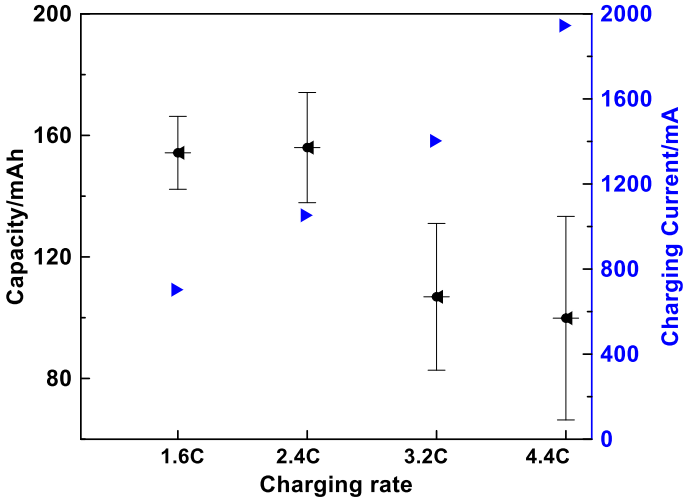

Figure S10. The capacity for the first show-up of stage I (LiC_6) within the cell under charging rates from 1.6 C to 4.4 C

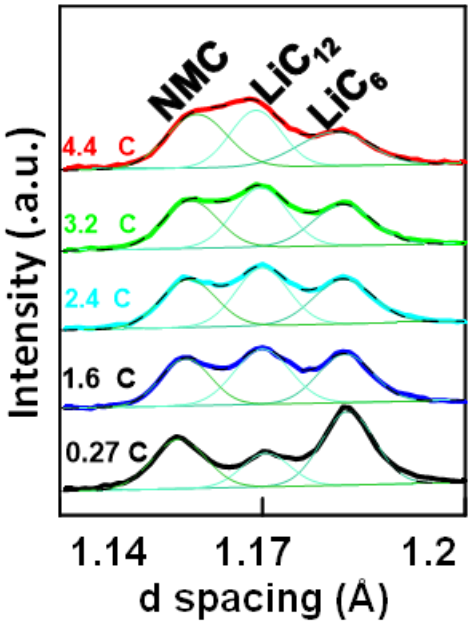

Figure S11. The qualitative comparison of LiC_6 and LiC_{12} contents under the 5 charging rates, the black dot line represents the cumulative line of all these 3 fitted peaks, the spring green line is fitted NMC peak, the turquoise line is fitted LiC_{12} peak and the sea green is fitted LiC_6 peak.

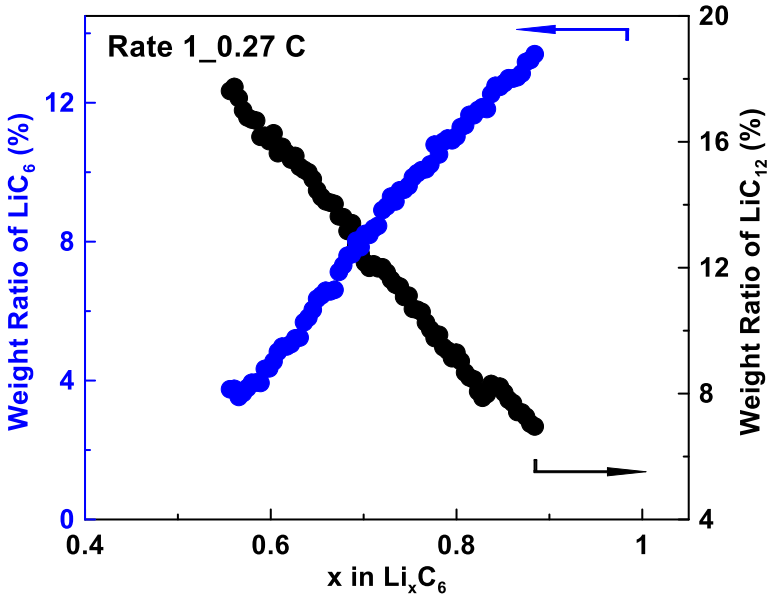

Figure S12. The time evolution of LiC_{12} and LiC_6 for the whole charging process under 0.27 C.

Table S1. EXAFS fitting parameters for the representative data shows in Figure 5b.

Electrolytes	R-factor	Ni-O (Å)	Ni-M (Å)	σ^2 (Å^2)
Pristine	0.0022729	2.00303	2.88605	0.00502
EMC	0.0064467	1.91063	2.86348	0.00445
DMC	0.0068221	1.93981	2.86732	0.00454
EA	0.0043508	1.90001	2.86121	0.00529
EF	0.047146	1.91264	2.88406	0.00657
MA	0.013005	1.90679	2.85936	0.00431

Table S2. Peak assignments for the XPS spectra of SEI layer

Region	Component	Binding energy (eV)
C 1s	Li-C	~ 282.4
	C-C of Carbon	~ 284.4
	C-O of ($ROCO_2Li$) or ether	~ 286.4
	C=O of $ROCO_2Li$	~ 288.6
	CO_3 of Li_2CO_3	~ 289.8
O 1s	CO3- in (ROCO2Li)	~ 531.5
	C-O of $ROCO_2Li$	~ 533.5
F 1s	LiF	~ 685.0
	PVDF/$LiPF_x$	~687.0
P 2p	$2p_{3/2}$ P=O	~133.7
	$2p_{1/2}$ P=O	~134.5
	$2p_{3/2}$ P=F	~136.7
	$2p_{1/2}$ P=F	~137.5

Table S3. The peak assignment for the XPS spectra of CEI layer.

Region	Components	Binding energy (eV)
C 1s	Carbon black	~ 284.4
	C-O of PEO	~ 286.4
	C=O of Li_2CO_3	~ 288.0
	C-F of PVDF	~ 290.4
O 1s		~ 527.8
	M-O	~ 530.0
	Li_2CO_3	~ 531.5
	C-O of R_2CO_3	~ 533.5
F 1s	LiF	~ 685.0
	C-F/P-F	~ 687.7
P 2p	$2p_{3/2}$ P=O	~ 133.7
	$2p_{1/2}$ P=O	~ 134.5
	$2p_{3/2}$ P=F	~ 136.7
	$2p_{1/2}$ P=F	~ 137.5

VITA

Xianyang Wu

Ph. D candidate, Purdue University

Education

08.2017- 12.2021	Ph.D. in Mechanical Engineering, Purdue University,
	Major Advisor: Prof. Kejie Zhao
08.2016-07.2017	Nuclear Engineering, Purdue University.
09.2012-07.2015	Master of Science, Nuclear Science and Technology, Tsinghua University.
09.2006-07.2010	Bachelor of Engineering, Xi'an Jiaotong University.

Publications

1. **Xianyang Wu**, Bohang Song, Po-Hsiu Chien, Michelle S. Everett, Kejie Zhao, Jue Liu, Zhijia Du "Structural evolution and transition dynamics in Lithium ion battery under fast charging: an operando neutron diffraction investigation" (**Advanced Science**)
2. **Xianyang Wu**, Yaocai Bai, Zhenglong Li, Jue Liu, Kejie Zhao, Zhijia Du, "Effects of charging rates on $LiNi_{0.6}Mn_{0.2}CoO_2$ (NMC622)/graphite Li-ion cells." *Journal of Energy Chemistry* 56 (2020): 121-126.
3. **Xianyang Wu**, Tianyi Liu, Yaocai Bai, Xu Feng, Muhammad Mominur Rahman, Chengjun Sun, Feng Lin, Kejie Zhao, Zhijia Du "Effects of solvent formulations in electrolytes on fast charging of Li-ion cells." *Electrochimica Acta* (2020): 136453.
4. Liu, Tianyi, Zhijia Du, **Xianyang** Wu, Muhammad Mominur Rahman, Dennis Nordlund, Kejie Zhao, Michael D Schulz, Feng Lin, David Wood, Ilias Belharouak, "Bulk and surface structural changes in high nickel cathodes subjected to fast charging conditions." Chemical Communications (2020).
5. Shan Huang, **Xianyang Wu**, Gabriel M Cavalheiro, Xiaoniu Du, Bangzhi Liu, Zhijia Du, Guangsheng Zhang, "In Situ measurement of lithium-ion cell internal temperatures during extreme fast charging." Journal of the Electrochemical Society 166.14 (2019): A3254.

Research Experience

Utilization of additives on Li-ion batteries (LIBs) under extreme fast charging

05.2020-Now

- Rate and long-term cycling performance of LIBs using pouch cells filled with various additives
- Post-mortem characterization of cycled electrodes: quantitative analysis of composition evolution in the cathode-electrolyte interphase (CEI) and solid electrolyte interphase

(SEI) via X-ray photoelectron spectroscopy (XPS), neutron powder diffraction (NPD) on cycled electrodes, the resistance growth via hybrid pulse power characterization (HPCC), the morphology evolution of cycled electrodes via SEM.

Structural evolution of graphite anode under increasing charging rates

02.2020-04.2020

- Preparation of cylindrical cell and operando neutron powder diffraction (NPD) experiment at the Spallation Neutron Source (SNS), ORNL;
- The analysis of structural evolution of $LiNi_{0.6}Mn_{0.2}CoO_2$ (NMC622) cathodes and lithiated graphite anodes via Rietveld refinement.

Study on effects of esters as co-solvent on extreme fast charging of LIBs

09.2019-01.2020

- Preparation and electrochemical testing of pouch cells filled with various esters as co-solvent, coin cells using cycled NMC622 cathodes in verifying the loss of active Li from NMC622 due to Li plating;
- Post-mortem characterization of cycled pouch cells: XPS analysis of composition evolution in the CEI and SEI, NPD on cycled electrodes and following Rietveld refinement to extract the structural evolution of electrodes after long term cycling, the evolution of chemical state for transition metal elements in NMC622 electrodes via X-ray absorption spectroscopy (XAS).

Effect of charging rates on LIBs

02.2019-08.2019

- Degradation of pouch cells under various charging rates;
- Characterization of composition evolution in the cycled electrolytes via inductively coupled plasma - optical emission spectrometry (ICP-OES), gas chromatography–mass spectrometry (GC-MS), the structural evolution of electrodes via NPD;

Manufacturing and electrochemical testing of pouch cells

09.2018-01.2019

- Manufacture process of single/multi-layer pouch cells: slurry preparation and coating, pouching of electrodes, tap welding, cell assembly, electrolyte filling and vacuum sealing;
- Electrochemical measurement of pouch cells: electrochemical impedance spectroscopy (EIS) / HPPC measurements, cyclic voltammetry (CV) tests and long term cycling of pouch cells.

Investigation of Solid State Electrolytes

08.2017-08.2018

- Mechanical test of sintered LLZTO with nano-indentation and structural characterization via XRD and electron backscatter diffraction (EBSD).

Technical Skills

Programming Languages/skills: FORTRAN, MATLAB, C, PYTHON, ABAQUS, CATIA;

Experimental skills:

- Operando characterization of LIBs: operando neutron imaging (2D imaging and 3D tomography) and operando neutron powder diffraction;
- Pouch cell preparation: slurry preparation and coating, pouching of electrodes, tap welding, single/multi-layer cell assembly, electrolyte filling and vacuum sealing;
- Electrochemical testing: EIS, HPPC, CV methods;
- Structural characterization: XAS, XPS, EBSD, XRD/NPD and Rietveld refinement,
- Synthesis and sintering of solid state electrolytes (LLZTO and glassy Li_2S-P_2S_5)
- Others: the Brunauer-Emmett and Teller (BET) technique, ion-polishing, nano-indentation.

Honors & Awards

SiYuan Scholarship for Outstanding Students, Sep.2008

Outstanding Student in the Training Course of Social Works, June, 2013.